DISS. ETH NO. 21731

Four-Dimensional Monte Carlo Simulations of Lung Cancer Treatments with Scanned Proton Beams

A thesis submitted to attain the degree of

DOCTOR OF SCIENCES of ETH ZURICH
(Dr. sc. ETH Zurich)

presented by

CLEMENS GRASSBERGER

MSc ETH Physics

born on 04.07.1984
citizen of AUSTRIA

accepted on the recommendation of
Prof. Dr. Tony Lomax
Prof. Dr. Harald Paganetti
Prof. Dr. Klaus Kirch
Prof. Dr. Martijn Engelsman

2014

Abstract:

The main objective of this thesis is the time-dependent Monte Carlo simulation of lung cancer patient treatments with scanned beams of protons.

Lung cancer remains the leading cause of cancer death worldwide, and radiotherapy plays a crucial role in its management. Due to their superior physical properties, protons are becoming more popular in the field of radiotherapy, which is conventionally delivered using photons. Proton therapy is currently mainly delivered using passively scattered beams, though most centers in planning will employ scanned beams for treatment. Irradiation with scanned beams of protons promises further improvements, however challenges remain in the areas of dose calculation accuracy and concerning the interference between beam and respiratory motion, termed the *interplay effect*.

To enhance the delivery accuracy of scanned proton beams and exploit their properties, improved dose prediction is crucial. To quantify the increased accuracy in dose calculation that can be gained by using Monte Carlo methods, they are validated experimentally in the first part of this work using a passively scattered proton beam in a static lung phantom. Comparing the results to analytical dose calculation methods currently employed clinically, we can confirm the superiority of Monte Carlo methods, especially in the modeling of *multiple coulomb scattering* in the complex lung geometries under investigation.

Subsequently the Monte Carlo code is adapted to two specific active scanning beam lines at Paul Scherrer Institut (PSI) and Massachusetts General Hospital (MGH), confirming that the limited amount of scattering in the gantry enables us to perform phase space based simulations starting close to the patient surface. It is also demonstrated how to model the initial energy spectrum accurately to reproduce dose measurements in water. Furthermore we show how to translate the output of the treatment planning system to a phase space of protons and perform static simulations in patients for liver, head&neck and lung.

Thereafter motion of the patient is added to the Monte Carlo simulations by using four-dimensional computer tomography data and deformable image registration. The interplay effect is then quantified in 10 patients with varying tumor motion treated with scanned proton beams of two different sizes, representing the spot sizes at PSI (SmallSpots) and MGH (BigSpots). The results show the profound impact of the beam size and estimate the averaging that can be expected from fractionation, i.e. the spreading of the irradiation over many sessions.

Finally, various methods to mitigate the interplay effect are investigated, such as *rescanning* the target repeatedly and *gating*, the restriction of the irradiation to specific motion states. Techniques to mitigate the effect even for single treatment sessions are important, as there is a trend to restrict the treatment of lung cancer to just a few sessions, termed *Hypofractionation*. The simulations show the efficiency of rescanning and gating in mitigating the interplay effect up to extensive target motion, as well as circumstances in which their performance is inadequate.

The work presented explores the motion effects from the interference of scanned proton beams and moving targets in patients using Monte Carlo simulations. The encouraging results demonstrate how to prevent this interplay effect and bring the treatment of lung cancer with scanned proton beams closer to application.

Zusammenfassung:

Das Ziel der vorliegenden Dissertation ist die vier-dimensionale Monte Carlo Simulation der Behandlung von Lungenkrebspatienten mit magnetisch deflektierten Protonenstrahlen (*pencil beam scanning*).

Lungenkrebs ist nach wie vor einer der weltweit am häufigsten auftretenen Krebsarten und Strahlentherapie spielt eine zentrale Rolle in seiner Behandlung. Konventionelle Strahlentherapie mit Röntgenstrahlen ist weit verbreitet, die Verwendung von Protonenstrahlen erfreut sich jedoch aufgrund Ihrer überlegenen physikalischen Eigenschaften zunehmender Beliebtheit. Zur Zeit verwenden die meisten Zentren für Protonentherapie eine passive Streutechnik (*passive scattering*), der Grossteil der in Bau und in Planung befindlichen Zentren wird jedoch auf die fortschrittlichere Technik der magnetischen Deflektion von dünnen Teilchenstrahlen (*pencil beam scanning*) setzen. Diese Technik verspricht weitere Verbesserungen in der Genauigkeit der Behandlung, lässt aber noch weitere Fragen offen bezüglich Interferenzeffekten zwischen der Bewegung des Strahls und des Tumors aufgrund der Atmung des Patienten (*interplay effect*).

Um die Vorteile von *pencil beam scanning* optimal zu verwenden sind bessere Arten der Dosisberechnung in Patienten notwendig. Der zusätzliche Nutzen von Monte Carlo Simulationen zu diesem Zweck wird im ersten Teil der vorliegenden Arbeit quantifiziert. Darin werden klinisch verwendete Methoden zur Dosisberechnung von passiv gestreuten Protonenstrahlen mit Monte Carlo Simulationen und Messungen in einem statischen Thoraxphantom verglichen.

Anschliessend wird der Monte Carlo Code angepasst um die Behandlung mit *pencil beam scanning* an zwei verschiedenen Zentren zu simulieren, wobei das Energiespektrum der Protonenstrahlen jeweils an Messungen angepasst werden muss. Die geringe Streuung der Protonen in dieser Technik erlaubt es uns die Strahlen erst kurz vor dem Eintritt in den Patienten zu modellieren und wird an Tumoren in unterschiedlicher Lage erfolgreich erprobt.

Darauffolgend wird die Bewegung der Patienten durch vier-dimensionale Computer Tomographie und Bildregistrierung (*deformable image registration*) in die Simulationen integriert. Der sogenannte *interplay effect* wird daraufhin für 10 Patienten und zwei verschiedene Strahlgrössen evaluiert, die denjenigen am Paul Scherrer Institut (PSI = SmallSpots) und Massachusetts General Hospital (MGH = BigSpots) entsprechen. Die statistischen Auswirkungen von Fraktionierung, d.h. der Aufteilung der Behandlung über mehrere Sitzungen, werden ebenfalls abgeschätzt.

Schliesslich werden unterschiedliche vorbeugende Massnahmen gegen den *interplay effect* studiert, insbesondere das mehrmalige Abtasten des Tumors (*rescanning*) und die zeitliche Einschränkung der Behandlung auf gewisse Phasen im Atmungzyklus (*gating*). Die Verhinderung dieses Effektes auch für einzelne Bestrahlungssitzungen wird immer wichtiger, da klinische Behandlungprotokolle zu immer weniger Sitzungen tendieren (*Hypofraktionierung*). Die Resultate zeigen unter welchen Randbedingungen rescanning und gating die geplante Dosisverteilung im Tumor wiederherstellen können und wann diese Methoden unzureichend sind.

Die vorliegende Arbeit untersucht die unerwünschten Effekte, die sich aus dem Zusammenspiel von Tumor- und Strahl-Bewegung ergeben können, mittels Monte Carlo Simulationen. Die vielversprechenden Resultate zeigen Möglichkeiten auf diesen *interplay effect* zu mindern und sind ein wichtiger Schritt zur Behandlung von mobilen Lungenkarzinomen mit magnetisch deflektierten Protonenstrahlen.

Contents

List of Abbreviations . . . i
List of Tables . . . iii
List of Figures . . . ix

1 Introduction 1
- 1.1 Proton Therapy: Background and Significance . . . 1
  - 1.1.1 Delivery Techniques . . . 3
  - 1.1.2 Biological Effect of Protons . . . 5
- 1.2 Treatment of Lung Cancer . . . 5
  - 1.2.1 Proton Therapy in the Treatment of Lung Cancer . . . 7
- 1.3 The Interplay Effect . . . 7
- 1.4 Structure & Aims . . . 8

2 Materials and Methods 11
- 2.1 Physical Interactions of Protons with Matter . . . 11
  - 2.1.1 Stopping Theory . . . 12
  - 2.1.2 Scattering Theory . . . 13
  - 2.1.3 Nuclear Interactions . . . 15
  - 2.1.4 Analytical Model of the Bragg Peak . . . 16
- 2.2 Monte Carlo Simulations . . . 18
  - 2.2.1 Physics Models . . . 18
  - 2.2.2 TOPAS: TOol for PArticle Simulations . . . 19
- 2.3 Treatment Planning & Optimization . . . 19
  - 2.3.1 Pencil Beam Algorithm . . . 20
- 2.4 Deformable Image Registration . . . 23
- 2.5 Evaluating Inhomogeneous Dose Distributions . . . 26

3 Dose Calculation Accuracy for Proton Therapy in Lung 29
- 3.1 Study Details . . . 30
  - 3.1.1 Phantom Study . . . 30
  - 3.1.2 Patient Cohort . . . 31
- 3.2 Dose to Target . . . 33
- 3.3 Beam Range in Patients . . . 34
- 3.4 Discussion . . . 35
  - 3.4.1 Impact of MC Dose Calculation on Dose to Target and Critical Structures . . . 36
  - 3.4.2 Impact of MC Dose Calculation on Range Uncertainty and Associated Margins . . . 37
  - 3.4.3 Clinical Impact . . . 38
- 3.5 Conclusion . . . 38

4 Active Scanning Monte Carlo Simulations 39
- 4.1 Validity of Phase Space based MC Simulations 40
- 4.2 Calibration in Water Phantom 42
  - 4.2.1 Derivation of Input Parameters 42
  - 4.2.2 Comparison to Depth-Dose Measurements 43
- 4.3 Translation TPS to Phase Space 45
  - 4.3.1 Patient Simulations 46
- 4.4 Discussion 49
- 4.5 Conclusion 50

5 Quantifying the Interplay Effect in Patients 51
- 5.1 Tumor Motion in Radiotherapy Patients 54
- 5.2 Study Details 54
  - 5.2.1 Treatment Planning 55
  - 5.2.2 Active Scanning Delivery System 56
  - 5.2.3 Monte Carlo Simulation and Post-Processing 56
  - 5.2.4 Simulation of Fractionation: the n-fraction approximation . . 58
  - 5.2.5 Metrics to assess the Interplay Effect 59
- 5.3 Results 60
  - 5.3.1 Interplay Effect in the Normal Lung 60
  - 5.3.2 Interplay Effect in the Target: Dose Distribution 61
  - 5.3.3 Interplay Effect in the Target: TCP 62
- 5.4 Discussion 64
- 5.5 Conclusion 65

6 Mitigating the Interplay Effect in Patients 67
- 6.1 Study Details 67
  - 6.1.1 Motion Mitigation Techniques 69
- 6.2 Results 71
  - 6.2.1 Effect of Motion Mitigation in Tumor 71
  - 6.2.2 Effect of Motion Mitigation in Lung Tissue 73
- 6.3 Discussion 73
- 6.4 Conclusion 77

7 Conclusion and Outlook 79
- 7.1 Experimental Validation and Implementation of Monte Carlo simulations 79
  - 7.1.1 Clinical Impact 80
- 7.2 Interplay Effect in Patients and Countermeasures 80
  - 7.2.1 Clinical Impact 81
- 7.3 Outlook 81
  - 7.3.1 Monte Carlo Methods in a Clinical Environment 81
  - 7.3.2 Treatment of Moving Targets 82

Bibliography **83**

List of Abbreviations

2y-LC	Local Control after 2 years
AP	Anterior-Posterior
ave-IP	average Intensity Projection
BED	Biologically Equivalent Dose
CTV	Clinical Target Volume
CW	Chest Wall
CT	Computer Tomography
DVH	Dose Volume Histogram
EUD	Equivalent Uniform Dose
eV	electron volt ($\approx 1.6 \cdot 10^{-19}$J)
GTV	Gross Tumor Volume
Gy	Gray [J/kg]
Gy(RBE)	Gray corrected for relative biological effectiveness of radiation
HU	Hounsfield Unit
IMPT	Intensity Modulated Proton Therapy
ITV	Internal Target Volume
MC	Monte Carlo
MCO	Multi-Criteria-Optimization
MCS	Multiple Coulomb Scattering
MGH	Massachusetts General Hospital
MLD	Mean Lung Dose
MIP	Maximum Intensity Projection
PB	Pencil Beam
PSI	Paul Scherrer Institute
PSPT	Passive Scattering Proton Therapy
PTV	Planning Target Volume
RBE	Relative Biological Effectiveness
SOBP	Spread Out Bragg Peak
SI	Superior-Inferior
TCP	Tumor Control Probability
TOPAS	TOol for PArticle Simulations
TPS	Treatment Planning System
VX	Percentage of structure receiving more than X Gy
WED	Water Equivalent Density

List of Tables

5.1 Studies reporting tumor motion for lung cancer patients undergoing radiotherapy. . . . 53
5.2 Patient characteristic: motion amplitude (peak to peak), tumor volume and average delivery time per field. . . . 55

6.1 Patient characteristics in rescanning study: tumor size, location, axis of main motion and motion amplitude. Tumor location encoded as [R/L][L/M/U][L] = [Right/Left][Lower/Medium/Upper]Lobe of Lung. SI = Superior-Inferior, AP = Anterior-Posterior. . . . 68
6.2 Simulation results of all patients for the large spot size (top part) and the small spot size (bottom). All values are in percent of the prescribed EUD in the static plan. . . . 74

List of Figures

1.1 Original figure from Wilson's publication on the radiological use of fast protons. The dotted curve shows the dose deposition for a single 140MeV proton, the full curve a qualitative estimation for a beam of monoenergetic protons of that energy [142]. 1

1.2 Energy deposition as a function of depth for 15 MV photons and a proton spread out Bragg peak. The tumor is marked in red and the red lines indicate an "ideal" dose distribution, delivering a uniform dose solely to the target [127]. 2

1.3 Schematic representation of passive scattering, showing the range shifter modulating the beam in depth and the scatter foils spreading it laterally. Collimator and Compensator then conform the beam to the target, though high proximal dose remains due to the constant modulation width. Figure courtesy of Silvan Zenklusen (NIRS, Chiba). 3

1.4 Schematic representation of active scanning: the sweeper magnets deflect the beam laterally and the degrader switches the energy to irradiate multiple layers. Figure courtesy of Silvan Zenklusen (NIRS, Chiba). 4

1.5 Example of Intensity Modulated Proton Therapy: the ensemble of inhomogeneous dose distributions cover the target homogeneously while sparing the spinal cord in its middle. Figure courtesy of Jan Unkelbach (Harvard Medical School, MGH). 5

1.6 Annual age-adjusted rates of cancer for males in the United States [61] 6

1.7 Comparison between passive scattering (**left**) and active scanning (**right**) in a lung cancer patient. The green contour indicates the tumor to be treated [149]. 7

1.8 Two dose distributions in the patient. **Left:** simulated on the static CT **Right:** simulated on the 4D-CT including respiratory motion. The orange contour shows the position of the target at the end of exhalation and the yellow contour the envelope of tumor motion over all breathing phases. The color bar is in percent of prescribed dose to the target. 8

2.1 Monte Carlo simulations showing the absorbed dose as a function of depth and its components for a 160 MeV pristine peak in a water phantom. The total absorbed dose is shown as percentage of the total peak dose and the individual components are shown as percentage of total dose at that depth. The distribution is cut at the depth where no primary particle is detected anymore (the total dose deposited at this point is 0.041% of peak dose). 15

2.2 Schematic of pencils j subdivided into bixels $k(j)$, which receive contributions from multiple pencils. Image courtesy of Hanne Kooy (Harvard Medical School, MGH). 22

2.3 Coronal slice view of a right lung at full exhalation **(a)** and inhalation **(b)** from two phases of 4D CT set. The two volumes were registered by B-spline registration using the mean squared error similarity metric. The full inhalation image **(b)** shows the voxel correspondence to the full exhalation image as a superimposed vector field, which was subsampled and projected into two dimensions for the sake of visualization. Figure courtesy of Tony Shackleford (Drexel University). 23

2.4 Dose Volume Histogram of 2 dose distributions with same mean dose to the structure, yet different degrees of homogeneity within the volume of interest. The dotted lines signify the D_{95} and D_5 of each distribution, i.e. the minimum dose to that is given to 95% or 5% of the volume. The spread between the values can be taken as a measure of dose homogeneity (D_{5-95}). 26

3.1 Explanation of experimental setup and measurements for various depths. (A1) middle part of lung phantom on ionization chamber array. (A2) CT of the phantom with planned dose distribution. (B1-2) Measurement results in planes proximal and distal to the target. (C1-2) Line profiles through the central axis of (B1-2), shown together with the predictions of Monte Carlo and the Pencil Beam Algorithm. 30

3.2 Experimental setup and results (A) Lung slabs (cedar wood) and chest wall (lucite) positioned on the 2D-array of ionization chambers. (B) CT of the phantom with GTV (full) and CTV (dashed) contours. (C) Modified phantom with chest wall, showing also the 2 halves of the embedded tumor. (D) Measurement results in central plane of target (right) together with prediction of TPS (left) and Monte Carlo (middle). (E) Line profile through the central axis of the tumor, with magnifications for target periphery (top right) and penumbra (lower right). Error bars for measurement 1.5%, for MC 1% (shaded blue). 32

3.3 Summary of the patient study. (A) Mean target dose difference (MC-TPS) in % of prescribed dose plotted against the size of the aperture opening. (B) Changes in MLD, V5 and V10 in percent of planned values as a function of tumor volume. (C-F) Example field: TPS dose (C), MC dose (D), DVHs (E) and dose difference (F=C-D). All color bars are percentages of prescribed dose, transparent <0.1%. Orange/blue contours represent the GTV/CTV. 33

3.4 Experimental verification of proton range using a heterogeneous lung phantom (shown in Fig 3.2C): prediction of TPS (A), MC (B), difference MC-TPS (C). Red areas in (C) indicate higher dose predicted by MC. All color bars are percentages of prescribed dose, transparent $<0.1\%$. (D) Histograms representing the difference in measured Range50 compared to MC (top, blue) and the TPS (bottom, red). The vertical lines represent range margins discussed in [99]: 2.4%+1.2mm (solid blue), 4.6%+1.2mm (solid red), 3.5%+1mm (dashed red). 34

3.5 Example of underestimated range in a patient by an analytical dose calculation algorithm. Dose calculation by TPS (A), MC (B) and difference MC-TPS (C). Red areas in (C) indicate higher dose predicted by MC. (D) shows the dose-volume-histograms of spinal cord and CTV for the MC and TPS dose distributions. All color bars are in percent of prescribed dose. Contours shown are the GTV (pink), CTV (green) and spinal cord (red). 35

3.6 Left: Dose profile of TPS and MC along the horizontal axis of the dose distribution in figures 2C-D Right: Visualization of the impact of tissue density on the range margin (cyan area). Both fields have the same (water-equivalent) range and therefore range margin, indicated in cyan, yet the margin of the superior field is enlarged by a factor ≈ 3. 36

3.7 Factors leading to lower mean dose to the target. Left: distance chest wall-tumor. Right: range of proton field in water. CW=chest wall. . 37

4.1 Full nozzle versus phase-space based simulations for a 12x12cm field of 91.015 MeV protons. Fluence in air at isocenter in relative units for phase-space based (A) and full nozzle (B) simulations. (C) profile through the central axis, full black line indicating phase-space based results from (A), red dotted line full nozzle results from (B). The scale is in log relative fluence, inset in linear scale. 40

4.2 **Top**: fluence in air at isocenter for the full nozzle simulations of a 230MeV beam: protons and electrons (top left), secondary protons only and neutrons (top right). **Bottom**: energy spectra for protons, electrons, photons and neutrons at nozzle exit. 10^9 protons were simulated entering the nozzle in these simulations. 41

4.3 (a) Distal range80 of a set pristine Bragg peaks plotted against energy in a water phantom calculated with TOPAS. (b) width80 in mm of that same dataset, shown together with measurement data of PSI (circles) and MGH (squares). 42

4.4 Predictions of the analytical model (as discussed in chapter 2.1.4) for the increase in width80 with energy spread (in percent of initial energy) for different energies. 43

4.5 (a) energy spreads according to the fit of the analytical model to the measured width80. Energy spread in percent of initial energy plotted as a function of energy. The red line represents of cubic Derived polynomial fit to the values 44

4.6 TOPAS simulations (blue lines) compared with measurement points (red stars) for the calibration dataset from MGH. The simulations are plotted in units of $Gy(RBE)mm^2Gp^{-1}$, the measurements are normalized to the maximum dose of the simulations. The lower part shows magnifications of the first, third and sixth peak. 44

4.7 (Differences in range80 (squares) and width80 (crosses) in mm between the TOPAS simulations and the measured depth dose distributions for different ranges. 45

4.8 Top row: anterior-posterior field in liver patient, structures on display are the clinical target volume (CTV, pink) and the planning target volume (PTV, blue). Middle row: head and neck patient, visible structures are gross tumor volume (GTV, green) and CTV (blue). Lower row: lung patient, red line indicates the CTV. All values given are Gy(RBE). The scale of the difference image on the right is 10% of prescribed dose for row 1 and 2, while 30% for row 3. Red areas in the diff(MC-PB) images indicate higher dose in the MC simulations, blue areas higher dose in the TPS. 47

5.1 Spectrum of motion amplitudes based on the studies in table 5.1. . . 54

5.2 Energy-dependent spot size for the gantry at MGH (blue) and PSI Gantry 2 (red). PSI values are the minimum values achievable and might be slightly larger in clinical practice. 56

5.3 Study design in detail. Red roman numerals denote the processes: treatment planning (I), scripts for 3D simulation (II) and for 4D simulation (III). 57

5.4 Sagittal view of the dose distributions for patient 1 with CTV in end-exhale phase (red, small contour) and ICTV (pink, large contour). a-d denote the 1-fraction cases for the 4 initial phases, e the n-fraction and f the static case. 58

5.5 Percentage of healthy lung receiving 20Gy(RBE) or more, plotted against tumor motion amplitude. Squares denote BigSpots (BS), triangles SmallSpots (SS), full blue symbols the static values and open red ones the 1 fraction average. 60

5.6 D_{min} (blue), D_{max} (red) and D_{mean} (green) values for the CTV for the 1-fraction (open symbols) and n-fraction (closed symbols) case. The open and closed D_{mean} symbols coincide. The error bars for the 1-fraction values represent the standard deviation of the 4 initial phases. The shaded areas represent a linear fit through the maximum and minimum values among the initial phases to guide the eye. . . . 61

5.7 D_{5-95} values for the CTV for the 1-fraction (open symbols) and n-fraction (closed symbols) case for BigSpots (squares) and SmallSpots (triangles). Blue symbols denote the static case. The error bars for the 1-fraction values represent the standard deviation of the 4 starting phases. The lines represent a linear fit through the 1-fraction values to guide the eye (full line: BigSpots, dotted line: SmallSpots). 62
5.8 EUD values as function of motion amplitude for static (blue symbols), 1-fraction average (open symbols) and n-fraction (closed symbols) case. The error bars for the 1-fraction values represent the standard deviation of the 4 initial phases. 63
5.9 2y-LC for the static (blue symbols), 1-fraction average (open symbols) and n-fraction (closed symbols) case. The error bars for the 1-fraction values represent the standard deviation of the 4 initial phases, and the cross denotes the worst 1-fraction result. 63

6.1 Example of dose distributions through the transverse slice after 4D-simulation for different motion mitigation approaches: (A) no motion mitigation, (B) 2x-layered rescanning, (C) 6x-layered rescanning, (D) 2x breath-sampled rescanning and gating (E). (F) shows the nominal, i.e. expected, distribution without any motion, simulated on the planning CT. The color bar is in percent of prescribed dose, the contours represent the GTV (orange) and the CTV (magenta). . . . 70
6.2 Results for patient 3: EUD (top), D_{99} (middle) and D_{5-95} (bottom). Triangles denote layered rescanning, squares volumetric rescanning, circles breath-sampled rescanning (BSR) and diamonds gating. The values for EUD and D99 are relative to the static dose distribution. Error bars represent the standard deviation from the 4 starting phases studied for each rescanning setting. Layered and volumetric symbols have been slightly offset to ease differentiation. 72
6.3 Example for synchronization effect in rescanning (patient 2), note the increase in interplay effect for 4x volumetric rescanning. EUD (top), D_{99} (middle) and D_{5-95} (bottom). Triangles denote layered rescanning, squares volumetric rescanning, circles breath-sampled rescanning (BSR) and diamonds gating. The values for EUD and D99 are relative to the static dose distribution. Error bars represent the standard deviation from the 4 starting phases studied for each rescanning setting. Layered and volumetric symbols have been slightly offset to ease differentiation. 75

Chapter 1

Introduction

Contents

1.1 Proton Therapy: Background and Significance 1
1.1.1 Delivery Techniques 3
1.1.2 Biological Effect of Protons 5
1.2 Treatment of Lung Cancer 5
1.2.1 Proton Therapy in the Treatment of Lung Cancer 7
1.3 The Interplay Effect 7
1.4 Structure & Aims 8

1.1 Proton Therapy: Background and Significance

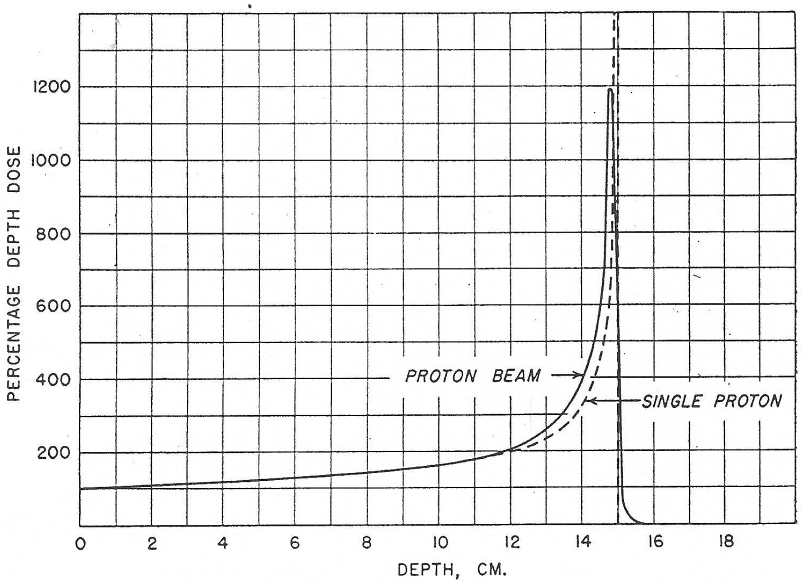

Figure 1.1: Original figure from Wilson's publication on the radiological use of fast protons. The dotted curve shows the dose deposition for a single 140MeV proton, the full curve a qualitative estimation for a beam of monoenergetic protons of that energy [142].

The use of protons to treat cancer was first suggested by Robert Wilson 1946 in his seminal publication [142], in which he noted

> "It will be easy to produce well collimated narrow beams of fast protons, and since the range of the beam is easily controllable, precision exposure of well defined small volumes within the body will soon be feasible."

Figure 1.1 from his original publication demonstrates the physical characteristics of proton energy loss, namely the finite range of penetration and their relatively low initial energy loss at the surface that increases towards the end of their range, leading to a narrow region of high ionization density, termed the *Bragg peak*. The interactions of protons and the reasons for these characteristics will be discussed in detail in chapter 2.1

Soon thereafter, first investigations into the biological effects of protons were undertaken at the University of California, Berkeley, and the first patients were treated from the 1950's on in Berkeley, Sweden and the Soviet Union [2]. Up to this date, over 90'000 patients have been treated with protons worldwide and the number of centers employing protons or other charged ions is steadily increasing[1].

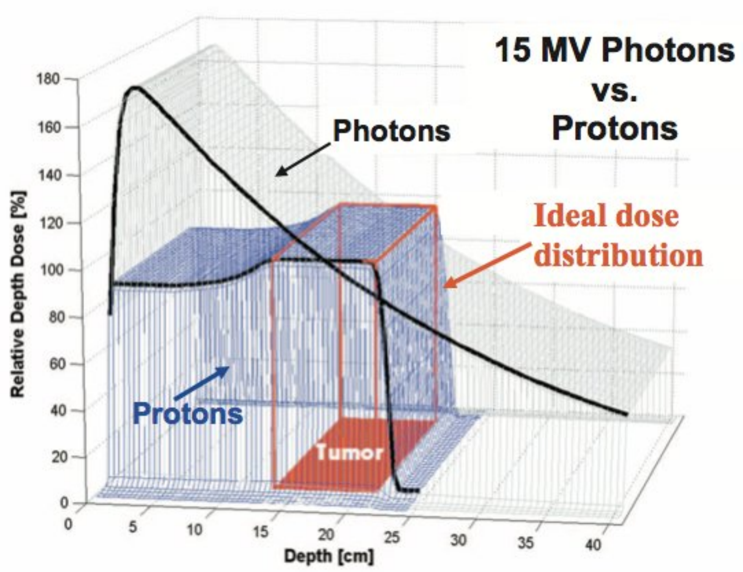

Figure 1.2: Energy deposition as a function of depth for 15 MV photons and a proton spread out Bragg peak. The tumor is marked in red and the red lines indicate an "ideal" dose distribution, delivering a uniform dose solely to the target [127].

In order to deliver a homogeneous dose, i.e. energy deposition, to a specific volume, many individual Bragg peaks of different energies can be weighed together to create a so called spread out Bragg peak (SOBP), as visualized in figure 1.2. It shows the dose deposition as a function of depth in water for a proton SOBP and a photon beam for comparison. Photons have an initial build-up over the first millimeters, after which they deposit an exponentially decreasing dose, delivering significant amounts of dose proximal and distal to the target. Protons on the other hand deposit less dose before and no dose after the target due to their finite range.

---

[1] For a list of particle therapy center currently in planning and operating, please visit the homepage of the Particle Therapy Co-Operative Group (PTCOG) at http://ptcog.web.psi.ch.

After acceleration to high enough energy, protons typically form a nearly mono-energetic beam of small lateral size and angular divergence. To be useful to treat extended volumes in patients the beam has to be spread laterally and in depth, as described in the next chapter.

1.1.1 Delivery Techniques

Two main approaches exist for spreading the beam laterally and in depth in order to irradiate the target in proton therapy, *passive scattering* and *active scanning*.

1.1.1.1 Passive Scattering

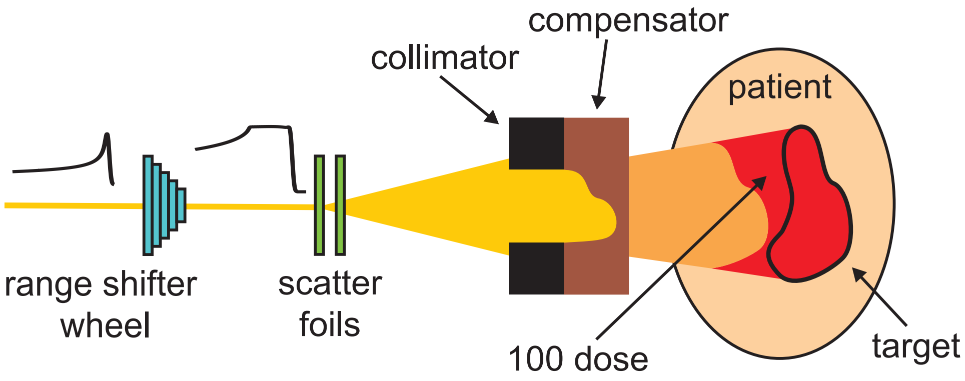

Figure 1.3: Schematic representation of passive scattering, showing the range shifter modulating the beam in depth and the scatter foils spreading it laterally. Collimator and Compensator then conform the beam to the target, though high proximal dose remains due to the constant modulation width. Figure courtesy of Silvan Zenklusen (NIRS, Chiba).

In passive scattering the lateral spread of the protons is produced by placing scattering foils in the beam to provide a near uniform fluence across the field, as shown schematically in figure 1.3.

As the resulting angular distribution after scattering in a single foil is Gaussian, one either has to place the scatterer far upstream and only include the central part of the field, or place a second scatterer in the beam to make the fluence uniform [71]. The former approach requires a large drift distance and results in low efficiency of the beam used, as most of the protons are removed from the field. The latter, more popular, approach includes a second scatterer which is made of a combination of high- and low-Z materials to ensure the same energy loss of all protons and a spatially uniform fluence.

To provide uniformity of irradiation in depth, the nearly mono-energetic beam either passes a wheel of varying thickness that rotates in the beam, such as the range shifter wheel in figure 1.3 [70, 142], or a ridge filter constructed from ridges of variable thickness absorbers [76].

After the spreading of the beam to a field homogeneous in depth and laterally, the field is then restricted using a patient- and field-specific collimator and compensator. The collimator restricts the dose to the outline of the tumor in beam's eye view, and the compensator shapes the dose distribution in depth to conform to the distal edge of the tumor.

The SOBP's width in depth however remains constant, leading to over-irradiation of healthy tissue proximal to the tumor, indicated in figure 1.3, which becomes especially important for irregular targets.

In this passive beam dispersal technique the entire volume is essentially irradiated simultaneously, which has advantages in the case of motion as we will discuss in chapter 1.3.

1.1.1.2 Active Scanning

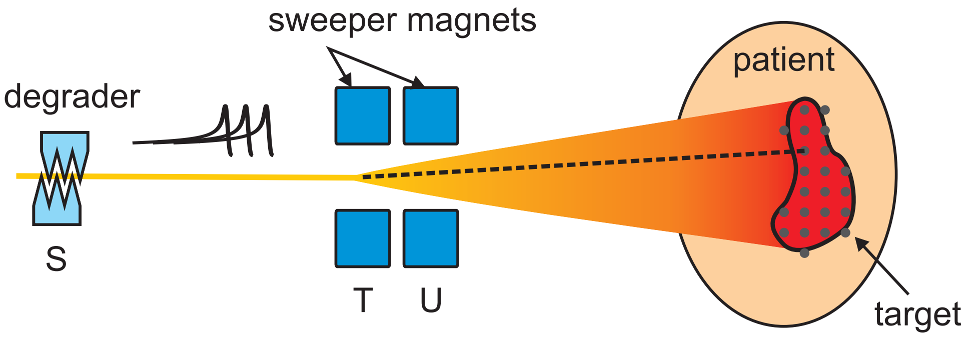

Figure 1.4: Schematic representation of active scanning: the sweeper magnets deflect the beam laterally and the degrader switches the energy to irradiate multiple layers. Figure courtesy of Silvan Zenklusen (NIRS, Chiba).

In Active Scanning, the desired dose distribution is formed by scanning the pencil beam laterally using magnetic fields and in-depth by changing its energy [104]. Shown schematically in figure 1.4, this technique allows conformation in all dimenions and irradiates less normal tissue than passive scattering, especially for targets of irregular geometry. Since there is no need for field-specific hardware (collimators and compensators), multiple fields can be delivered consecutively and the treatment can be adapted more easily in case of geometric changes [128].

The main advantage of this method is the possibility to optimize the fluence of each pencil beam independently, allowing for the delivery of inhomogeneous fields. This so called *Intensity Modulated Proton Therapy* (IMPT) [80] allows for higher conformity and sparing of critical structures in proximity to the target.This is demonstrated in figure 1.5, where the three inhomogeneous dose distributions in the top row cover the target while sparing the spinal cord in its middle.

In this work we focus on *discrete spot scanning*, in which the beam is interrupted between the delivery of single spots to allow for accurate settling of the scanning magnets. In *raster* and *continuous* scanning the beam remains on while scanned laterally, for the latter the beam intensity can vary dynamically as well [2].

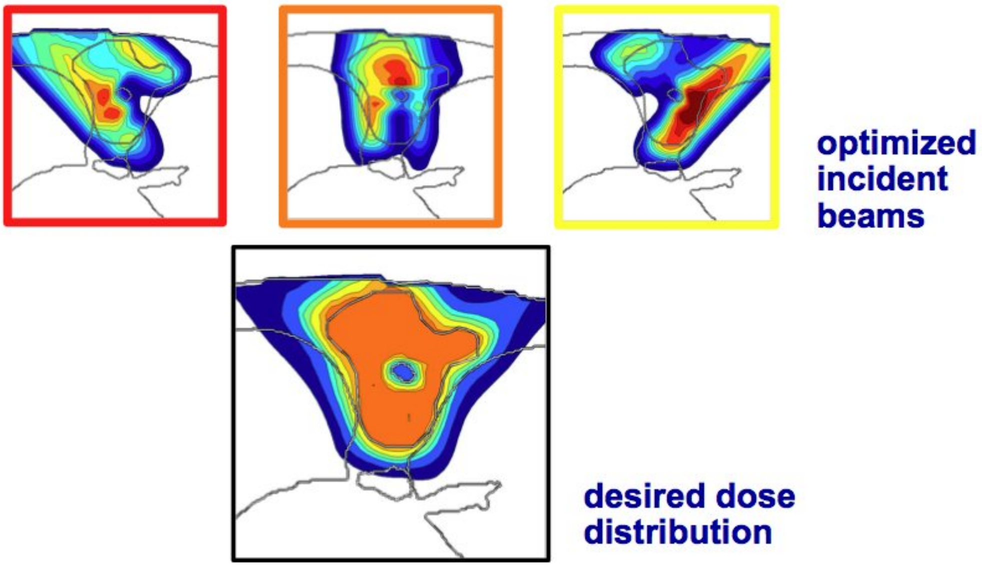

Figure 1.5: Example of Intensity Modulated Proton Therapy: the ensemble of inhomogeneous dose distributions cover the target homogeneously while sparing the spinal cord in its middle. Figure courtesy of Jan Unkelbach (Harvard Medical School, MGH).

1.1.2 Biological Effect of Protons

Different types of radiation do not result in the same biological effect for the same amount of physical dose, which is given in Gray ([Gy] = [J/kg]). To relate biological effects from different types of radiation the concept of *relative biological effectiveness* (RBE) has been introduced. The RBE of a specific kind of radiation is the ratio of the physical doses

$$RBE = \frac{D_{reference}}{D}, \tag{1.1}$$

that produce the same biological effect (for example cell kill), where the reference radiation is usually Cobalt-60 [55]. The RBE therefore normalizes the dose for different types of radiations to give rise to the same biological effect.

As protons lead to different patterns of microscopic energy deposition, their RBE is generally slightly higher than for photons. Even though the exact ratio depends on the energy of the protons and the cell type irradiated among other factors, for clinical purposes we generally assume a fixed RBE of 1.1 [46, 101].

For this reason absorbed doses throughout this thesis are usually denoted by Gy(RBE), i.e. corrected for the relative biological effectiveness of protons.

1.2 Treatment of Lung Cancer

Lung cancer is the most common cancer worldwide, in terms of incidence as well as mortality. The incidence is highest in North America and Europe. In the US, the estimated lung cancer incidence 2008 was 215'000 cases, with a mortality of

161’840 [61], in Europe the figures are 390’900 and 342’100, respectively [41]. Figure 1.6 shows the incidence of common cancers for males in the United States.

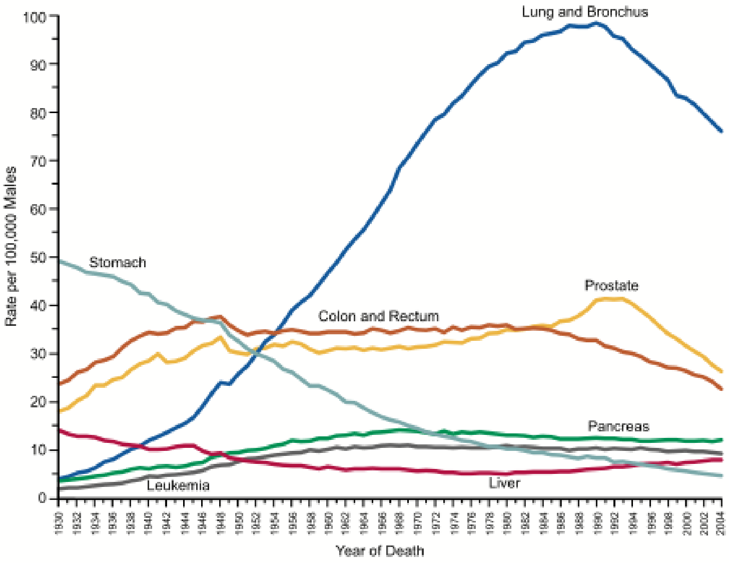

Figure 1.6: Annual age-adjusted rates of cancer for males in the United States [61]

Survival depends strongly on stage, ability to undergo surgery and other factors, but overall the prognosis tends to be poor, with a 5-year overall survival rate of only 10-15% [43].

For early stage lung cancer (i.e. stage I-II), the gold standard remains surgical resection, if the patient’s performance status allows for it and the tumor is judged to be completely resectable. Unfortunately only 30% of lung cancer patients present with early stage disease, in the other 70% the disease has already locally advanced (stage III) or spread metastatically to distant organs (stage (IV).

Radiation therapy plays a significant role in the management of lung cancer since the 1960’s, when a trial by the Veterans administration [143] assessed its role in the treatment of unresectable Non-Small-Cell Lung Cancer (NSCLC).

For radiation therapy of early stage NSCLC, Stereotactic Body Radiation Therapy (SBRT) is now preferentially applied instead of normally fractionated treatments. SBRT usually delivers high biologically equivalent doses ($>$100Gy) in typically $<$5 fractions, and has shown superior local control and overall survival. For centrally located and larger lesions however, SBRT has proven too toxic [22, 97, 136].

For locally advanced disease, concurrent chemo- and radiation therapy is often the treatment of choice. Due to high failure rates the prescribed dose has been escalated over the past decade, with a host of studies now reporting the safety and efficacy of 74 Gy in 2 Gy/fraction in a concurrent setting [16, 29, 116].

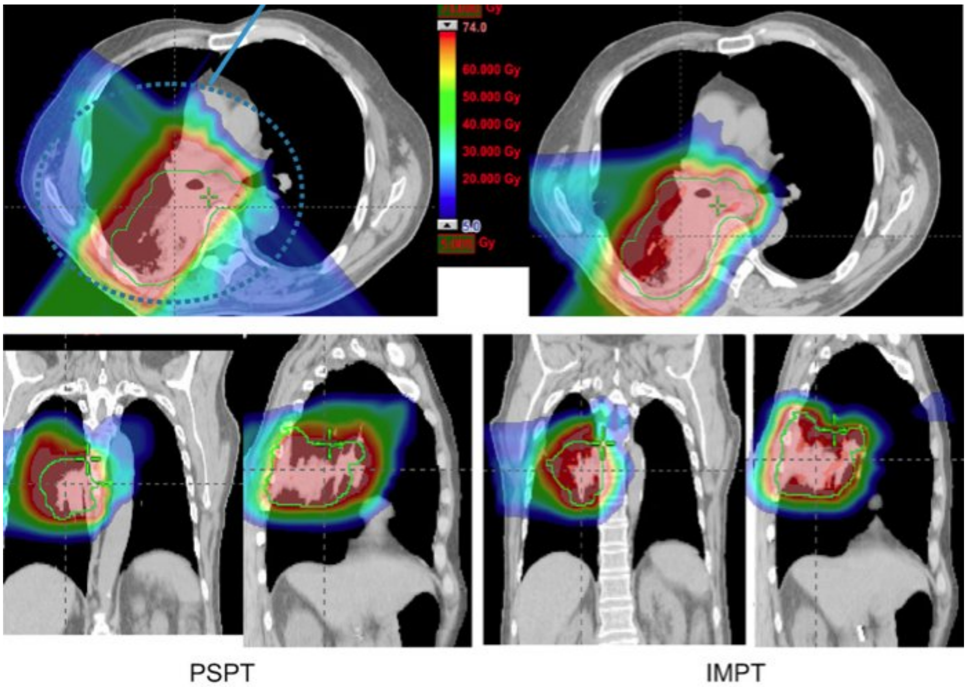

Figure 1.7: Comparison between passive scattering (**left**) and active scanning (**right**) in a lung cancer patient. The green contour indicates the tumor to be treated [149].

1.2.1 Proton Therapy in the Treatment of Lung Cancer

Protons have been shown to improve the dose distribution further due to their superior physical characteristics. Especially IMPT could be able to reduce the dose to the lung and other normal tissues significantly, particularly for complicated cases involving lymph nodes. Therefore IMPT could be used to either further escalate the dose to improve patient outcome or reduce the toxic side-effects of the treatment [149]. Figure 1.7 shows the comparison in an actual lung cancer patient between active scanning on the right and passive scattering on the left, demonstrating the difference in dose conformity and excessive dose to the normal lung in passive scattering.

Furthermore active scanning techniques could be used to adapt the treatment to changes in anatomy, such as tumor shrinkage, which usually increase the dose to the normal lung if not accounted for [58].

1.3 The Interplay Effect

There is increasing interest in treating lung cancer with actively scanned protons, not only to improve treatment outcome and reduce side effects, but also because most proton centers under construction and in planning will only offer active scanning as delivery modality [153].

Targets in the lung, as well as liver and to some extent prostate, exhibit *intra-fractional motion* due to respiration [75]. For passive scattering delivery this can be adequately accounted for by enlarging the treatment field to cover the tumor in every breathing phase, due to the simultaneous nature of the field delivery [65]. Though this approach causes additional irradiation of healthy normal tissue, it is successful in maintaining a homogeneous dose to the tumor and is used at several institutions.

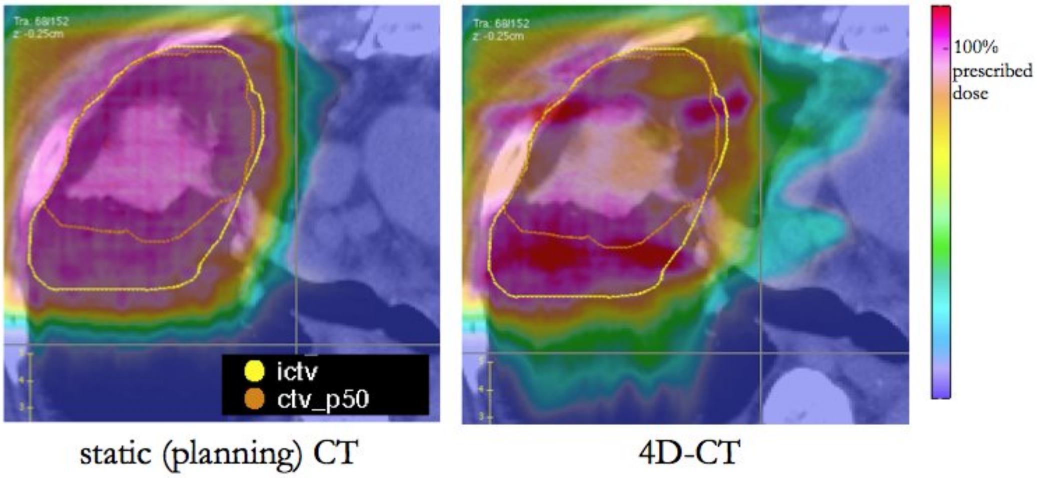

static (planning) CT

4D-CT

Figure 1.8: Two dose distributions in the patient. **Left:** simulated on the static CT **Right:** simulated on the 4D-CT including respiratory motion. The orange contour shows the position of the target at the end of exhalation and the yellow contour the envelope of tumor motion over all breathing phases. The color bar is in percent of prescribed dose to the target.

For active scanning delivery on the other hand, interference between the motion of the pencil beam and the target can cause complex patterns of over- and under-dose within the target, first reported by Phillips *et al* [109]. Figure 1.8 shows the severe dosimetric consequences of this *interplay effect*: on the left is the dose distribution simulated in a static geometry, and on the right a simulation including respiratory motion, showing large areas of lower than expected dose within the target.

Several techniques have been proposed to mitigate this effect [9], for example re-irradiations of the target (rescanning) and restriction of the treatment to certain phases of the breathing cycle (gating). These techniques will be introduced in detail in chapter 6.1.1.

1.4 Structure & Aims

The previous section (chapter 1) served to introduce the merits of proton therapy, introduced the techniques to deliver the treatment and motivates the use of actively scanned protons for lung cancer. Furthermore the main obstacle of introducing the technique of active scanning to the treatment of moving lung tumors has been presented, the *interplay effect*.

The overall goal of this work is the time-dependent Monte Carlo simulation of Lung Cancer patients treated with scanned beams of protons to simulate the interplay effect and investigate methods to mitigate its consequences.

To achieve this goal four aims were realized:

I **Evaluation of Monte Carlo simulations in a static lung phantom for passive scattering**
The next section (chapter 3) first gives an overview over the interactions of protons and further describes the Monte Carlo code used to simulate them (chapter 2.2). Next the clinical algorithm (chapter 2.3) is presented, which is then compared to Monte Carlo simulations and measurements in the first results section (chapter 3).

II **Development of Monte Carlo code for active scanning**
Thereafter we adapt our Monte Carlo code to active scanning simulations (chapter 4), deriving the energy spread with the help of an analytical model (described in chapter 2.1.4) and performing first patient simulations of active scanning treatments (chapter 4.3.1).

III **Time-dependent patient simulations of active scanning to quantify the interplay effect**
For simulations in moving targets we need methods to map between motion states (deformable image registration, chapter 2.4) and to evaluate the resulting inhomogeneous dose distribution (chapter 2.5). Subsequently time-dependence of the patient CT is introduced into the Monte Carlo simulations (chapter 5) and the interplay effect is quantified for 2 different pencil beam sizes in 10 patients.

IV **Mitigation of the interplay effect**
Finally, various techniques (chapter 6.1.1) to mitigate the dosimetric consequences of motion are tested in patients that have shown a significant interplay effect and the results presented in chapter 6.

Chapter 2

Materials and Methods

Contents

2.1 Physical Interactions of Protons with Matter 11
2.1.1 Stopping Theory 12
2.1.2 Scattering Theory 13
2.1.3 Nuclear Interactions 15
2.1.4 Analytical Model of the Bragg Peak 16
2.2 Monte Carlo Simulations 18
2.2.1 Physics Models 18
2.2.2 TOPAS: TOol for PArticle Simulations 19
2.3 Treatment Planning & Optimization 19
2.3.1 Pencil Beam Algorithm 20
2.4 Deformable Image Registration 23
2.5 Evaluating Inhomogeneous Dose Distributions 26

This section gives first an overview over the interactions of protons in matter (chapter 2.1), followed by how they were simulated with Monte Carlo methods (chapter 2.2) and finally how the dose distributions are calculated in the clinic (chapter 2.3).

Chapter 2.4 describes deformable image registration, which is necessary to compute the dose to a moving geometry and 2.5 introduces metrics to analyze such deformed dose distributions in the patient.

2.1 Physical Interactions of Protons with Matter

Passing through matter, protons are subject to three main phenomena [47]:

Stopping describes the slowing down and energy loss process, mainly through electromagnetic interactions with atomic electrons.

Scattering results in angular deflections due to electromagnetic interactions with atomic nulei.

Nuclear Interactions are relatively rare compared to the electromagnetic interactions with electrons and nuclei, yet have significant effects on the patterns of energy absorption.

2.1.1 Stopping Theory

Generally the rate of energy loss for charged particles, the *stopping power* S, is expressed as energy lost per unit path length MeV/cm, divided by the density ρ of the material to give the *mass stopping power*

$$\frac{1}{\rho}S = -\frac{\mathrm{d}E}{\mathrm{d}x} = \frac{1}{\rho}S_{col} + \frac{1}{\rho}S_{rad}, \tag{2.1}$$

which can be further subdivided in to a collision and radiative term [152]. S_{rad}, indicating Bremsstrahlung interactions, is negligible for heavier charged particles like protons compared to the collision term S_{col}, why we'll focus on the latter.

In the early 1930's Bethe [13] published a theory in which the energy loss of heavy charged particles in an absorber is calculated using the Born approximation, which is applied to the collision of the heavy charged particle with atomic orbital electrons. It assumes quantized momentum transfer and was extended to relativistic energies, to yield the *Bethe equation* for mass stopping power

$$\frac{1}{\rho}S_{col} = -\frac{4\pi r_e^2 mc^2}{\beta^2}\frac{1}{u}\frac{Z}{A}z^2 L(\beta), \tag{2.2}$$

where $r_e = e/mc^2$ is the classical electron radius, mc^2 the electron rest energy, atomic mass u, $\beta = v/c$, Z and A atomic number and relative atomic mass of the target atom and z the charge number of the projectile. These first terms give the general features of the interactions of charged particles with matter, while the last term, the *stopping number* $L(\beta)$ describes the fine details. The energy loss due to collisions with electrons is therefore proportional to the charge z^2 and inversely proportional to the velocity v^2 of the projectile

$$\frac{\mathrm{d}E}{\mathrm{d}x} \propto z^2 v^{-2}, \tag{2.3}$$

which already explains the increasing energy deposition with depth resulting in the Bragg peak described in the introduction (figure 1.1).

$L(\beta)$ is usually grouped into a main term $L_0(\beta)$ and additional terms for the Barkas correction (zL_1) and the Bloch correction (z^2L_2). The main term is

$$L_0(\beta) = \frac{1}{2}\ln\left(\frac{2mc^2\beta^2 W_m}{1-\beta^2}\right) - \beta^2 - \ln I - \frac{C}{Z} - \frac{\delta}{2}, \tag{2.4}$$

where I is the mean excitation energy of the target absorber, C/Z the shell correction and $\delta/2$ the density correction factors. W_m is the *maximum* kinetic energy that can be imparted to an electron by a particle with mass M:

$$W_m \approx \frac{2mc^2\beta^2}{1-\beta^2}, \quad \text{if} \quad M >> m. \tag{2.5}$$

In the energy range and dimensions crucial to proton therapy, i.e. around 3-300 MeV, the corrections mentioned above are all small and the main uncertainty comes by far from mean excitation potential I. In principle I can be derived from atomic structure calculations, though these results have been shown not to be sufficiently accurate [152]. In practice I is fitted to experimental results or otherwise interpolated according to theory.

For charged particles stopping in mixtures or compounds *Bragg's additivity rule* is used, which approximates the stopping power by a linear combination of the constituents j weighed by their mass fraction w_j

$$(1/\rho)S_{col} \approx \sum_j (1/\rho)w_j S_{col,j}, \tag{2.6}$$

which is again a good enough approximation for energies in our range, non-linearity only becoming important for very low energies.

For water multiple tabulated stopping power and range tables exist [60, 152], though they differ slightly, leading to an uncertainty in I on the order of 1-2 %.

2.1.1.1 Range and Straggling

As heavy charged particles transfer only small amounts of the incident particle's kinetic energy in individual ionizing collisions, it is convenient to think of the particle that is moving through an absorber as losing its kinetic energy gradually in the so called *continuous slowing down approximation* (CSDA) [7]. Once the stopping power S is know as a function of energy, the CSDA range is defined as

$$R_{CSDA} = \int_0^{E_{i,k}} \frac{\mathrm{d}E \cdot \rho}{S(E)}, \tag{2.7}$$

where $E_{i,k}$ is the initial kinetic energy of the charged particle.

The *mean projected path length* is slightly smaller due to the small angular deflections (described in the next chapter), however the difference is on the order of $\approx 0.1\%$ for clinical energies [60]. This is the reason it makes sense to discuss stopping before multiple scattering, as latter has almost no effect on the slowing down of protons.

As many individual interactions in the absorber affect the particles path, there are statistical fluctuations among the particles even in a mono-energetic beam. Therefore not all of them will stop at the same depth, which is termed *range straggling*. Janni [60] tabulates range straggling for different materials, which only increases slightly for higher Z and is $\approx 1\%$ for light materials [47].

2.1.2 Scattering Theory

While interactions with the atomic electrons hardly deflect fast protons, they are scattered by a multitude of Coulomb interactions with atomic nuclei, termed *Multiple Coulomb Scattering*. The theory behind it was described in the 1940's by Moliere, first for single scattering in the Coulomb field of the nucleus, which is screened by the atomic electrons [87]. He further applies the results to plural scattering, which he defines as "several events", and multiple scattering for very many scatter events [88]. I will just sketch the broad strokes of the theory here, a more involved discussion can be found in [48].

Instead of a single scattering parameter θ_0 as in Gaussian scattering, Moliere introduces two important quantities, the *characteristic single scattering angle* χ_c and the *reduced target thickness* B, which is a dimensionless quantity proportional to the logarithm of the normalized target thickness. These can then be used to define a characteristic multiple scattering angle

$$\theta_M = \frac{1}{\sqrt{2}}(\chi_c \sqrt{B}), \tag{2.8}$$

which plays a similar role as θ_0 in Gaussian scattering.

In the simple case of a thin scatterer, i.e. under the assumption that the incident particle with charge number z, momentum p and speed v does not lose significant energy to change the kinematics, the characteristic single scattering angle is given by

$$\chi_c^2 = 4\pi N_A \left(\frac{e^2}{\hbar c}\right)^2 (\hbar c)^2 \frac{z^2 Z^2}{A} \cdot \frac{t}{(pv)^2}, \tag{2.9}$$

with Avogadro's constant N_A, the fine structure constant $(e^2/\hbar c)$ and the target described by atomic number A, atomic weight Z and its thickness t (in g/cm^3). On average a particle suffers one single deflection $>\chi_c$ in its traversal. Together with the *screening angle* χ_a, which incorporates the Born parameter, B from above is defined as

$$\ln\left(\frac{\chi_c^2}{1.167\chi_a^2}\right) = B - \ln B. \tag{2.10}$$

With a reduced angle variable

$$\theta' \equiv \frac{\theta}{\chi_c \sqrt{B}}, \tag{2.11}$$

Moliere writes the distribution function $f(\theta)$ as a power series in $1/B$ starting with a simple Gaussian:

$$f(\theta) = \frac{1}{2\pi\theta_M^2}\frac{1}{2}\left[2e^{-\theta'^2} + \frac{f^{(1)(\theta')}}{B} + \frac{f^{(2)(\theta')}}{B^2}\right], \tag{2.12}$$

where

$$f^{(n)}(\theta') = \frac{1}{n!}\int_0^\infty y\,dy\, J_0(\theta' y)\, e^{y^2/4}\left(\frac{y^2}{4}\ln\frac{y^2}{4}\right)^n. \tag{2.13}$$

Equations 2.12 and 2.8 can be used to compute the scattering probability density $f(\theta)$ and the multiple scattering angle for targets with $Z \gg 1$. For lighter nuclei, where scattering off atomic electrons plays a role, Bethe [12] proposed a modification of equation 2.9 with $Z(Z+1)$, while Fano [40] in a more exact correction modifies the screening angle χ_a and therefore B.

2.1.3 Nuclear Interactions

Additional to the electromagnetic interactions with electrons and nuclei discussed in the last chapters, protons also interact via the strong interaction with target nuclei [47]. ICRU report 63 differentiates between three kind of nuclear interaction:

elastic reactions refer to those in which total kinetic energy is conserved and the internal states of incident particle and target remain unchanged, i.e. no excitation occurs.

nonelastic are all reactions in which the kinetic energy is not conserved, i.e. the target nucleus might disintegrate and new particles (e.g. alpha particles) can be ejected or particle transfer reactions can take place.

inelastic interactions are actually a sub-class of nonelastic ones in which the final target nucleus is of the same kind as the initial one, but the kinetic energy is not conserved, for example because of excitation of the target nucleus.

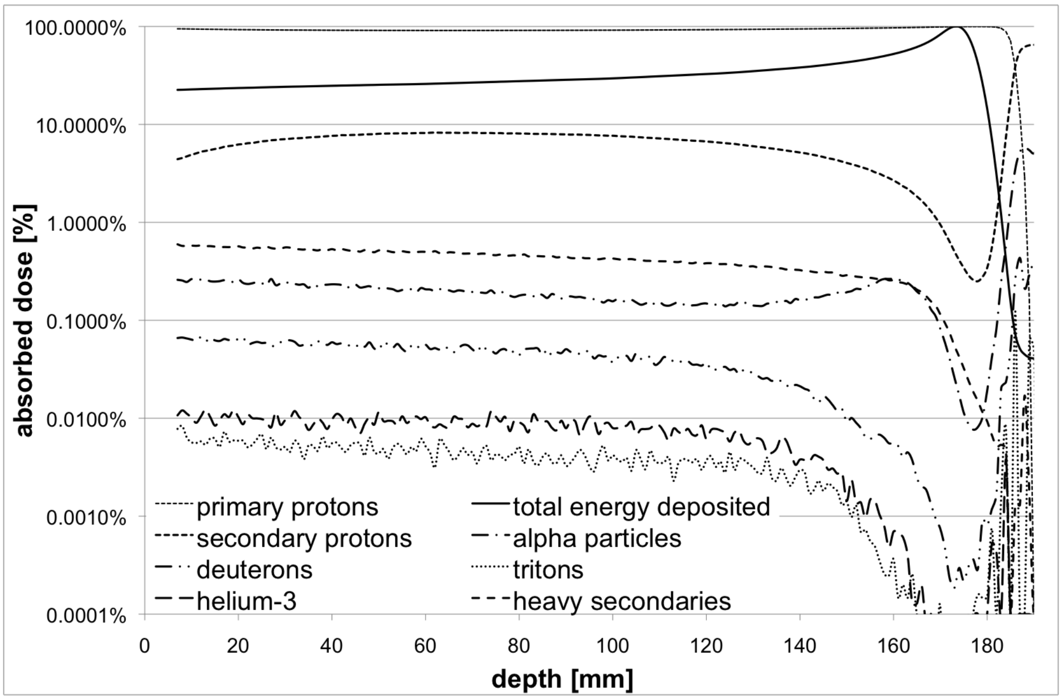

Figure 2.1: Monte Carlo simulations showing the absorbed dose as a function of depth and its components for a 160 MeV pristine peak in a water phantom. The total absorbed dose is shown as percentage of the total peak dose and the individual components are shown as percentage of total dose at that depth. The distribution is cut at the depth where no primary particle is detected anymore (the total dose deposited at this point is 0.041% of peak dose).

Nuclear interactions occur above a proton energy of around 20 MeV at a rate of ≈1% per g·cm^{-2} [14, 60]. Their consequences on the dose distribution are the following:

- They create a *halo* of neutrons, part of which interact outside the field yielding a low dose envelope, while the other part escapes the patient without further interaction, leading to a slight mismatch between the absorbed dose and the initial energy of the protons [115].
- The scattered incident protons and other secondary protons ejected in nonelastic nuclear interactions further contribute to the halo of low dose far out of the primary radiation field [27].
- In the case of target fragmentation heavy nuclei can deposit biologically very effective doses, i.e. with a high RBE, in very close proximity of the interaction.
- They reduce the fluence of primary protons, as already mentioned above.

Figure 2.1 shows the contribution of the different particles to absolute dose by a 160 MeV proton beam simulated in a water phantom as a function of depth. The secondary protons account for up to 8% at a given depth and show a build-up effect due to their forward peaked emission. This includes the contribution of neutrons, which deposit their dose indirectly via secondary protons.

Among the other light secondaries (A<5), only alpha particles cause a significant contribution to the dose deposited, while deuteron, helium-3 and triton are orders of magnitude below. Note the relatively large contribution of heavy secondaries (A>4) to the total dose deposited, i.e. up to 0.6%. Detailed investigations have shown however that the remaining range of these heavy recoil particles is in most cases too small to inflict biological damage [50].

2.1.4 Analytical Model of the Bragg Peak

The energy deposition of charged particles in matter leading to the Bragg peak is well described by the Bethe equation discussed previously. However, this analytical description of the depth-dose curve is not easily integrated [39]. This means numerical methods are typically used to interpolate between Bragg curves or to superimpose them to calculate SOBPs. Bortfeld derived an analytical approximation of the depth dose distribution for protons based on the assumption that the range-energy relationship follows a power-law [14, 15]. Hence we sketch the derivation of this analytical expression here, as we will use it later in chapter 4 to derive the energy spread of the proton beam.

The model is based on a power-law relationship describing the dependency between range and energy

$$R_0 = \alpha E^p, \tag{2.14}$$

with range R_0 and energy E. For range straggling within the medium, a Gaussian distribution of ranges of individual protons within a Bragg peak is assumed. This arises from the statistical nature of the many electromagnetic interactions between the protons and the electrons in the target. Even though multiple Coulomb scattering is expected to render the distribution slightly asymmetric towards lower energies, for protons in a clinical significant energy range this is however a good approximation. Consequently, the Gaussian around the mean depth $\overline{z}(E, E_0)$ with the standard deviation $\sigma_z(\overline{z})$ can be folded into the 'pure' dose distribution $\hat{D}(z)$, in which every proton has the exact same remaining energy (and hence range) at each depth z. The width $\sigma_z(\overline{z})$ of this distribution increases with depth and peaks at $\sigma \equiv \sigma_z(R_0)$. Use of a constant is highly accurate since at low depths, where the real value would differ most, the depth dose profile is very smooth, such that the effects of folding a Gaussian are mitigated, allowing us to write the depth dose curve as

$$D(z) = \frac{1}{\sqrt{2\pi}\sigma} \int_{-\infty}^{R_0} \hat{D}(z) e^{\frac{-(z-\overline{z})^2}{2\sigma^2}} d\overline{z}, \tag{2.15}$$

where $\hat{D}(z)$ is the dose distribution of a mono-energetic beam and $\sigma \equiv \sigma_z(R_0)$. This still assumes the proton beam is initially mono-energetic, while the beam at nozzle exit of a proton therapy beamline will typically consist of two major components: a Gaussian peak around E_0 and a tail towards lower energies, coming from scatter of components in the beam transport and energy selection systems. Since we are interested in the area around the peak, the impact of the low-energy tail of the distribution will be negligible in our calculations and thus we will focus on the Gaussian. Assuming a small standard deviation $\sigma_{E,0} \ll E_0$, the power-law governing the range-energy relation can be linearized around E_0, permitting us to write it as a range spectrum using 2.14, added to that of the mono-energetic beam

$$\sigma^2 = \sigma^2_{mono} + \sigma^2_{E,0} \left(\frac{dR_0}{dE_0} \right)^2 = \sigma^2_{mono} + \sigma^2_{E,0} \alpha^2 p^2 E_0^{2p-2}. \tag{2.16}$$

Including a linear model for the fluence reduction based on Janni's tables [60], the depth dose curve can be written using the gamma function $\Gamma(x)$ and the parabolic cylinder functions $\Delta_y(x)$ as

$$D(z) = \Psi_0 \frac{e^{-\zeta/4} \sigma^{1/p} \Gamma(1/p)}{\sqrt{2\pi} \rho p \alpha^{1/p} (1 + \beta R_0)} \times \left[\frac{1}{\sigma} \Delta_{-1/p}(-\zeta) + \left(\frac{\beta}{p} + \gamma\beta \right) \Delta_{-1/p-1}(-\zeta) \right], \tag{2.17}$$

with

$$\zeta = \frac{R_0 - z}{\sigma}, \tag{2.18}$$

where Ψ_0 is the primary fluence, b is the slope parameter of the fluence reduction relation and γ the fraction of locally absorbed energy from nuclear interactions. The parameters α and p stem from the range-energy relationship in 2.14.

With this analytical expression it is now possible to relate the shape of a measured depth dose distribution directly to the initial energy spread, which will be used in chapter 4 to derive the input parameters necessary for the Monte Carlo simulations.

2.2 Monte Carlo Simulations

Monte Carlo Simulations offer numerical solutions to the behaviour of macroscopic systems through simulations of its microscopic interactions. A solution is determined by random sampling of the probability density functions, and as the number of individual events (histories) increases, the reported average behaviour of the system improves, i.e. its statistical uncertainty decreases.

The Geant4[1] Monte Carlo toolkit [3] provides a computational environment to simulate the passage of particles through matter. It is being developed in a collaboration led by CERN[2] and is geared towards high energy physics. The physics processes cover a wide range, including electromagnetic, hadronic and optical processes in an energy range from several TeV down to in some cases $250eV$, depending on the model.

2.2.1 Physics Models

Geant4 offers a wide range of models for various physical interactions in different energy ranges, which can have a significant effect on the ensuing simulations. The exact physics models used in the simulations have been validated against measurements for protons of clinical energies [147].

2.2.1.1 Electromagnetic

Electromagnetic processes model the interaction of photons and charged particles: multiple scattering, photoelectric effect, Compton scattering, ionization, Bremsstrahlung, Rayleigh scattering, positron annihilation, Cherenkov effect, synchrotron and transition radiation, Auger emission, refraction, reflection, absorption, scintillation and fluorescence. The analytical model used is derived directly from QED calculations and applied down to $1keV$, neglecting the binding energy of atomic electrons (except for the photoelectric effect) and the recoil momentum of the nucleus. We used the low-energy extension, which accounts for atomic and shell effects down to $250eV$.

The energy loss and ionization of hadrons above $2MeV$ is described by the Bethe formula, as described in the last chapter. Below $2MeV$ a parametrization based on ICRU49 [1] is used down to $1keV$.

A condensed history algorithm is employed for multiple scattering [138], which calculates the angular and spatial distribution of the scattered particle without using the Moliere formalism [88].

2.2.1.2 Hadronic

Inelastic scattering is modeled by different formalisms applied to the different stages of the interaction.

---

[1] GEometry ANd Tracking

[2] Centre Europeenne pour la Recherche Nucleaire = European Organization for Nuclear Research

Intra-nuclear cascade: Primary (projectile) interacts with the nucleons residing in the target in a series of two-particle collisions, leading to an intra-nuclear cascade. For this stage the *G4BinaryCascade* [42] model is used, which is valid in the range $100 MeV$-$10 GeV$. The implemented cross sections are parameterizations of experimental data from the Particle Data Group [54].

De-excitation of the pre-equilibrium state nucleus is simulated by the *G4PreCompoundModel*, which is applied to nuclei $<100 MeV$ until equilibrium is reached. The nucleons are viewed as 'exciton' states that are not in ground state and whose number defines the state of the nucleus. Additional to interactions between excitons light ions can be emitted from the nucleus (up to ^{4}He). When all transitions are equally probable the nucleus has reached statistical equilibrium, which invokes the next stage.

De-excitation of the equilibrium state nucleus: compound nucleus further de-excites until energy-cutoff is reached, modeled by *G4VEvaporation*. Nucleus is defined through mass, charge and excitation energy, which can be above the separation energy, leading to further emission of particles.

Elastic scattering is modeled by combining the *G4UHadronElasticProcess* [59] with the *G4HadronElastic* model, which includes an additional dataset for the scattering of nucleons off hydrogen.

2.2.2 TOPAS: TOol for PArticle Simulations

We used TOPAS [107], a toolkit layered on top of Geant4, for all Monte Carlo simulations. TOPAS is aimed at medical physics applications and includes important features, such as material conversion for computer tomography (CT) datasets and efficient voxel navigation [119].

The patient CT contains the geometrical information needed for tracking the particles in Hounsfield Units (HU), which are related to the attenuation coefficient of the diagnostic x-rays used in the CT scanner. To model the interactions in Monte Carlo simulations however, the exact chemical composition and mass density is needed to calculate the cross section for various physics processes. We use a conversion from HU to human tissues based on [117], which uses 26 elemental material compositions to describe the patient anatomy. Each tissue is given a varying density as function of HU, leading to over 3000 distinct materials, from air (HU=-1000) to titanium (HU=3061), as described in [100].

2.3 Treatment Planning & Optimization

Treatment planning is the process of simulating a given arrangement of beams and their weighing factors, a *treatment plan*, in a specific patient anatomy based on imaging studies. Usually the planning is done on CT studies with additional delineation of target volumes and organs at risk (OAR).

For the patient study described in chapter 3, clinical medical physicists planned the treatments using *XiO* (Computerized Medical Systems). These plans were optimized manually, as the planners select appropriate beam angles and weights by hand. For the pencil beam treatments calibrated in chapter 4 and simulated in chapters 5&6, we use ASTROID [72], an in-house developed software, to optimize the plan.

The planning was done on the average intensity CT of the patient, which is the average of the phases of the 4D-CT. The target specified was the envelope of motion of the tumor, so that the target remains within the field in every breathing phase. The voxel values in this so called IGTV (Internal Gross Tumor Volume), were replaced by a value representing tumor density (HU=50) to guarantee coverage in every breathing phase. This method has been shown to provide a good trade-off between target coverage and irradiation of normal tissue for passively scattered proton therapy [65].

We have consistently used two beams for each patient, with beam angles chosen to minimize exposure of the normal lung. The multi-criteria optimization [28] within ASTROID was used to minimize the dose to the normal lung while maintaining target coverage >99% of the prescribed dose.

Both *XiO* and ASTROID use a similar *pencil beam algorithm* to calculate the dose distribution of the proton beams in the patient, as described in the following chapter.

2.3.1 Pencil Beam Algorithm

To calculate the dose in the patient, ASTROID and *XiO* use a pencil beam algorithm based on [57]. The dose to a point from a specific pencil beam is given by a central axis term $C(z')$ and an off-axis term $O(x', y', z')$

$$d(x', y', z') = C(z')O(x', y', z'), \tag{2.19}$$

where the central term is taken from the measured broad-beam depth dose distribution in a water phantom, modified by an inverse-square correction:

$$C(z') = DD(d_{eff}) \left(\frac{ssd_0 + d_{eff}}{z'} \right)^2 . \tag{2.20}$$

ssd_0 denotes the source surface distance for the measurement and d_{eff} the effective depth

$$d_{eff} = R_0 - (R_r - rpl(z')), \tag{2.21}$$

where R_0 is the initial range of the protons and R_r the residual range upon entering the patient. $rpl(z)$ denotes the radiological path length

$$rpl(z) = \int_{surface}^{z} \mathrm{d}z' \mathrm{WED}(\mathrm{CT}(z')), \tag{2.22}$$

where WED is the water-equivalent density of the CT value at the point z'.

The off-axis therm is a Gaussian and represents the lateral flux distribution from the radial emittance suffered by protons along the pencil beam's central axis

$$O(x',y',z') = \frac{1}{2\pi\sigma_{tot}(z')^2}\exp\left(-\frac{x'^2+y'^2}{2\sigma_{tot}(z')^2}\right), \tag{2.23}$$

where $\sigma_{tot}(z')$ is the standard deviation of the radial emittance which will be discussed in detail below.

The dose to a given point in the patient is now determined by integration over all contributing pencil beams

$$D(x,y,z) = \iint \mathrm{d}x'\mathrm{d}y'\Psi_0(x',y')\frac{C(x',y',z')}{2\pi\sigma_{tot}(x',y',z')^2}\exp\left(-\frac{(x'-x)^2+(y'-y)^2}{2\sigma_{tot}(x',y',z')^2}\right), \tag{2.24}$$

where $\Psi_0(x',y')$ is the intensity profile of the open beam.

The total gaussian radial emittance is composed of three components,

i) scattering in devices upstream of the beam-limiting devices (if applicable) is implemented as increasing the effective source size σ_{source}.

ii) scattering in devices downstream of the beam-limiting devices is incorporated as increasing the spatial standard deviation at the depth of the point of interest by an additional emittance σ_{srm}.

iii) multiple scattering within the patient is modeled as scattering in an infinitely thick material, and is only a function of the water-equivalent depth $rpl(z)$:

$$\sigma_{pt} = y_0(rpl(z)). \tag{2.25}$$

y_0 is a Gaussian distribution describing the radial distribution of fluence and can be calculated using the generalized Highland approximation [48] to have a standard deviation at depth t' of

$$y_0(t') = 14.1\left(1+\frac{1}{9}\log_{10}\left(\frac{t'}{L_R}\right)\right)\left[\int_0^{t'}\left(\frac{t'-z}{pv}\right)^2\frac{\rho}{L_R}dz\right]^{1/2}, \tag{2.26}$$

where L_R is the radiation length of the material and pv the product of momentum and velocity of the protons at depth t'. Usually the curves are normalized by the full residual range and pre-tabulated to enable quick look-up by the algorithm. This formula is obtained by fitting Bethe's modification of Moliere's theory, as described in equation 2.8, over a range of target thicknesses and materials. This approximation has been well tested and yields results almost as accurate as Molieres full theory [48].

The contributions from these three components are summed in quadrature to provide the total standard deviation of the radial distribution of the pencil beam profile:

$$\sigma_{tot} = \left[\sigma_{source}^2 \left(\frac{z_p - z_{bld}}{z_{bld}} \right)^2 + \sigma_{rms}^2 + \sigma_{pt}^2 \right]^{1/2}, \tag{2.27}$$

where z_{bld} is the distance from the source to to the downstream face of the beam-limiting device.

In active scanning, where little material is in the beam path, the first two terms are replaced by the intrinsic lateral spread of the scanning nozzle $\sigma_0(R_S, z_p)^2$, which is determined by the properties of the scanning nozzle, magnetic steering and the scatter in air, and which is a function of range and position along the beam axis [72].

2.3.1.1 Computational Implementation

Within ASTROID the physical pencil beams are given by their position at nozzle exit, their spread σ and the total number of protons contained in them. To reach sufficient lateral accuracy these pencils are sub-divided into *bixels* for computational purposes, as schematically presented in figure 2.2.

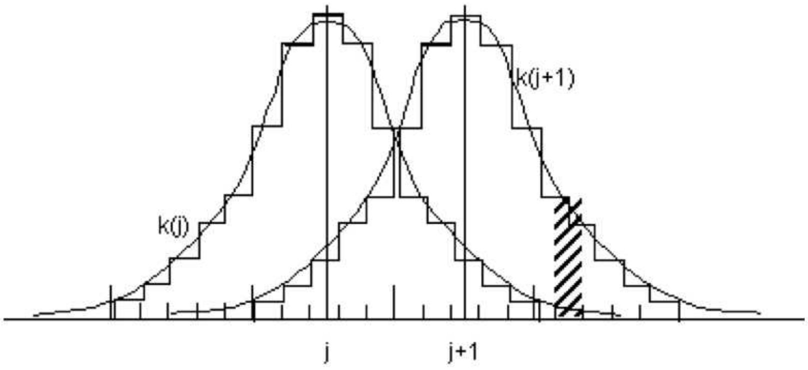

Figure 2.2: Schematic of pencils j subdivided into bixels $k(j)$, which receive contributions from multiple pencils. Image courtesy of Hanne Kooy (Harvard Medical School, MGH).

Summing over all bixels in a surrounding area K the dose from a pencil j to a point i is therefore

$$D_{ij} = \sum_{k \in K} F_j(k) D_{ik}, \tag{2.28}$$

with $F_j(k)$ the fraction of protons to bixel k from pencil j. The dose in the patient can therefore be computed by convolving the bixels with the fluence of the pencil beams. The geometric accuracy of modeling pencil beams through inhomogeneous geometries is greatly affected by the resolution of this computational bixel grid, which is usually kept constant in the algorithm. For all calculations in this work the bixel grid used by the pencil beam algorithm has been 2x2mm.

2.4 Deformable Image Registration

To perform dose calculation in a moving geometry, it is necessary to map the coordinates between different motion states to be able to calculate the dose that has accumulated at a specific point. Figure 2.3 shows two such motion states, exhalation (left) and inhalation (right), for a patient's anatomy. The vectors superimposed on the inhale phase point to their corresponding position on the exhale phase. To find this vectorfield *deformable image registration* with B-splines was used, which is briefly outlined in the chapter below.

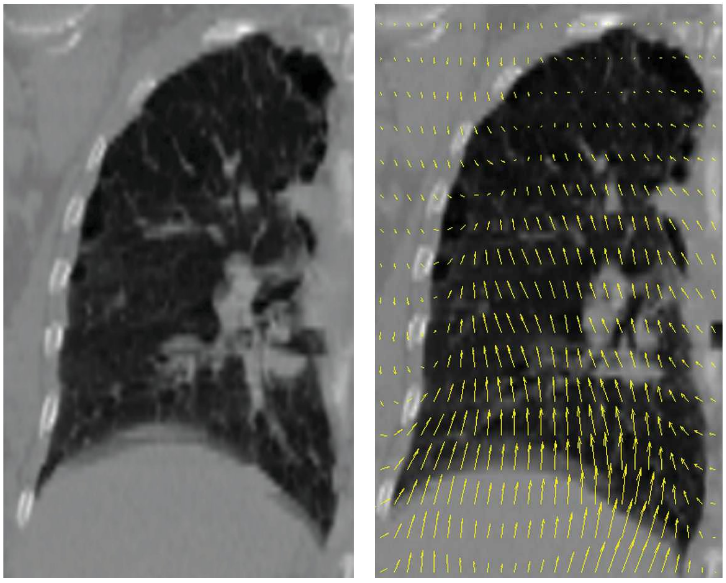

(a) CT in exhale phase

(b) CT in inhale phase with vectorfield to exhale

Figure 2.3: Coronal slice view of a right lung at full exhalation **(a)** and inhalation **(b)** from two phases of 4D CT set. The two volumes were registered by B-spline registration using the mean squared error similarity metric. The full inhalation image **(b)** shows the voxel correspondence to the full exhalation image as a superimposed vector field, which was subsampled and projected into two dimensions for the sake of visualization. Figure courtesy of Tony Shackleford (Drexel University).

Image registration is the process of transforming different sets of images into a common reference coordinate system. *Rigid* registration is limited to global translations and rotations, which is sufficient to detect and correct misalignments in rigid geometries, such as head and neck, but does not model changes due to organ deformation, weight loss or tumor shrinkage [18].

Deformable image registration (DIR) on the other hand includes complex local variations to find the mapping between points in one image and the corresponding points in another. DIR is an ill-posed problem and there is generally no unique solution to a registration problem. In its most general form DIR is formulated as an optimization problem: finding the function g and h for two images $I_1(x, y, z)$ (reference image) and $I_2(x', y', z')$ (moving image), so that

$$I_1(x,y,z) = g(I_2(h(x,y,z))). \tag{2.29}$$

g is an intensity mapping function that describes the differences in image intensities (essential for multi-modal registration, i.e. between different imaging modalities), while h is a spatial 3D transformation so that $h(x,y,z) = (x', y', z')$ [18].

There is a variety of deformable image registration algorithms to solve the above problem, which vary in the choice of similarity measure, transformation model and optimization process [92].

Plastimatch, an open source software for high-performance volumetric registration [124], was used throughout the project for deformable image registration. It is a common method to describe parametric elastic transformations as deformation fields defined by a linear combination of a class of basis functions. *Plastimatch* uses B-splines to define a continuous displacement field ν to map the corresponding voxels in images. The B-splines, short for basis splines, are piecewise cubic polynomials that are combined in a linear fashion to represent the deformation

$$\nu_x = \sum_l p_i \beta_i(x). \tag{2.30}$$

First, the image is partitioned into equally sized tiles. In the 3D case, the vector field ν at any given point is given by the 64 control points surrounding the voxel's tile. So for the x-component of the field at (x,y,z)

$$\nu_x(x,y,z) = \sum_{l=0}^{3} \sum_{m=0}^{3} \sum_{n=0}^{3} \beta_l(u)\beta_m(v)\beta_n(w) P_x(i+l, j+m, k+n) \tag{2.31}$$

represents the B-spline interpolation and P_x is the spline coefficient defining the x-component of ν_x for the control points affecting the voxel. β_l is the uniform cubic B-spline basis function along the x-direction, expressed by the cubic basis splines

$$\begin{array}{lcl} \beta_0(u) & = & \frac{(1-u)^3}{6} \\ \beta_1(u) & = & \frac{(3u^3-6u^2+4)}{6} \\ \beta_2(u) & = & \frac{(-3u^3+3u^2+3u+1)}{6} \\ \beta_3(u) & = & \frac{u^3}{6} \end{array}, \tag{2.32}$$

with anolog expressions for β_m for the y and β_n for the z coordinates.

To measure and optimize the similarity between images, a cost function C is necessary. We use the mean square error (MSE) to compare the deformed moving image $I_2(x+\nu_x, y+\nu_y, z+\nu_z)$ to the reference image I_1

$$C = \frac{1}{N} \sum_x \sum_y \sum_z \left(I_1(x,y,z) - I_2(x+\nu_x, y+\nu_y, z+\nu_z)\right)^2, \tag{2.33}$$

where N is the number of voxels in the image. If the grid of control points is coarser than the underlying image, tri-linear interpolation is used to create the intermediate voxels.

We used a multi-level approach, where optimization was first performed on a coarser control grid and further used as input for a fine registration on the grid of the original image.

A feature of B-splines is the fixed resolution of the control points, meaning that the resolution of the optimization can only be improved globally, leading to large numbers of control points in areas where the underlying image does not provide much structure. Alternatively Bernstein polynomials or Bezier curves could be used as basis functions for the transformation [131].

For minimization of the cost function in 2.33 gradient descent optimization is used. The cost function gradient

$$\frac{\partial C}{\partial P} = \sum_{(x,y,z)} \frac{\partial C}{\partial \nu(x,y,z)} \frac{\partial \nu(x,y,z)}{\partial P}, \tag{2.34}$$

quantifies the variation of C with varying underlying coefficient values P at each control point and the summation includes all neighboring points affecting it. The first term is only a function of the exact parametrization and cost function employed and can be expressed as

$$\frac{\partial C}{\partial \nu(x,y,z)} = 2 \cdot (I_1(x,y,z) - I_2(x+\nu_x, y+\nu_y, z+\nu_z)) \nabla I_2(x,y,z), \tag{2.35}$$

using the deformed images gradient $\nabla I_2(x,y,z)$.

The second term, $\frac{\partial \nu(x,y,z)}{\partial P}$, describes how the vector field changes with the coefficients at the control-points and can be written as

$$\frac{\partial \nu(x,y,z)}{\partial P} = \sum_{l=0}^{3} \sum_{m=0}^{3} \sum_{n=0}^{3} \beta_l(u)\beta_m(v)\beta_n(w) \tag{2.36}$$

according to 2.31, which is only dependent on the location of the voxel and the exact parametrization 2.32.

So during the iterative optimization process this term does not have to be recomputed at each step and can be stored in a look-up table. 2.35 on the other hand depends on the current values of the deformation field ν and changes with each iteration in the optimization process.

To find the coefficient P that minimizes the MSE (2.33), a quasi-Newtonian optimizer (L-BFGS-B) is used. The optimization algorithm is a limited-memory version of the *Broyder-Fletcher-Goldfarb-Shanno* algorithm, which stores only a few vectors to represent an approximation to the inverse Hessian matrix implicitly. This results in linear memory requirements, which is important as the number of coefficients to be optimized in deformable image registration can become quite large [19, 151].

2.5 Evaluating Inhomogeneous Dose Distributions

The aim of the treatment planning process described earlier is generally to deliver a homogeneous dose to the target [55]. As described earlier (chapter 1.3), the interplay effect leads to an inhomogeneous dose distribution that we model correctly using the Monte Carlo code (chapter 2.2.2) and deformable image registration (chapter 2.4). This chapter describes how best to evaluate these inhomogeneous dose distributions, in terms of pure physical dose as well as outcome of the treatment.

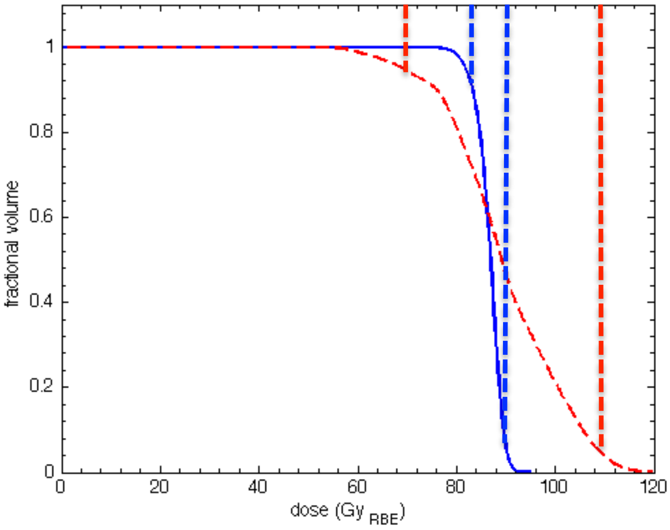

Figure 2.4: Dose Volume Histogram of 2 dose distributions with same mean dose to the structure, yet different degrees of homogeneity within the volume of interest. The dotted lines signify the D_{95} and D_5 of each distribution, i.e. the minimum dose to that is given to 95% or 5% of the volume. The spread between the values can be taken as a measure of dose homogeneity (D_{5-95}).

Figure 2.4 shows 2 cumulative Dose Volume Histograms (DVH), which plot the fractional volume on the y-axis versus the dose received by that volume. The 2 DVHs belong to different dose distributions with the same mean dose, yet different degrees of homogeneity. To quantify the difference in homogeneity within that volume one can define D_{5-95} as the difference in dose received by the highest 5% of the volume minus the dose received by 95% of the volume, which can be expressed in *Gy* or as percentage of the prescribed dose. The dashed blue and red lines demonstrate the difference in D_{5-95} for these two dose distributions.

Alternatively, the concept of *Equivalent Uniform Dose (EUD)* has been developed:

> "For any dose distribution, the corresponding Equivalent Uniform Dose is the dose (in Gy), which, when distributed uniformly across the target volume, causes the survival of the same number of clonogens." [94]

This concept has been further expanded [144] to the generalized EUD for both tumors and normal tissues:

$$EUD = \left[\frac{1}{N} \sum_i D_i^a \right]^{1/a} , \quad EUD \rightarrow \begin{array}{ll} D_{min} & a \rightarrow -\infty \\ D_{mean} & a = 1 \\ D_{max} & a \rightarrow \infty \end{array} . \tag{2.37}$$

D_i is here the dose in the i-th voxel and a is a parameter which is negative for tumors and positive for normal tissues, and can be fitted to experimentally observed responses. Generally, the EUD will be between minimum (for $a \rightarrow -\infty$) and mean dose for tumors and between mean and maximum dose (for $a \rightarrow \infty$) for normal tissues. This allows to account for different functional organizations in structures at risk, such as the liver (parallel organization, $a \approx 1$) and the spinal cord (serial organization, $a \gg 1$). To analyze the dose to the target we generally used a value of $a = -20$, though we analyzed the sensitivity of our results and our conclusions were independent of the exact value chosen.

To translate the results into clinical outcome, we used a model for *tumor control probability (TCP)*, based on a Poisson statistical model of cellular damage described by a logistic function [84, 118]. The probability to control the tumor is accordingly

$$TCP = \frac{1}{1 + \left(\frac{D_{50}}{BED_2} \right)^{4\gamma_{50}}}, \tag{2.38}$$

where D_{50} is the dose for a 50% tumor control rate and γ_{50} the normalized slope of the sigmoid-shaped dose-response curve. BED_2 is the total dose corrected for conventional $2Gy_{RBE}$ fractionation, as we planned treatments with $2.5Gy_{RBE}$ in each fraction, which can be converted following the linear-quadratic model [98] using

$$BED_2 = D_0 \left(\frac{1 + \frac{d_0}{\alpha/\beta}}{1 + \frac{2}{\alpha/\beta}} \right), \tag{2.39}$$

where a α/β-ratio of 10 was used to describe tumor tissue.

CHAPTER 3

Dose Calculation Accuracy for Proton Therapy in Lung

Contents

3.1 Study Details 30
3.1.1 Phantom Study 30
3.1.2 Patient Cohort 31
3.2 Dose to Target 33
3.3 Beam Range in Patients 34
3.4 Discussion 35
3.4.1 Impact of MC Dose Calculation on Dose to Target and Critical Structures 36
3.4.2 Impact of MC Dose Calculation on Range Uncertainty and Associated Margins 37
3.4.3 Clinical Impact 38
3.5 Conclusion 38

This chapter[1] investigates the accuracy of Proton dose calculation in the treatment of lung tumors. As mentioned in the introduction, proton therapy has only relatively recently started to be investigated for the treatment of lung cancer and the results of the on-going clinical trials will determine the future role of proton therapy in the treatment of lung cancer.

For photon dose calculations, it has long been known that equivalent-path-length (EPL) algorithms severely overestimate the dose to the target [26, 67]. This has been the motivation for the development of alternative methods, such as convolution/superposition and Monte Carlo (MC) algorithms and their introduction into the clinic over the last decade [26]. The adequacy of current clinical dose calculation algorithms for protons in this challenging geometry needs to be ensured. This deserves special attention, since the finite range of protons and the lower number of incident beam angles in proton compared to photon therapy leave less margin for error.

The aims of study described here are to:

---

[1] Results from this chapter have been presented as oral presentation entitled *"Experimental Validation of Clinical as well as Monte Carlo Dose Calculation for Proton Therapy of Lung Cancer Patients"* at the 2013 Annual Meeting of the American Association of Physicists in Medicine (Indianapolis, USA) and have been submitted for publication.

1. Assess a clinical treatment planning system and a MC dose calculation algorithm through measurements in a lung phantom, focusing on:

  1A. the dose to the target

  1B. range uncertainties at the distal fall-off

2. Analyze the difference between the treatment planning system (TPS) and Monte Carlo in a cohort of 19 patients treated with passively scattered proton therapy.

3.1 Study Details

3.1.1 Phantom Study

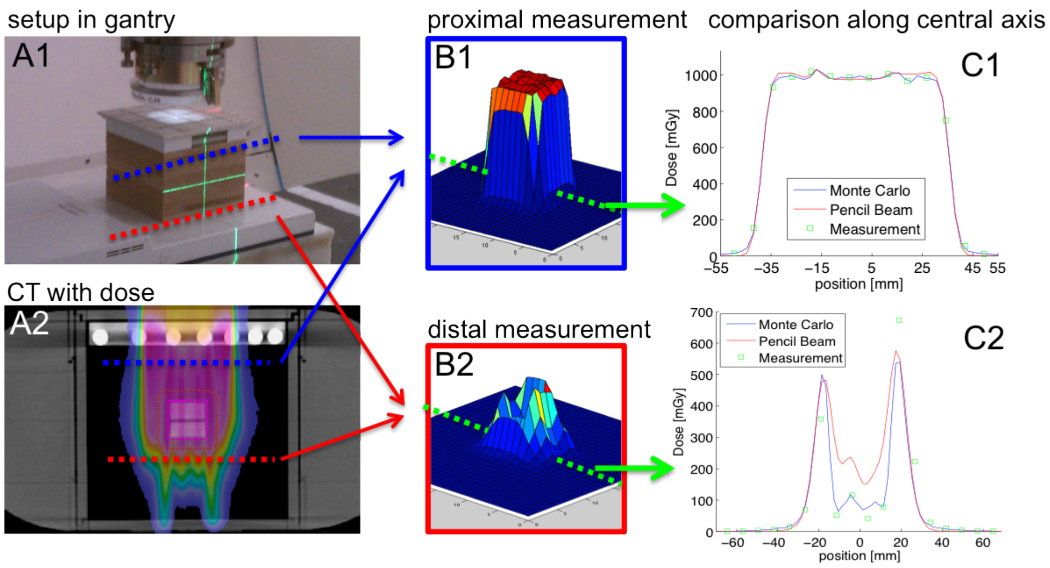

Figure 3.1: Explanation of experimental setup and measurements for various depths. (A1) middle part of lung phantom on ionization chamber array. (A2) CT of the phantom with planned dose distribution. (B1-2) Measurement results in planes proximal and distal to the target. (C1-2) Line profiles through the central axis of (B1-2), shown together with the predictions of Monte Carlo and the Pencil Beam Algorithm.

Experiments were conducted at Massachusetts General Hospital. The Wellhofer I'mRT phantom consisted of 10mm slabs of cedar wood with a stopping power (SP) of 0.33, according to the HU-SP conversion curve used by the TPS. The tumor (20x20x20mm3, SP=1.15) is divided in two halves and embedded in two thicker slabs (20mm), to enable measurements in a plane within the target. Figures 3.1A1 and 3.2A show the experimental setup, the structure placed on top of the ionization chamber array (I'mRT MatriXX, Ion Beam Applications) is the middle part of the phantom, a CT scan of which is shown in figure 3.2B. For all experiments we used the beam's-eye-view x-ray system, reducing the setup uncertainty to $<$1mm.

The uncertainty in dose measurement was assumed to be 1.5% according to vendor specifications, and the statistical uncertainty of the MC simulations was

<1%, due to the high number of protons (10^8) simulated per field.

We used the TPS to plan a treatment with a prescribed dose of 1Gy(RBE) to the clinical target volume (CTV), defined as 8mm expansion of the gross tumor volume (GTV). Subsequently, we delivered the treatment to the experimental setup (figure 3.2A) and measured the dose distribution across a plane in the middle of the target.

For the range measurements, we modified the homogeneous phantom by including an artificial chest wall (figures 3.1A2 and 3.2C), consisting of Lucite (20mm thickness) embedded with bone equivalent 'ribs' (11mm diameter). Following clinical protocols, we developed a single-field treatment plan to cover the target. 64 ionization chambers of the detector-array were located within the field. By gradually adding lung slabs (water-equivalent thickness=3mm) to the setup, we were able to measure the dose at each of these 64 points with increasing depth, allowing us to calculate the range in the phantom. This is exemplified in figure 3.1, which shows measurements (B1-B2) at differents planes in the phantom (A2), and line profiles comparing Monte Carlo to the Pencil Beam Algorithm and measurements.

We chose Range50, i.e. the range where the dose has fallen to 50% of the prescribed dose, to compare the measured and predicted ranges.

3.1.2 Patient Cohort

All patients undergoing proton therapy to treat tumors in the lung at our institution dating from July 2011 to July 2013 (n=18) were included in the study. Additionally, one patient that was planned with protons but randomized to the photon arm of an ongoing clinical trial was also included.

As this study focused on the accuracy of clinical dose calculations in the lung, the specific tumor histology did not impact the study design. Prescribed doses and fractionation schemes varied, the patient cohort included 6 stereotactic cases, 2 boost-plans complementing photon plans, and 11 fractionated schedules. To account for these variations, all deviations are given in percentages of the prescribed dose. Tumor sizes ranged from 2-318cc, with clinical stages from IA-IV.

To compare to a site with less complex patient geometry, an additional set of 10 liver fields, with similar water-equivalent ranges (108-194mm) and field sizes to the lung cohort was included.

All patients were planned and treated using passively scattered proton therapy. The treatment planning system employed was *XiO* (Computerized Medical System) with an analytical algorithm as described in chapter 2.3.1. The patients were planned according to clinical protocols, either developed at our institution [37] or methods used in multi-institutional trials [65]. For recalculation, the plans were exported from the TPS to the MC system TOPAS, as previously mentioned in chapter 2.3.

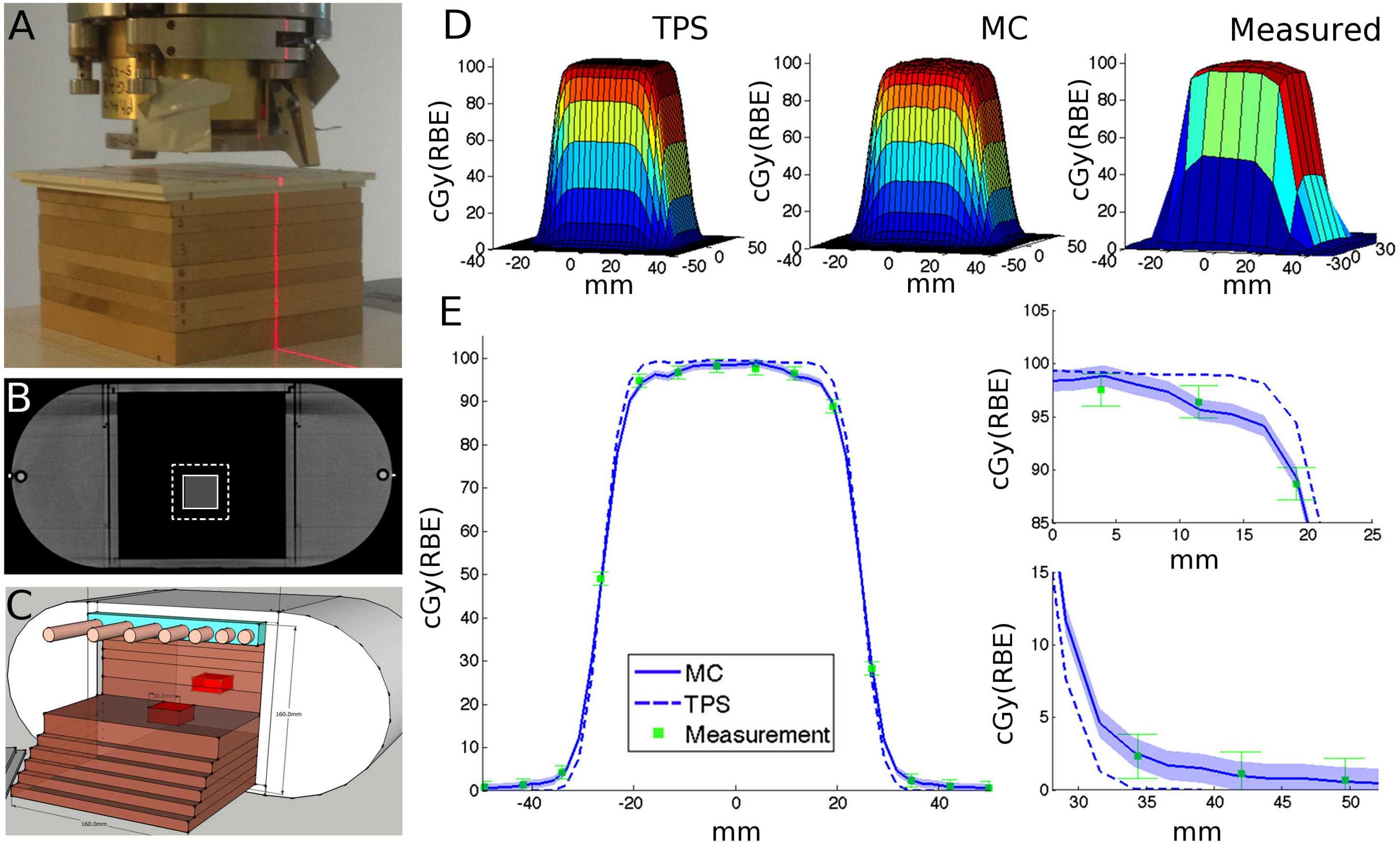

Figure 3.2: Experimental setup and results (A) Lung slabs (cedar wood) and chest wall (lucite) positioned on the 2D-array of ionization chambers. (B) CT of the phantom with GTV (full) and CTV (dashed) contours. (C) Modified phantom with chest wall, showing also the 2 halves of the embedded tumor. (D) Measurement results in central plane of target (right) together with prediction of TPS (left) and Monte Carlo (middle). (E) Line profile through the central axis of the tumor, with magnifications for target periphery (top right) and penumbra (lower right). Error bars for measurement 1.5%, for MC 1% (shaded blue).

3.2 Dose to Target

Figures 3.2D-E show the experimental results, obtained with the setup in figures 3.2A-B, together with the predictions of the TPS and MC along a profile through the center of the target. The measurements in the periphery of the high dose region (figure 3.2E, top right) are consistently lower than planned by the TPS, within measurement uncertainty of the MC prediction. In the low-dose penumbra (figure 3.2E, lower right) measurements and MC coincide as well, showing a higher dose than predicted by the TPS. Across the measurement plane within the target, the average difference between measurement and MC is 1.6% of prescribed dose, compared to 5.6% for the TPS.

The reason for the lower dose in the periphery, and conversely higher dose in the penumbra, is that protons interacting in the chest wall are scattered further out of field due to the low-density lung tissue that follows. The mechanism will be further discussed below.

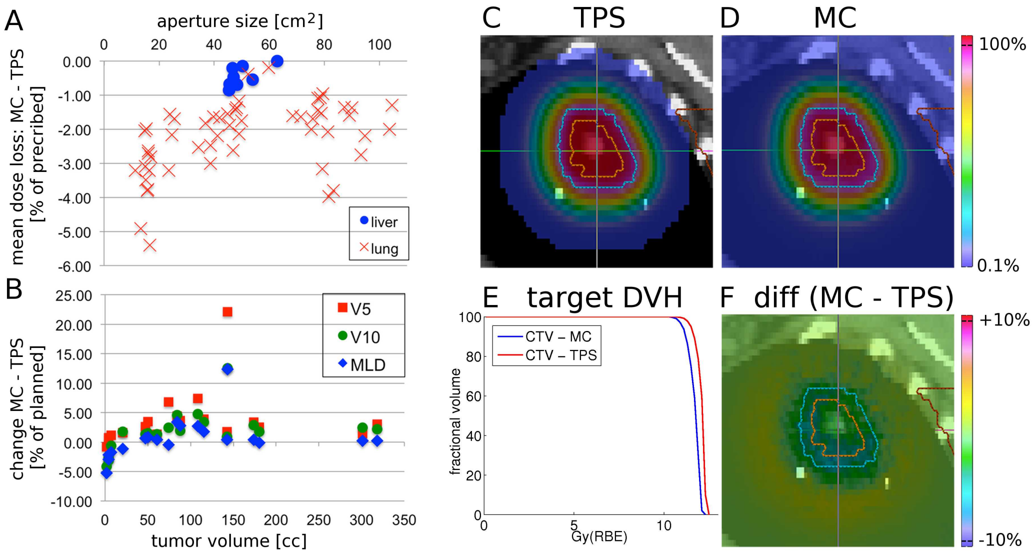

Figure 3.3: Summary of the patient study. (A) Mean target dose difference (MC-TPS) in % of prescribed dose plotted against the size of the aperture opening. (B) Changes in MLD, V5 and V10 in percent of planned values as a function of tumor volume. (C-F) Example field: TPS dose (C), MC dose (D), DVHs (E) and dose difference (F=C-D). All color bars are percentages of prescribed dose, transparent <0.1%. Orange/blue contours represent the GTV/CTV.

A similar effect is observed in MC recalculations of patient treatment plans, shown in figure 3.3A. The mean dose difference predicted by MC and TPS is plotted as a function of size of the aperture opening. The crosses represent the 54 fields from the 19 treatment plans and the circles correspond to the 10 liver fields. The MC algorithm consistently predicts a lower target dose, and the effect is higher in the lung compared to liver. The average(maximum) mean dose loss in is -2.3%(-5.4%) for all 54 fields. The minimum target dose for a specific field decreases by up to -7.6%. The average(maximum) mean dose loss per patient is -2.2%(-4.1%), as the effect averages out over multiple fields.

Figure 3.3B demonstrates the effect of the calculation algorithm on the dose to normal lung, showing that MC predicts a lower dose to normal lung for small targets and a higher dose for large ones. The difference (MC-TPS) in mean lung dose (MLD) and the volumes receiving greater than 5Gy(RBE) (V5) and 10Gy(RBE) (V10) were between -5-+12%, -1-+22% and -4-+13% respectively.

Figures 3.3C-F show the results for one field of a lung patient, i.e. a single data point in figure 3.3A. The TPS and MC predictions and their DVHs are shown in figures 3.3C, 3.3D and 3.3E respectively. The dose difference in figure 3.3F highlights the lower target dose predicted by MC. Note the increasingly lower dose towards the CTV edges in figure 3.3F, which resembles the experimental results shown in figure 3.2E.

3.3 Beam Range in Patients

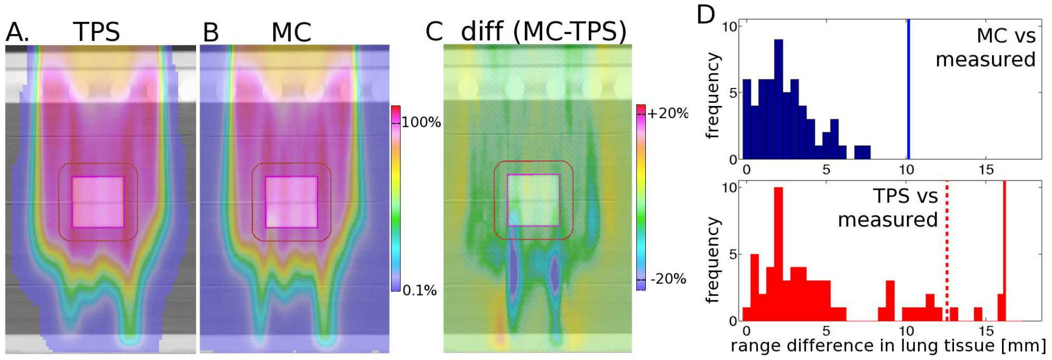

Figure 3.4: Experimental verification of proton range using a heterogeneous lung phantom (shown in Fig 3.2C): prediction of TPS (A), MC (B), difference MC-TPS (C). Red areas in (C) indicate higher dose predicted by MC. All color bars are percentages of prescribed dose, transparent <0.1%. (D) Histograms representing the difference in measured Range50 compared to MC (top, blue) and the TPS (bottom, red). The vertical lines represent range margins discussed in [99]: 2.4%+1.2mm (solid blue), 4.6%+1.2mm (solid red), 3.5%+1mm (dashed red).

Figures 3.4A and 3.4B show the predictions of the TPS and the MC algorithms in the modified lung phantom which included an artificial chest wall. The difference between the two (MC-TPS) is shown in figure 3.4C, with red and blue areas indicating higher doses in MC and TPS, respectively. The histograms in figure 3.4D demonstrate the results, displaying the differences in Range50. Each entry represents the difference between predicted and measured range in one of the 64 measurement points on the distal surface. The average(maximum) range differences were 3.9mm(7.5mm) and 7mm(17mm) for MC and TPS respectively. Note that the range differences in figure 3.4D are given in lung tissue, i.e. are magnified by a factor 3 compared to soft tissue.

These differences are caused by inaccuracies in the modeling of multiple Coulomb scattering in the TPS algorithm, which only accounts for the material along each pencil's central axis [57, 108, 135, 137].

In the Monte Carlo algorithm on the other hand, the protons and all secondary particles produced are transported step-wise through the voxelized geometry. This then determines the angular and spatial distribution produced by the scattering with nuclei, as described in chapter 2.1.2. So the protons can take various paths through the patient, even for the same initial conditions. In the pencil beam calculation on the other hand this is estimated through the path of the central axis of the pencil, even for protons deflected away from the central axis.

The second approximation by the pencil beam algorithm is the assumption that the patient is water-like, so the all parameters (including lateral scattering) are dependent on this water-equivalent depth. Monte Carlo on the other hand takes the material composition of the material into account for scattering, so considers the different scattering in bone compared to water.

These effects are prominent when heterogeneities are along the beam path, which is the case for most lung patients due to rib-lung interfaces. Figure 3.5 shows the dose distribution calculated by the TPS, MC, their difference (MC-TPS) and the DVHs of target and the spinal cord (from left to right). This patient was ultimately treated with photons, however the data shows the impact range uncertainties can have. The increased range in the superior part of the field leads to a marked increase in dose to the spinal cord, which clearly alters the DVH.

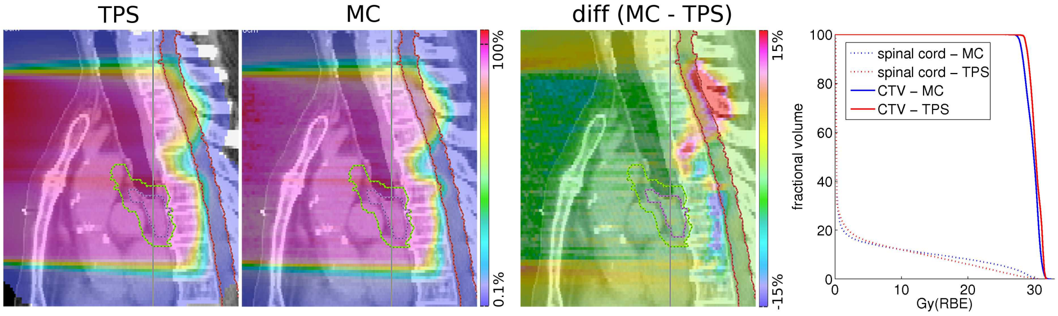

Figure 3.5: Example of underestimated range in a patient by an analytical dose calculation algorithm. Dose calculation by TPS (A), MC (B) and difference MC-TPS (C). Red areas in (C) indicate higher dose predicted by MC. (D) shows the dose-volume-histograms of spinal cord and CTV for the MC and TPS dose distributions. All color bars are in percent of prescribed dose. Contours shown are the GTV (pink), CTV (green) and spinal cord (red).

3.4 Discussion

The experiments confirm that the dose to peripheral regions of a target embedded in low-density tissue is lower than expected by the TPS and can be correctly predicted by MC simulations. The reason lies in the degradation of the lateral penumbra, which increases as a function of depth more pronounced compared to the prediction by the TPS. Analytical algorithms [57,108,135,137] assume that the penumbra width is a function of water-equivalent depth only. Yet after scattering in the chest wall, the beam diverges over a longer distance, because of the higher geometric range of the beam in low-density tissue. The implication for the target dose is visualized in figure 3.6, which shows the dose profile as predicted by TPS and MC for the patient shown in figures 3.3C-D, replicating the phantom results presented in figures 3.2D-E.

This effect is related to the well-known field-size-effect [30], which is exacerbated in low-density lung tissue. This is demonstrated by the liver fields also shown in figure 3.3A, which exhibit a similar size and range compared to the lung fields, yet do not show degradation in mean dose greater than 1%. This discrepancy of MC and analytical algorithms in lung compared to liver targets has already been noted in a recent simulation study [145].

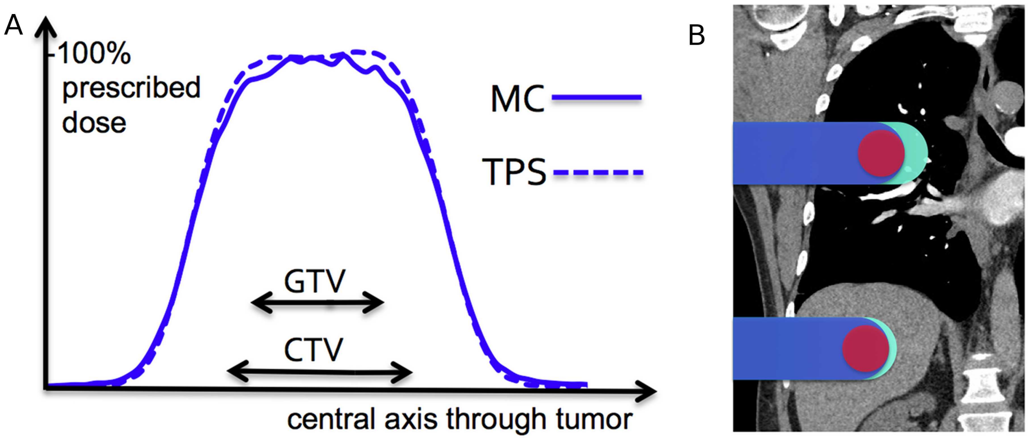

Figure 3.6: Left: Dose profile of TPS and MC along the horizontal axis of the dose distribution in figures 2C-D Right: Visualization of the impact of tissue density on the range margin (cyan area). Both fields have the same (water-equivalent) range and therefore range margin, indicated in cyan, yet the margin of the superior field is enlarged by a factor ≈3.

3.4.1 Impact of MC Dose Calculation on Dose to Target and Critical Structures

The dose reduction measured in the phantom, see figure 3.2E, is similar to the in-patient effect predicted by MC (figures 3.3C-F). The MC dose is slightly reduced compared to the TPS in the center, while towards the edge of the target the reduction becomes substantial (>5%).

As visible in figure 3.3A, there is a significant correlation between the loss of mean target dose and the aperture size (Spearman's p=0.0002). The spread among the values in figure 3.3A for the same aperture size suggests additional confounding factors to the field-size [30], visualized in figure 3.7. In addition to the aperture size, the tumor-chest wall distance (figure 3.7, left) also significantly correlates (Spearman's p=0.004) with lower dose. The range of the field (figure 3.7, right) also has a significant correlation (Spearman's p=0.0001) to lower dose, though only for fields of similar size (>20cm^2). Therefore fields with a large tumor-chest wall distance and a high range are most at risk of delivering lower target doses than predicted by the TPS.

As shown in the results, analytical dose calculation methods in the lung can lead to a mean dose loss in excess of 5% for small targets, while the lung V5 can increase by >20%. Not accounting for these deviations could inherently introduce bias into randomized clinical trials comparing photon and proton therapies for lung cancer.

First, due to the steep dose-response curve of most lung cancer cell lines [31], a lower mean target dose can have a significant effect on outcome, as shown in previous clinical studies [121]. As figure 3.6 demonstrates, the TPS underestimates the dose specifically in the CTV periphery, a region that has been linked to increased cancer stem cell density [130]. Consequently, the effect on local control could be higher than the mean dose loss initially suggests. It has also been shown in clinical studies that prescription of dose to isocenter, leading to lower peripheral tumor doses, is linked to decreased local control [121].

Secondly, as the MC algorithm predicts consistently higher doses to the normal lung for large targets, conclusions regarding the toxicity of protons could be adversely affected. This would especially concern trials designed around iso-toxic dose escalation strategies [140].

3.4.2 Impact of MC Dose Calculation on Range Uncertainty and Associated Margins

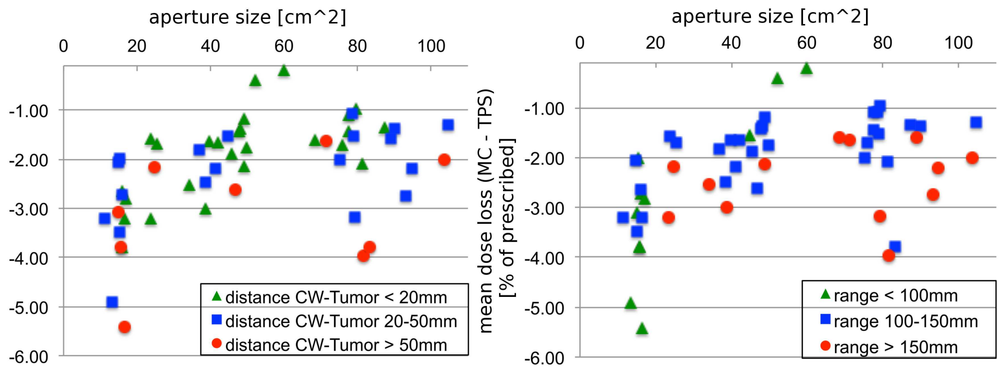

Figure 3.7: Factors leading to lower mean dose to the target. Left: distance chest wall-tumor. Right: range of proton field in water. CW=chest wall.

The second area in which MC algorithms can impact clinical practice is through reduced range uncertainty margins. The impact will be greatest for large targets located in the lung, because the range margin is defined as an increase in the water-equivalent range. If the distal fall-off occurs in low-density tissue, as is shown in the right of figure 3.6, the volume of normal tissue irradiated is increased compared to other soft-tissue sites.

It has been proposed that by employing MC algorithms for treatment planning, range margins associated with dose calculation uncertainty could be reduced from 4.6%+1.2mm to 2.4%+1.2mm [99], represented by the solid lines in figure 3.4D. The results of this work indicate that the latter is an adequate margin for dose calculation uncertainty, though additional margins certainly have to be added to account for other uncertainties encountered in patient treatments. The lower histogram in figure 3.4D suggests that 4.6%+1.2mm is a necessary margin for the current TPS. Furthermore, applying a margin of 3.5%+1mm, a commonly used value for proton range uncertainty , is not sufficient in this inhomogeneous geometry. Acknowledging this, we currently use additional range margins at our institution for lung treatments.

The reduction in range uncertainty margins by 2.2%, i.e. from 4.6% to 2.4%, can make a sizable difference if in lung tissue. For example, at 20cm range, MC algorithms could decrease the distal range margin by 4.4mm water-equivalent range, which corresponds to approximately 15mm of lung tissue.

3.4.3 Clinical Impact

A short-term solution could be to triage patients to specific risk groups based on figure 3.7 and apply a parameterized increase in delivered monitor units or to perform retrospective MC dose calculation, particularly for patients with small tumors far from the chest wall. The treatment plan could then be amended as required to counter the lower dose. Various scenarios can be envisioned as medium- to long-term solutions. Current shortcomings of analytical algorithms could be addressed in more advanced versions, such as pencil-beam redefinition algorithms [35], to improve the dose calculation accuracy in the presence of lateral heterogeneities.

As the effects described in this publication are not the only weakness of current analytical algorithms [77, 114], the authors advocate the incorporation of MC algorithms into treatment planning. Monte Carlo algorithms have been the gold-standard for proton therapy dose calculation for decades [20], and the latest developments have shown promising results in terms of speed [62, 63].

Though we studied the problem only for passively scattered proton therapy, the observed effect is a consequence of the shortcomings of current analytical algorithms, variants of which are employed by most clinical TPS. Therefore similar effects will likely be observed for active scanning proton therapy, which relies on these algorithms as well.

3.5 Conclusion

It has been demonstrated experimentally that current analytical dose calculation algorithms for protons used in the clinic can overestimate the mean dose to tumors situated in lung by over 5%, and underestimate the dose to the normal lung, especially V5 and V10. Monte Carlo dose calculation techniques have the potential to reduce range margins and increase the accuracy of the relationships between dose and effect, concerning tumor control as well as normal tissue toxicity. This is of ever-increasing importance, as the role of proton therapy in the treatment of lung cancer continues to be evaluated in clinical trials.

Chapter 4

Active Scanning Monte Carlo Simulations

Contents

4.1 Validity of Phase Space based MC Simulations 40
4.2 Calibration in Water Phantom 42
  4.2.1 Derivation of Input Parameters 42
  4.2.2 Comparison to Depth-Dose Measurements 43
4.3 Translation TPS to Phase Space 45
  4.3.1 Patient Simulations 46
4.4 Discussion 49
4.5 Conclusion 50

The last chapter has shown the impact that Monte Carlo simulations can have on the dose accuracy of passively scattered Proton Therapy (PSPT). This chapter will now describe the process of adapting the Monte Carlo code to simulate active scanning beam delivery systems.

As already mentioned in the introduction, Intensity Modulated Proton Therapy (IMPT) is becoming more available as more proton facilities become equipped with beam scanning technology. In IMPT steep dose-gradients can occur within the target, which makes the treatment more sensitive to uncertainties in the exact position of the individual Bragg peaks. Lomax [79, 81] studied how changes in CT values, inter-fraction and inter-field motion affect IMPT plans, concluding that especially plans with steep intra-field gradients are highly sensitive to such errors. Albertini *et. al* [4] examined in detail the usefulness of margins in accounting for setup and range uncertainties in IMPT. They concluded that while safety margins are adequate to increase the robustness of plans with uniform fields and those with low in-field gradients, highly modulated IMPT plans show degradations of dose conformity also in the middle of the target volume.

Improving the ability to accurately predict the range of protons in the patient has other benefits as well. In current clinical practice, beam directions that place the sharp distal fall-off adjacent to a critical structure are generally avoided due to the range uncertainties, even though the anatomical locations of organs at risk (OAR) around the target might favor such arrangements. For scanning systems with relatively large spot sizes (e.g. with sigma values above 10 mm) a situation can occur in which the distal fall-off of the beam is significantly sharper than the lateral one. In this case, using the distal edge would lead to steeper dose-gradients towards critical structures located close to the target. In order to take full advantage of the increased conformity that protons offer, it is therefore paramount to predict the range of proton beams in the patient as accurately as possible.

While the Monte Carlo code for passive scattering used in the last chapter is well tested and commissioned, the active scanning version developed has to be validated with experimental results to assure correct simulations.

This chapter will present the development and commissioning of phase space based Monte Carlo simulations that interface the treatment planning system (ASTROID, see 2.3), with the Monte Carlo code (TOPAS, see 2.2.2).

The aim of this chapter is to

i. perform simulations of the complete MGH Scanning Nozzle to assess secondary particle production and the feasibility of phase space based patient calculations.

ii. outline a generic method to calibrate a Monte Carlo code to measured depth-dose data and apply it to two different institutions using pencil-beam scanning.

iii. translate treatment plans to proton phase spaces treatment head exit and perform absolute dose Monte Carlo simulations in patients of varying complexity (liver, head and neck, lung).

4.1 Validity of Phase Space based MC Simulations

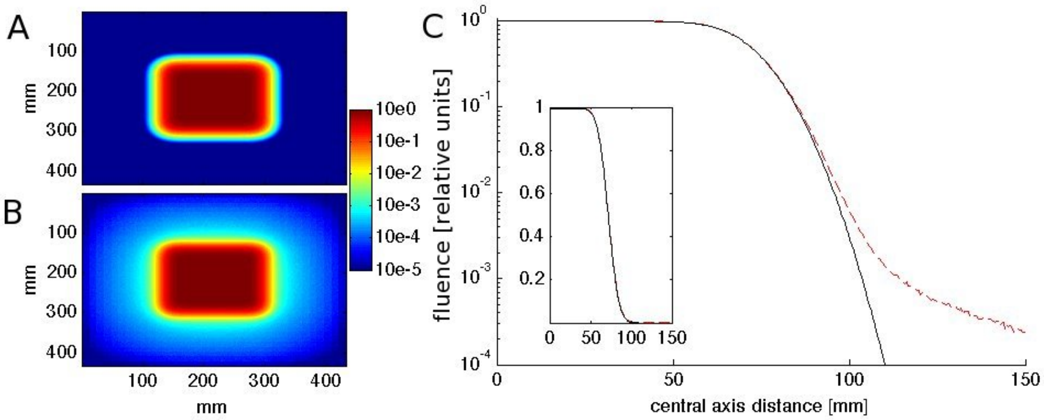

Figure 4.1: Full nozzle versus phase-space based simulations for a 12x12cm field of 91.015 MeV protons. Fluence in air at isocenter in relative units for phase-space based (A) and full nozzle (B) simulations. (C) profile through the central axis, full black line indicating phase-space based results from (A), red dotted line full nozzle results from (B). The scale is in log relative fluence, inset in linear scale.

Active Scanning Proton Therapy offers the possibility to perform Monte Carlo simulations starting at nozzle exit, which offers benefits in terms of speed compared to a simulation of the full nozzle geometry. Figure 4.1 shows the results for the fluence of a 12x12cm field in air at isocenter for the phase-space based (A) and full nozzle simulations (B) for the lowest energy (91.015 MeV). The low-fluence background around the main field originates from scattering in the ionization chambers in the full nozzle simulations. The central axis profile in figure 4.1C demonstrates that below ≈1% of the in-field fluence the phase-space method starts to underestimate the fluence. This means that for calculations of dose far out-of-field, e.g. for the estimation of secondary cancer, phase-space based active scanning simulations could severely underestimate the dose and the full nozzle has to be simulated. We have chosen the lowest energy available as the scattering reduces for higher energies, and this represents a good estimation for the upper bound of the effect of scattering throughout the nozzle.

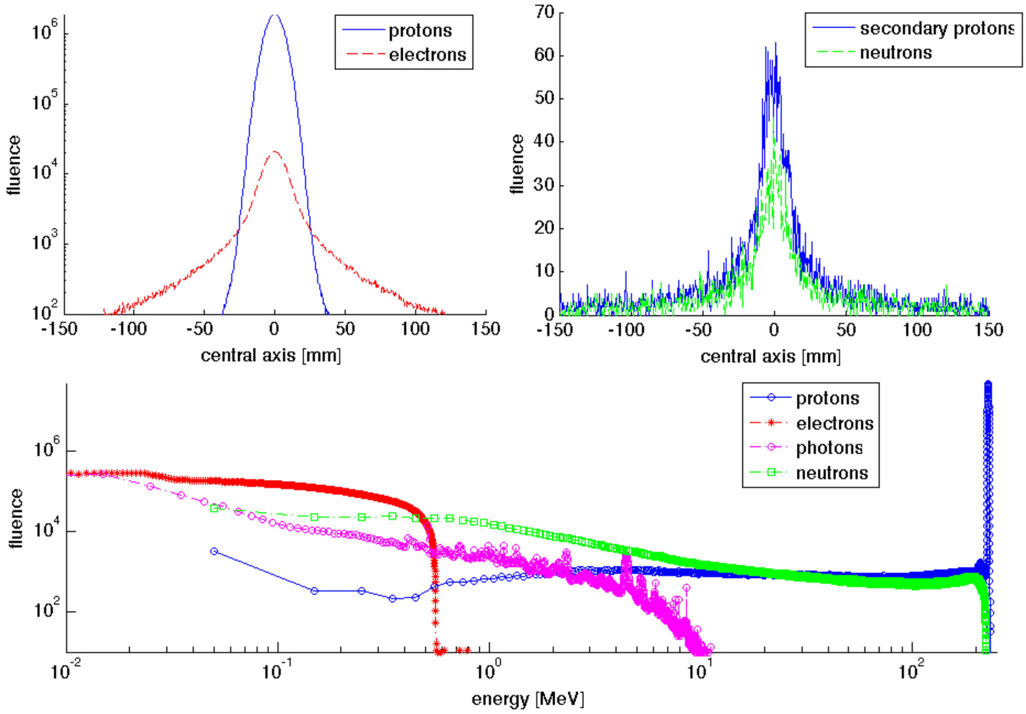

Figure 4.2: **Top**: fluence in air at isocenter for the full nozzle simulations of a 230MeV beam: protons and electrons (top left), secondary protons only and neutrons (top right). **Bottom**: energy spectra for protons, electrons, photons and neutrons at nozzle exit. 10^9 protons were simulated entering the nozzle in these simulations.

Figure 4.2 shows details about the type and angular distributions of secondary particles emitted from the nozzle, together with their energy spectra. Electrons are by far the most numerous secondary particle produced, and are emitted with a relatively narrow angular distribution (see figure 4.2, top left). Due to their low energy, they are nevertheless negligible in terms of dose: even if the would be deposited with a 5mm radius in skin of $70\mu m$ thickness, their contributions would only be $2.37 \cdot 10^{-13}$ Gy per gigaproton (Gp). As an average plan only delivers several hundred Gp, their contribution to skin dose is minimal.

4.2 Calibration in Water Phantom

4.2.1 Derivation of Input Parameters

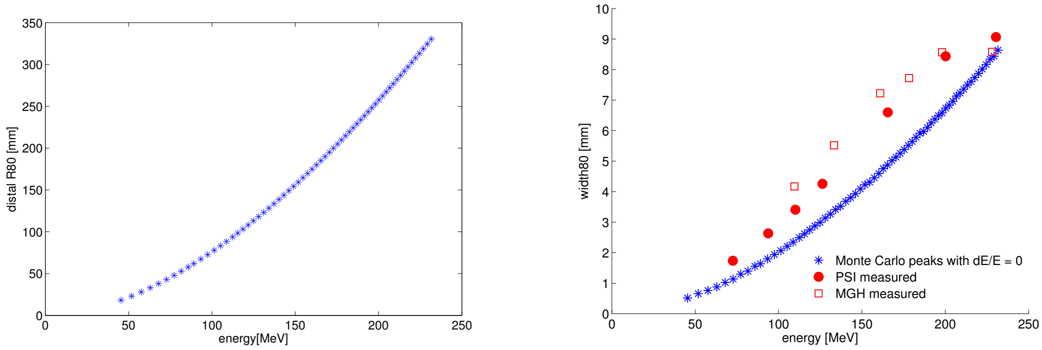

(a) (b)

Figure 4.3: (a) Distal range80 of a set pristine Bragg peaks plotted against energy in a water phantom calculated with TOPAS. (b) width80 in mm of that same dataset, shown together with measurement data of PSI (circles) and MGH (squares).

The first step in the commissioning of a given Monte Carlo code to measured data is to establish its range-energy relationship, since many parameters can affect simulations of the proton range in water. Especially the exact choice in ionization potential for water can change the range of the beam by several millimeters for high energies [11]. This information will be necessary in the next step, when the output of the treatment planning system has to be converted to input suitable for Monte Carlo simulations of patient treatments.

Figure 4.3a shows the depth in which the dose has fallen to 80% of its maximum at the Bragg peak (range80), plotted against the energy. It should be noted that the range-energy relationship on display is not the exact equivalent of the range-energy tables found in ICRU 49 [1] or Janni's report [60], since they use the mean projected range, which is independent of the initial energy spread while the range80 can vary. However, previous work [7, 90] has shown that the deviations are minimal, so the range80 of the beam including initial energy spread will not change significantly compared to the range80 of the mono-energetic beam. Furthermore, range80 has the advantage that it is a characteristic of the depth-dose profile, while accurately determining the mean projected range necessitates fluence measurements [1, 90].

The width80 (the distance of the two points on the depth dose curve that equal 80% of the maximum dose) as a function of energy for the same set of mono-energetic peaks is shown in figure 4.3b. The width80 is sensitive to the initial energy spread of the beam and is readily available through standard commissioning or quality assurance measurements. Also shown in figure 4.3b is the width80 for sets of measured peaks from MGH and PSI. To derive the energy spread to use in our simulations, we can thus employ Bortfeld's analytical model (as described in chapter 2.1.4) to determine the amount of energy spread needed to calibrate the width80 of our mono-energetic beams to match those obtained in measurements.

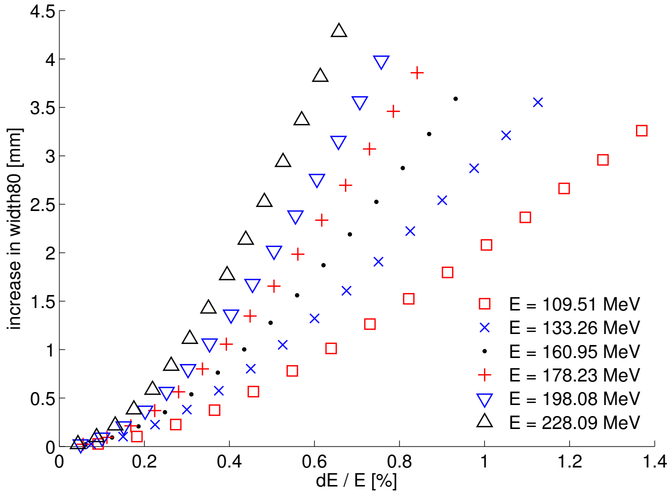

Figure 4.4: Predictions of the analytical model (as discussed in chapter 2.1.4) for the increase in width80 with energy spread (in percent of initial energy) for different energies.

Figure 4.4 shows the result of the analytical model for the energies of the MGH calibration peaks: the increase in width80 is plotted as a function of initial energy spread in %. The peaks with lower energy are generally more sensitive to relatively small variations in absolute increase of width80, as they experience less range straggling along the beam path due to their shorter range. Above a non-linear region for very low energy spreads ($< 0.2\%$) the relationship appears almost linear. Solving for the desired increase in width80 results in the functions displayed in 4.5, which show the initial energy spread as a function of initial proton energy. They reflect the differences in beam transport at the two beam lines: MGH has higher values for low ranges, yet falls below PSI for higher ranges, which is consistent with the measured data for width80 shown in figure 4.3b.

4.2.2 Comparison to Depth-Dose Measurements

To test the accuracy of the polynomial fits shown in figure 4.5, we now simulate the measured peaks with their initial energy E_0 drawn from the function in figure 4.3a and their energy spread σ_E from the fit in figure 4.5. Figure 4.6 shows a comparison of the results of TOPAS simulations with measurements. The upper part shows six peaks from the MGH dataset, highlighting the good agreement in the peak-to-plateau ratios for all ranges. The magnifications of three of the peaks in the lower part also illustrate the match of the exact peak shapes and ranges (within 0.5 mm).

The results for the PSI dataset agree to a similar degree: figure 4.7 shows an

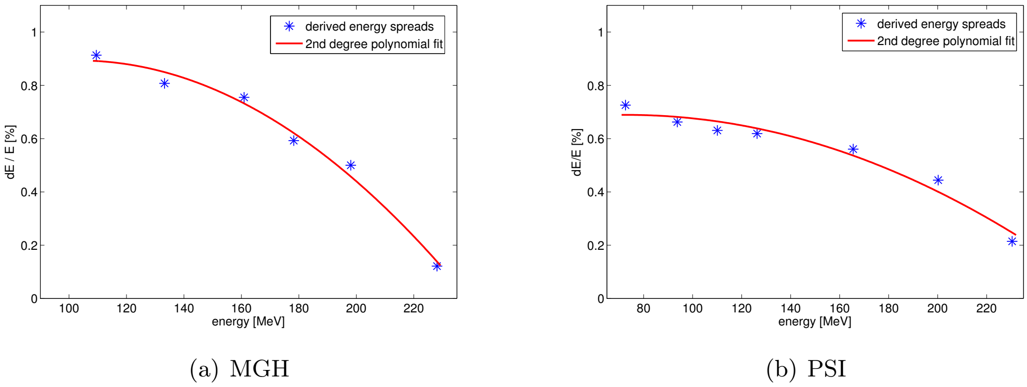

(a) MGH (b) PSI

Figure 4.5: (a) energy spreads according to the fit of the analytical model to the measured width80. Energy spread in percent of initial energy plotted as a function of energy. The red line represents of cubic Derived polynomial fit to the values

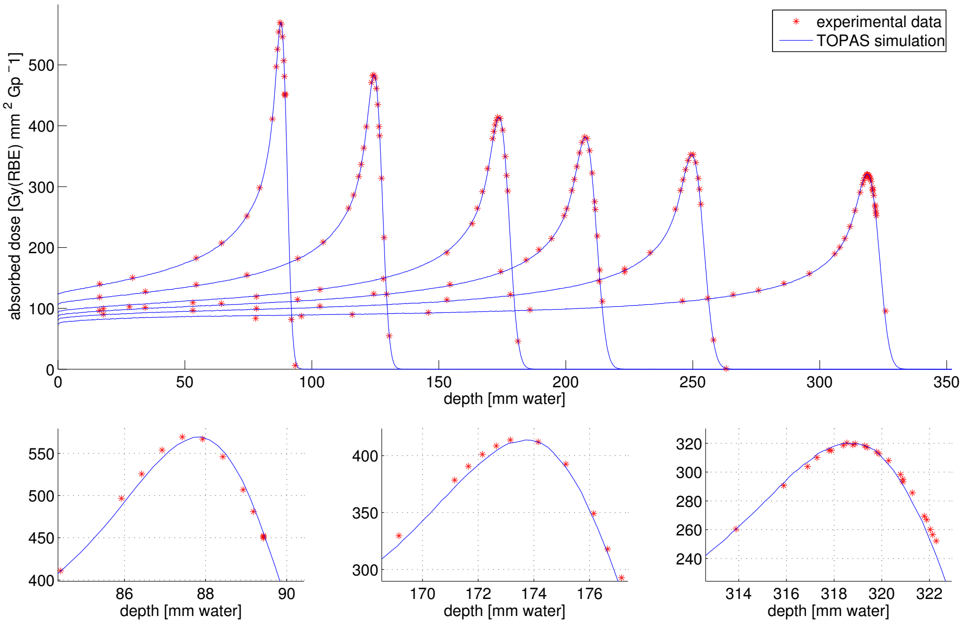

Figure 4.6: TOPAS simulations (blue lines) compared with measurement points (red stars) for the calibration dataset from MGH. The simulations are plotted in units of $Gy(RBE)mm^2Gp^{-1}$, the measurements are normalized to the maximum dose of the simulations. The lower part shows magnifications of the first, third and sixth peak.

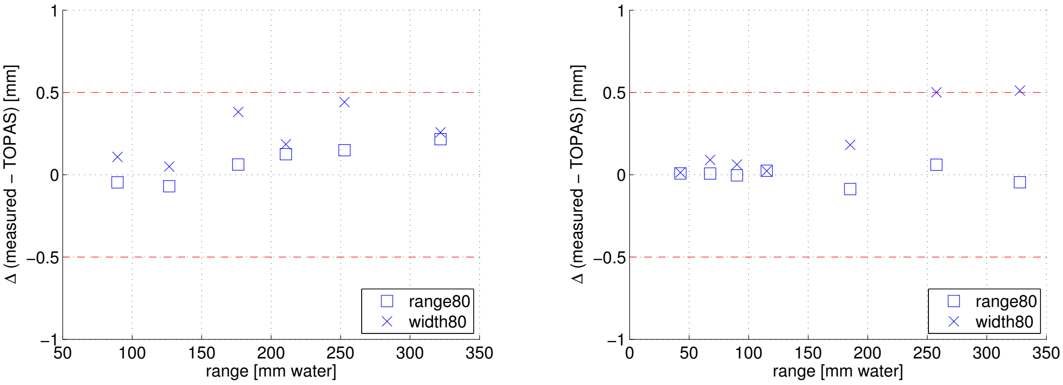

(a) MGH (b) PSI

Figure 4.7: (Differences in range80 (squares) and width80 (crosses) in mm between the TOPAS simulations and the measured depth dose distributions for different ranges.

overview over the differences in width80 and range80 for all ranges for the data from MGH (left) and PSI (right). The agreement for range80 and width80 is within 0.5mm for all ranges considered.

As the exact settings of the physics lists, the step size and even the secondary particle creation threshold can have implications for the exact range of protons and their energy straggling, it is of paramount importance to determine these relationships with the same settings that will be in use later in the patient simulations.

4.3 Translation TPS to Phase Space

To translate the information given by the treatment planning system into input for Monte Carlo patient simulations, corrections must be applied. The energy in the treatment plan is chosen according to energy-range tables within ASTROID, that are based on Janni's tables [60]. These don't represent actual energies measured at nozzle exit, but rather reproducible machine settings that lead to a specific range as measured in a water phantom.

We have to obtain the requested range80 and use the appropriate energy in our Monte Carlo code as determined by the relationship shown in figure 4.3a. The spot positions are given at isocenter, thus together with the position of the scanning magnets and the exact location of the nozzle relative to isocenter one can transform these easily to the position and momentum of each spot at nozzle exit. Together with the energy-dependent spot size, which is tabulated as well, we have now all the necessary information to create a phase space distribution of protons at nozzle exit. As we start our simulations just before the surface of the patient, we assume a parallel beam without divergence, as scattering becomes the main factor affecting the path of the protons as soon as they enter the patient.

To determine the number of protons delivered per spot is straightforward. The weight of the spot w_i is given by our treatment planning system in units of gigaprotons (Gp). Thus, we can simply introduce a spotfactor S, which determines the number of protons to be simulated per Gp prescribed. The Bragg peak database within the treatment planning system has been corrected with a small range dependent correction factor $C_D(\text{range80})$, which is a necessary to fit the absolute dose in the center of a broad field to measurements (for details see [27]). Including this correction, we simulate

$$w_i[Gp] \cdot S \cdot C_D(\text{range80}) \tag{4.1}$$

protons per spot. Generally we use a spotfactor of 10^5, meaning that we simulate approximately 1 in 10^4 protons that are actually delivered in the clinic. The exact spotfactor chosen for a simulation can vary, since the spot weight also depends on the total dose delivered in a given treatment. During the simulation the dose is scored in Gy and simply scaled by $10^9/S$ after the simulation to yield the absolute dose in the patient. Thus, through the use of direct mapping between Bragg peak intensities given by the treatment planning system and the measured current in the reference ionization chamber, one can perform truly absolute Monte Carlo simulations of dose inside the patient.

This approach is more direct than in Monte Carlo simulations of passively scattered fields, where a normalization run in a water phantom and knowledge of the prescribed dose per field is necessary to normalize the energy deposited in the patient [100]. The reason for this is that most treatment planning systems prescribe a dose or a beamweight to a beam, while ASTROID determines directly the number of protons to be delivered.

4.3.1 Patient Simulations

Having characterized the relevant beam parameters, we can now use this information to create a phase space at nozzle exit and perform absolute dose Monte Carlo simulations in patients. To demonstrate our implementation we analyze fields that are part of clinical treatment plans for three different patients with varying degrees of complexity in geometry: liver, head and neck, and lung. The patients have originally been treated with passively scattered proton therapy and we used the same beam directions to create the active scanning plans. The spotfactor S used for the Monte Carlo simulations was variable, so as to simulate approximately the same number of protons ($\approx 10^7$) for each field.

Figure 4.8 shows the results of the simulations: the first two images in each row display the results for Monte Carlo (MC) and pencil-beam (PB) simulations respectively, while the difference picture on the right shows the difference in absolute dose, i.e. [Dose(MC) - Dose(PB)].

The first row shows the results for the anterior-posterior (AP) field of a patient treated for hepatocellular carcinoma. The patient was originally treated using passive scattering to a prescribed dose of 58.05 Gy(RBE). The field presented in the figure is part of the active scanning plan and delivers a maximum dose of 30

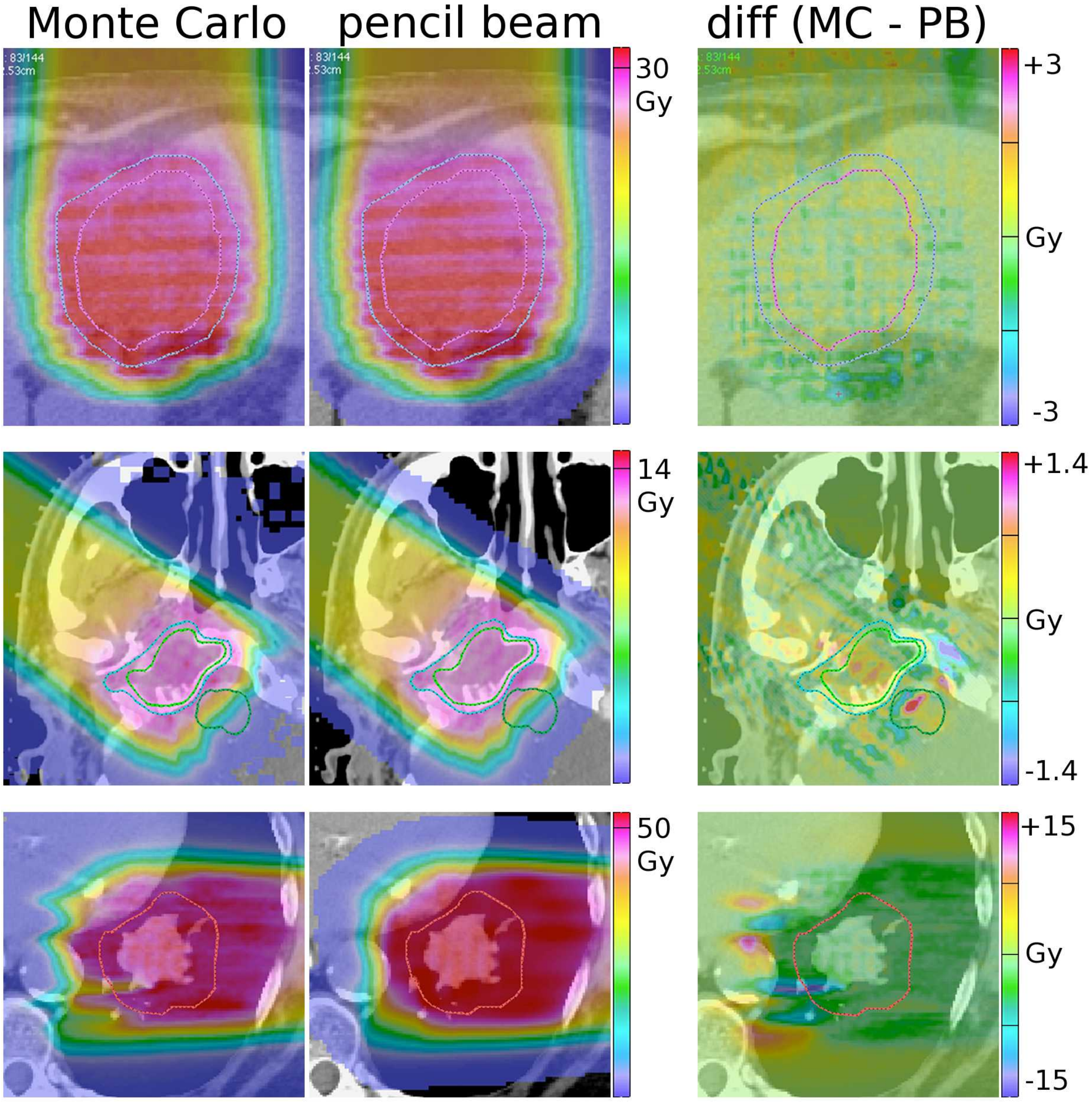
Monte Carlo
pencil beam
diff (MC - PB)
83/144
53cm
30
Gy
+3
Gy
-3
14
Gy
+1.4
Gy
-1.4
50
Gy
+15
Gy
-15

Figure 4.8: Top row: anterior-posterior field in liver patient, structures on display are the clinical target volume (CTV, pink) and the planning target volume (PTV, blue). Middle row: head and neck patient, visible structures are gross tumor volume (GTV, green) and CTV (blue). Lower row: lung patient, red line indicates the CTV. All values given are Gy(RBE). The scale of the difference image on the right is 10% of prescribed dose for row 1 and 2, while 30% for row 3. Red areas in the diff(MC-PB) images indicate higher dose in the MC simulations, blue areas higher dose in the TPS.

Gy(RBE). The dose yielded by Monte Carlo simulations agrees well with the dose predicted by the treatment system, as is expected for such a simple geometry. Even the dose ripples within the field are reproduced and the difference picture on the right does not show significant variations (agreement within ±2%).

The second row shows the field of a treatment plan for a petroclival meningioma, originally treated with passive scattering using 4 fields. The dose predicted by Monte Carlo deviates more from the treatment planning system than in the liver case. Especially in the area in which the zygomatic bone introduces a sharp lateral inhomogeneity in the beam path, the difference in the handling of multiple coulomb scattering apparently leads to dose differences of up to 5% at some points within the CTV and up to 10% in the brainstem.

A field in a treatment plan for a lung patient is shown in the bottom row. This patient was originally treated with photons, we re-planned it with a coplanar 2-field treatment plan to a prescribed dose of 87.5 Gy(RBE), adhering to clinical constraints for mean lung dose and lung V20 (the percentage of normal lung that receives more than 20 Gy(RBE)).

The bone-lung interfaces in the beam path lead to increased multiple coulomb scattering and due to the extension from gross tumor volume to clinical target volume the distal fall-off is situated in lung tissue. This represents a similar situation as in the lung phantom discussed in the last chapter (3), leading to a magnification of range errors in low-density tissue. The observed range differences between the Monte Carlo simulations and the analytical algorithms are significant. Note that compared to the first 2 patients in figure 4.8, the scale of the difference image for the lung patient is ±30% of the prescribed dose. Monte Carlo predicts differences in the heart, the descending aorta and the spine, and even significant underdosage stretching right into the CTV (contoured in red). While the range differences seem large, it must be kept in mind that event though for example the aorta is located around 20 mm behind the target, this is just ≈5 mm in water-equivalent pathlength.

The differences observable in figure 4.8 are due to differences in the modeling of multiple coulomb scattering of the protons in the patient. The analytical algorithm assumes that the interactions along each computational pencil beam's central axis (a so called *bixel*, see chapter 2.3.1) are representative within the whole proximity of other affected voxels. This makes pencil beam models insensitive to lateral inhomogeneities, where bone-tissue interfaces can lead to a lateral disequilibrium of scatter. Additionally the pencil beam algorithm assumes all media are water-like in scattering, meaning the physical depth is converted to its water-equivalent and the scattering width is based on this parameter alone.

In Monte Carlo on the other hand the chemical composition of the tissue is taken into account when calculating the interaction cross sections for scattering, so bone will scatter differently from lung or water. The particles are also transported step-by-step through the voxelized patient anatomy and this determines the resulting angular and spatial distribution of the protons.

4.4 Discussion

The steep dose gradients present in proton fields cannot be fully utilized whilst uncertainties in the proton range are still prevalent. The range differences demonstrated here stem from approximations in the modeling approach of pencil-beam algorithms. Yet range uncertainties arise also from other sources, such as incorrect patient setup and CT calibration uncertainties. Approaches to mitigate these are under development: robust planning can reduce the impact of setup uncertainties [25], image guidance techniques minimize the errors in setup themselves [32,132] and dual-energy CT is under investigation to reduce the uncertainty in Hounsfield Unit to stopping power conversion [146].

We derived the initial beam energy spread using a published analytical model by Bortfeld, described in detail in section 2.1.4. Other groups have determined the energy spread by obtaining a set of mono-energetic peaks and then weighing them with a Gaussian distribution [27, 66] By fitting this weighted sum to the measured data, they were able to determine the mean energy E_0 and standard deviation σ_E of the peak. This method does not necessarily produce a unique solution, but has shown to yield results with sufficient accuracy. Theoretically, one could also model the accelerator and the beam transport system up to the nozzle to determine the initial energy spread [21].

Our simulations use a phase-space based approach, i.e. we characterized the beam at nozzle exit and from this point we also start tracking protons. The advantage of this approach is its simplicity: all that is needed is a thoroughly tested Monte Carlo code capable of patient simulations based on CT data, TOPAS in this case, and a set of measured Bragg peaks from the Gantry. The exact nozzle geometry does not have to be modeled, which saves time (tracking of protons through magnetic fields is especially time-intensive) and effort, since no blue prints and material composition have to be obtained.

For passive scattering (as used in the last chapter) this approach would not be feasible, due to the interactions taking place with the components in the beam's path, such as range modulator wheels and scatterers. Event though in active scanning there is almost nothing in the beam path, some particles can undergo wide-angle scatter due to interactions with the ionization chambers. Such interactions are not accounted for in the approach used here. For modeling far out-of-field doses in distant organs for secondary cancer risk estimation, this approach is therefore inadequate and a full simulation of the scanning nozzle is advisable [34]. For the high-dose regions within the treatment field and comparisons to the treatment planning system on the other hand, phase-space based simulations are sufficient, as our simulations in water and patient cases show. Our approach also allows studying the effect of hardware on scanning treatments, as we can start our phase space upstream of any patient specific apertures or range compensators that might be employed to reduce the lateral penumbra.

The above method to calibrate the Monte Carlo code to the measured depth dose curves used by the treatment planning system does not guarantee proper modeling of the *halo* in the latter, i.e. the contribution of large angle scattering that forms a low dose envelope around the primary pencil beam. This is usually modeled by a second Gaussian in the lateral beam profile, and can be parameterized using input from simulations or measurements [27, 106, 114, 115].

4.5 Conclusion

The characterization of all beam parameters at nozzle exit, together with the exact number of protons to be delivered from the treatment plan, enabled us to perform absolute dose Monte Carlo simulations of treatments plans in patients. As expected, the agreement is excellent for a simple case such as liver, where the agreement is within 2% for most of the volume, while deviations of up to 30% can arise in complex geometries such as lung.

Using the well calibrated active scanning Monte Carlo simulations presented here, we hope to gain further understanding under which circumstances the results in the patient deviate significantly from those produced by pencil-beam calculations and facilitate developments to increase their accuracy.

Chapter 5

Quantifying the Interplay Effect in Patients

Contents

5.1 Tumor Motion in Radiotherapy Patients 54
5.2 Study Details 54
  5.2.1 Treatment Planning 55
  5.2.2 Active Scanning Delivery System 56
  5.2.3 Monte Carlo Simulation and Post-Processing 56
  5.2.4 Simulation of Fractionation: the n-fraction approximation . . 58
  5.2.5 Metrics to assess the Interplay Effect 59
5.3 Results 60
  5.3.1 Interplay Effect in the Normal Lung 60
  5.3.2 Interplay Effect in the Target: Dose Distribution 61
  5.3.3 Interplay Effect in the Target: TCP 62
5.4 Discussion 64
5.5 Conclusion 65

After validating our Monte Carlo code against experiments (chapter 3) and matching its calculations in water to the treatment planning system (chapter 4), we can now take a step further and introduce motion into the simulations[1].

As already discussed in the introduction, spot scanning proton therapy has been shown to outperform passively scattered proton therapy, especially for targets of high geometric complexity [149]. However, for targets that move during irradiation there is interference between dynamic pencil beam delivery and target motion, typically referred to as interplay effect, as described in chapter 1.3. In passively scattered proton therapy, where all parts of the field are essentially delivered simultaneously, this effect is not significant [65].

Previous studies [10, 69, 74] were limited by the use of rigid image registration, small number of patients and analytical dose calculation methods, which are expected to have significant uncertainties in lung. In this study we use the current state-of-the-art Monte Carlo dose calculation and deformable image registration methods, applied to ten clinical lung cancer patients.

---

[1] Results from this chapter have been presented as oral presentation entitled *"Four-dimensional Monte Carlo simulations of lung cancer patients treated with proton beam scanning to assess interplay effects"* at the 2012 Annual Meeting of the American Association of Physicists in Medicine (Charlotte, USA) and have been published [49].

The aim of this chapter is to answer the following questions:

i. What is the magnitude and spectrum of tumor amplitudes observed in lung cancer patients?

ii. How does the interplay effect vary with tumor motion amplitude?

iii. Is there an impact of the spot size on the interplay effect?

iv. How much does conventional fractionation mitigate the interplay effect?

Table 5.1: Studies reporting tumor motion for lung cancer patients undergoing radiotherapy.

Observer	Nr of patients	Method	observed motion [mm]		
			Sup-Inf	Ant-Post	Right-Left
Barnes *et al.* (2001) [6]	10	fluoroscopy	18.5 (9-32) lower lobe 7.5(2-11) middle/upper lobe	-	-
Britton *et al.* (2007) [17]	8	4DCT	8.6±1.9	3.9±0.8	1.9±0.5
Chen *et al.* (2001) [24]	12	-	(0-50)	-	-
Ekberg *et al.* (1998) [36]	20	fluoroscopy	3.9(0-12)	2.4(0-5)	2.4(0-5)
Erridge *et al.* (2003) [38]	25	EPIs	12.5±7.3(6-34)	9.4±5.2(5-22)	7.3±2.7(3-12)
Guckenberger *et al.* (2007) [53]	27	CBCT	81% < 10, 19% > 10mm, abd. comp. used for > 5		
Guckenberger *et al.* (2009) [52]	17	CBCT	12±6.3, 47% > 10		
Hanley *et al.* (1999) [56]	5	CT & spiro	12(1-20)	5(0-13)	1(0-1)
Korreman *et al.* (2012) [73]	46	4DCT(39)/fluo(7)	6.4 , >10 in 22% , >20 in 7%		
Liu *et al.* (2007)[a] [78]	152	4DCT w rigid reg.	5 (11%>10)	2.1	1.2
Michalski *et al.* (2008) [85]	22	4DCT	11.7±8.2 , >10 in 50% , >20 in 32%		
Mori *et al.* (2007) [89]	14	256MS-CT	10.3±7.1	4.0±2.3	1.9±1.6
Muirhead *et al.* (2011) [91]	20	4DCT	7.3(2-13.8)	-	-
Murphy *et al.* (2002) [93]	13	radiography	7(2-15)	-	-
Ong *et al.* (2011) [96]	20	4DCT	8.8 , >10 in 40% , >20 in 15%	-	-
Pantorotto *et al.* (2009) [102]	41 (100 nodes)	4DCT	6.8 (1.7-16.4) , >10 in 10%		
Plathow *et al.* (2004) [110]	20	MRI	lower lobe 9.5 (4.5-16.4) middle lobe 7.2 (4.3-10.2) upper lobe 4.3 (2.6Ð7.1)	6.1 (2.5-9.8) 4.3 (1.9-7.5) 2.8 (1.2-5.1)	6.0(2.9-9.8) 4.3 (1.5-7.1) 3.4 (1.3-5.3)
Purdie *et al.* (2007) [111]	28	4DCT	upper/middle lobe: 4.2 lower lobe: 6.7 (mostly with abd. comp.)		
Richter *et al.* (2010) [112]	30	4DCT	6.54, 20% > 10		
Seppenwoolde *et al.* (2002) [122]	20	fluoroscopy	5.8(0-25)	2.5(0-8)	1.5(0-3)
Shirato *et al.* (2006) [125]	21	RTRT	10.7±8.6 **max speed:**	8.8±7.0 21.1±18.9 mm/s	8.2±6.5
Shah *et al.* (2012) [123]	120	CBCT	4.6±5.0	1.7±1.3	1.1±1.0
Sixel *et al.* (2003) [126]	10	fluoroscopy	(0-12.8)	(0-4.4)	(0-3.2)
Sonke *et al.* (2008) [129]	56	CBCT	9 average, >10 in 35%, >20 in 10-15% of patients		
Stevens *et al.* (2001) [133]	12	orth. radiographs	8 ± 4 (3-22)	-	-
Suh *et al.* (2008) [134]	42	cyberknife	4.8 peak-to-peak, >5 in 40% of fractions		

---

[a] all patients with 4DCT artefacts and those where rigid-body registration didn't work to assess tumor motion were excluded.

5.1 Tumor Motion in Radiotherapy Patients

Table 5.1 shows studies reporting the motion amplitude of lung tumors and lymph nodes in patients undergoing radiotherapy. It is important to include only publications which report unbiased estimations of patient populations that were not pre-selected, meaning that for example studies investigating gating were mostly excluded, as they will most probably select patients based on significant motion amplitude.

Unfortunately those studies do not all report motion the same way, and some only report an average value. Drawing on 20 of the studies listed above we can derive an approximate motion spectrum of patients in the clinic, as shown in figure 5.1. The average motion is 7.7mm based on 509 patients, 28% of the tumors move more than 10mm (based on 356 patients) and 9% >20mm (based on 288 patients).

These values are based on 3D motion estimations, though in all studies the main motion direction reported was cranio-caudial. The tumor motion is correlated to other factors as well, such as clinical stage and performance status of the patient.

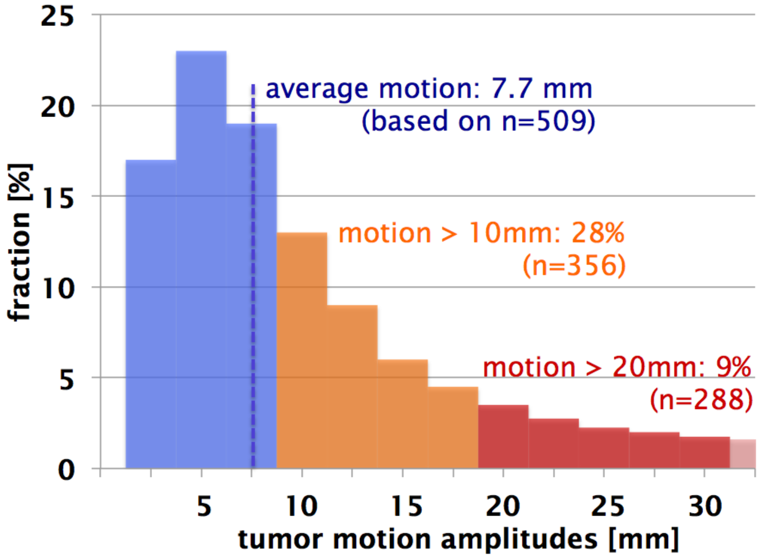

Figure 5.1: Spectrum of motion amplitudes based on the studies in table 5.1.

5.2 Study Details

Ten patients treated for lung cancer at our institution were retrospectively included in this study. Cases were selected to give a representative range of tumor motion, volume and location. Table 5.2 gives an overview over peak-to-peak motion amplitude, gross tumor volume (GTV) in end-exhale and the average delivery time per field.

Patient #	motion amplitude [mm]	GTV volume [cc]	delivery time per field [s]
1	30.6	21.1	65
2	3.5	64.9	99
3	10.7	26.0	65
4	20.2	82.3	63.5
5	14.6	4.0	19
6	10.0	21.7	59.5
7	5.1	2.6	17.5
8	15.1	15.4	40
9	9.1	24.5	79.5
10	2.9	33.9	63.5

Table 5.2: Patient characteristic: motion amplitude (peak to peak), tumor volume and average delivery time per field.

5.2.1 Treatment Planning

The treatment planning method was based on a clinical trial (ClinicalTrials.gov ID: NCT00495040) [23]. The internal gross tumor volume (IGTV) was outlined on the maximum intensity projection CT (MIP-CT) and validated on the 4D-CT, to ensure it encompassed the gross tumor volume (GTV) in every phase. The clinical target volume (CTV) was defined as the GTV plus an 8mm margin to account for microscopic disease, with the ICTV encompassing the CTV in all phases. A conventional planning target volume (PTV) was defined as a 5mm isotropic extension of the ICTV to account for uncertainties in patient setup and deformable image registration (DIR).

Treatment plans were designed on the average intensity projection CT (ave-IP CT) with the IGTV volume set to a generic tumor density (HU=50). This approach has been shown to provide adequate tumor-coverage, while minimizing treatment uncertainties and dose to normal tissue [65].

We used the ASTROID treatment planning system for proton beam scanning as described in a previous chapter (2.3). The prescription dose was 87.5Gy(RBE), delivered to >99% of the ICTV and >95% of the PTV. All plans employed 2 coplanar fields and satisfied our target coverage requirements and the clinical normal tissue constraints [83]. Beam angles were chosen to minimize lung dose and to avoid placing a distal edge immediately proximal to a critical structure. The dominant motion direction was perpendicular to both beams for all patients, i.e. cranio-caudial. Normal lung was defined as the combined lungs, excluding the IGTV. The spot spacing is expressed relative to the spot size: we used a spacing of 1 sigma per default, reducing it to 0.7 sigma only if necessary to satisfy target coverage requirements.

5.2.2 Active Scanning Delivery System

The simulation of the delivery was based on the hardware available at Massachusetts General Hospital. We planned and simulated two different spot sizes, where the BigSpots (BS) sigma varies between 8-17mm (230-70MeV). The smallest spot size currently used for proton treatments has a sigma of 2-4mm (230-70MeV), which we define as SmallSpots (SS) [105]. The treatment plans for the 10 patients were comprised of spot energies between 100-170MeV, reducing the used spot sizes to 11-15mm for BigSpots and 2-3mm for SmallSpots. Figure 5.2 shows the energy-dependent spot sizes for BigSpots and SmallSpots used in the simulations.

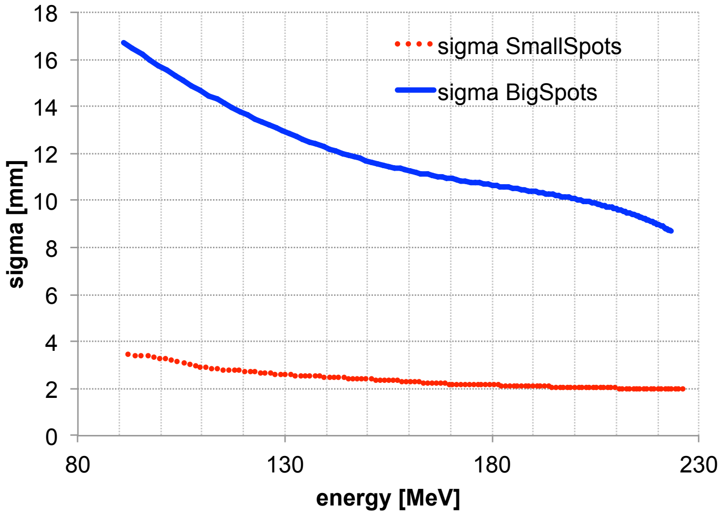

Figure 5.2: Energy-dependent spot size for the gantry at MGH (blue) and PSI Gantry 2 (red). PSI values are the minimum values achievable and might be slightly larger in clinical practice.

The dynamic delivery was simulated using energy switching time of 1 second and lateral scanning speeds of $3/30\frac{m}{s}$ in x/y direction. There was a $5ms$ spot settling time before beam delivery, to allow for settling of the magnets and the associated field, and the delivery time of each spot was based on a beam current of $2nA$.

5.2.3 Monte Carlo Simulation and Post-Processing

Figure 5.3 shows an overview of the study design. After treatment planning (I. in the figure), Monte Carlo (MC) techniques were used to simulate the delivery to the patient. All calculations employed TOPAS, as described in chapter 2.2.2.

In arm A, the fluence maps acquired from the treatment planning system were delivered to the static ave-IP CT, using an automated suite of scripts (MCAUTO-3D, II. in figure 5.3). The resulting dose distributions are denoted as static.

For arms B and C, MCAUTO-4D (III. in figure 5.3) retrieves the 4D-CT and combines it with the timing information of the proton gantry to deliver the pencil beams to the appropriate phase in the breathing cycle. The resulting dose distributions are then deformed back to the reference phase (T50=end exhale) using

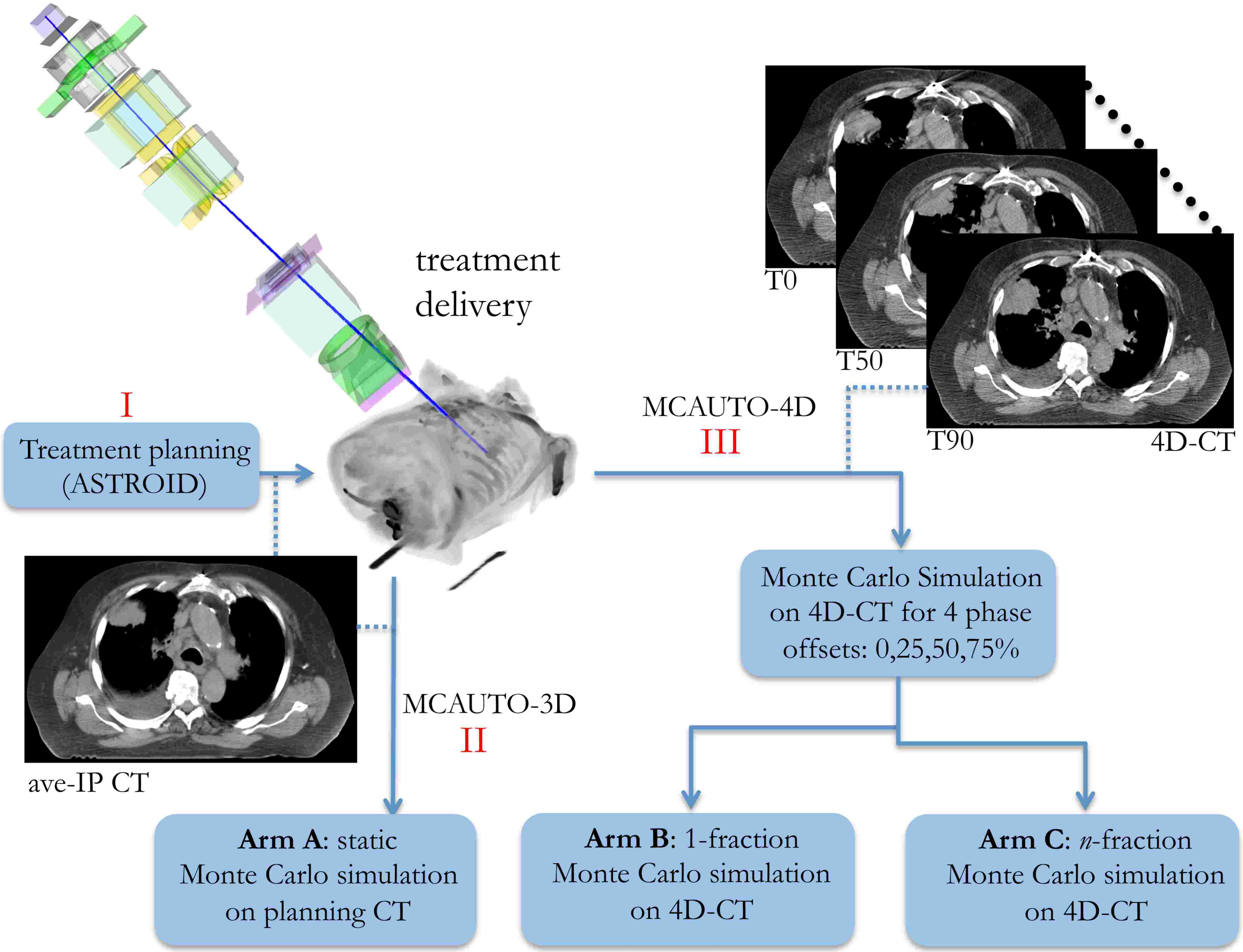
treatment
delivery
I
Treatment planning
(ASTROID)
ave-IP CT
MCAUTO-3D
II
MCAUTO-4D
III
T0
T50
T90
4D-CT
Monte Carlo Simulation on 4D-CT for 4 phase offsets: 0,25,50,75%
Arm A: static Monte Carlo simulation on planning CT
Arm B: 1-fraction Monte Carlo simulation on 4D-CT
Arm C: *n*-fraction Monte Carlo simulation on 4D-CT

Figure 5.3: Study design in detail. Red roman numerals denote the processes: treatment planning (I), scripts for 3D simulation (II) and for 4D simulation (III).

deformable image registration (DIR). To this end we use *plastimatch*, a toolkit that has been described in chapter 2.4 and extensively benchmarked [92].

For each patient, 4 different starting phases were simulated to determine any variation in the interplay effect based on the initial phase. Simulations were performed with the scanning treatment starting at T0 (peak inhale), T25 (mid exhale), T50 (end exhale) and T75 (mid inhale). This yielded 4 dose distributions with varying interplay effect as shown in figure 5.4a-d for patient 1. The values reported for the 1-fraction case (arm B), are the average of the values of each metric obtained from these 4 dose distributions.

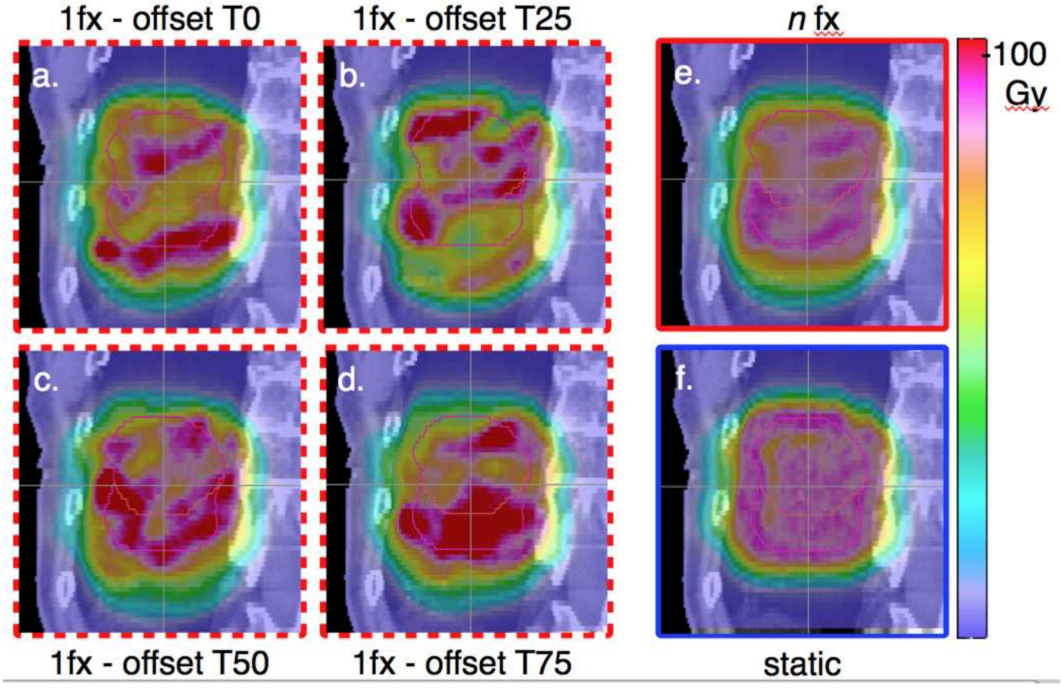

Figure 5.4: Sagittal view of the dose distributions for patient 1 with CTV in end-exhale phase (red, small contour) and ICTV (pink, large contour). a-d denote the 1-fraction cases for the 4 initial phases, e the n-fraction and f the static case.

5.2.4 Simulation of Fractionation: the n-fraction approximation

We define the n-fraction case (arm C, n=35, 2.5Gy/fx) as the average of the dose distributions from the 4 initial phases, as illustrated in figure 5.4: 5.4a-5.4d show the dose distributions for the 4 starting phases, revealing over- and under-dosage within the target. Averaging these 4 to arrive at the n-fraction case (5.4e), the hot- and cold-spots are reduced, yielding a dose distribution similar to the static case (25.4). The quantities reported for n-fractions are the values obtained from this average dose distribution (25.4).

Averaging the distributions of the 4 starting phases is a valid assumption, since it can be expected that at the delivery of each fraction, scanning would start at a random phase, leading to an even distribution after many fractions.

Our estimation of the n-fraction case rests on the following assumptions, which all cause a conservative assessment of the interplay effect:

1. We use 4 different starting phases to calculate the n-fraction case, notwithstanding it would be more accurate to use more starting points for the average. However, the interplay effect is thus overestimated: using more initial phases would lead to a more homogeneous dose distribution, since an even wider array of distributions to average would wash out the inhomogeneities caused in the delivery of single fractions to a greater extent.

2. We rely on a single 4D-CT scan, which assumes that the patient breathes the same way during a whole course of fractionated therapy lasting weeks. Varying the tumor trajectory for different fractions would decrease the interplay, since the same rationale holds true as for point 1.

3. We do not include a biological equivalent dose (BED) correction to account for the fact that different parts of the tumor receive on some days more, on some days less, dose. By not correcting for essentially non-uniform fraction sizes to different tumor sub-volumes, we underestimate the biological effect within the tumor. The concave dose response curve for doses relevant to this study means a non-uniform fractionation will always yield a biological effect greater or equal than uniform fractionation.

This n-fraction approximation estimates the interplay effect that can be expected over a conventionally fractionated treatment.

Finally, we note that this method, particularly point 2, assumes the tumor stays within the drawn IGTV over the course of the whole treatment. Geometrical misses due to increasing motion or a non-representative 4D-CT are not considered.

5.2.5 Metrics to assess the Interplay Effect

To quantify the impact of interplay on the target dose distribution, the minimum dose (D_{min}), maximum dose (D_{max}), mean dose (D_{mean}), the dose homogeneity quantified by D_{5-95} and the EUD (see chapter 2.5)were analyzed.

To estimate the effect on treatment outcome, the tumor control probability (TCP), given by the 2-year local control rate (2y-LC) was calculated. The values used for the 2y-LC calculations were taken from Willner *et al.* [141] (γ_{50}=3.52 and D_{50}=74.5).

Additionally, changes in mean lung dose (MLD) and in the volumes of normal lung receiving at least 20 and 5 Gy(RBE), V20 and V5 respectively, were calculated to determine any effect on normal lung resulting from interplay.

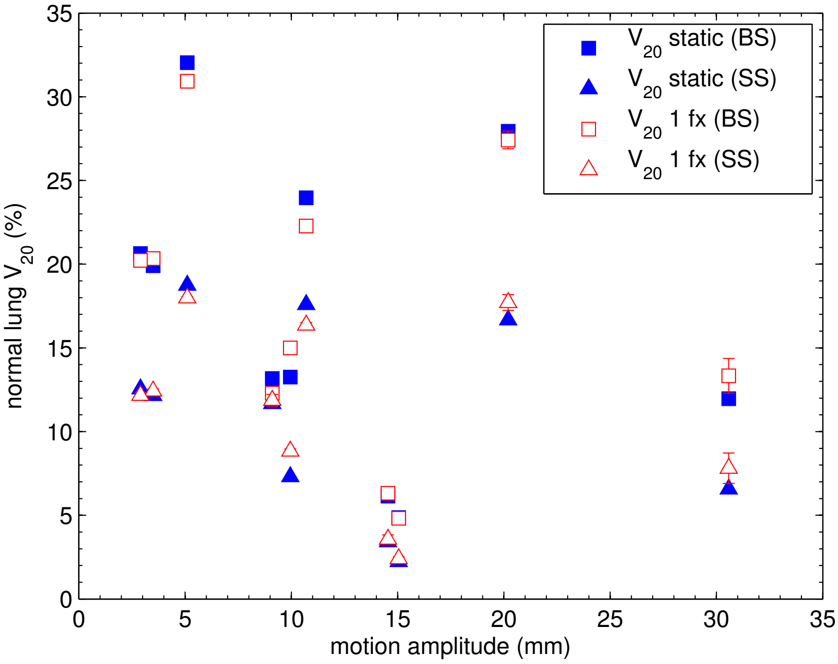

Figure 5.5: Percentage of healthy lung receiving 20Gy(RBE) or more, plotted against tumor motion amplitude. Squares denote BigSpots (BS), triangles SmallSpots (SS), full blue symbols the static values and open red ones the 1 fraction average.

5.3 Results

5.3.1 Interplay Effect in the Normal Lung

The V20 and V5 are often used during treatment planning to dictate the number of beams and their angles. The change in V20 and V5 for a single fraction compared to the static plan is on average -0.12±0.9%(range -1.4% to 1.5%) and 0.22%±1.1%(range -1.0% to 2.7%) for BigSpots, 0.12±0.7%(range -1.0% to 1.2%) and 0.52%±1.3%(range -1.1% to 3.2%) for SmallSpots. The average MLD occurring in all patients is 11.6Gy(RBE) (range 3.1-23.5) for BigSpots and 7.3Gy(RBE) (range 1.7-13.0) for SmallSpots. The changes caused by the interplay effect are $<$0.6Gy(RBE) for all patients. There is no significant correlation to tumor motion (Spearman's p $>$0.21 for all parameters above) for these patients.

Figure 5.5 shows normal lung V20 values for all patients plotted against the tumor motion amplitude for the static cases and including motion. The influence of motion is limited and does not have a consistent effect on the dose to the normal lung, as the location of hot- and cold-spots may vary, though the integral dose to the lung remains almost constant.

The difference in MLD between the spot sizes is primarily due to the larger penumbra of BigSpots, which leads to a higher volume of normal tissue being irradiated. This is also demonstrated in Figure 5.5, which shows that the V20 for the smaller spot size is consistently smaller, up to a factor ≈2.

5.3.2 Interplay Effect in the Target: Dose Distribution

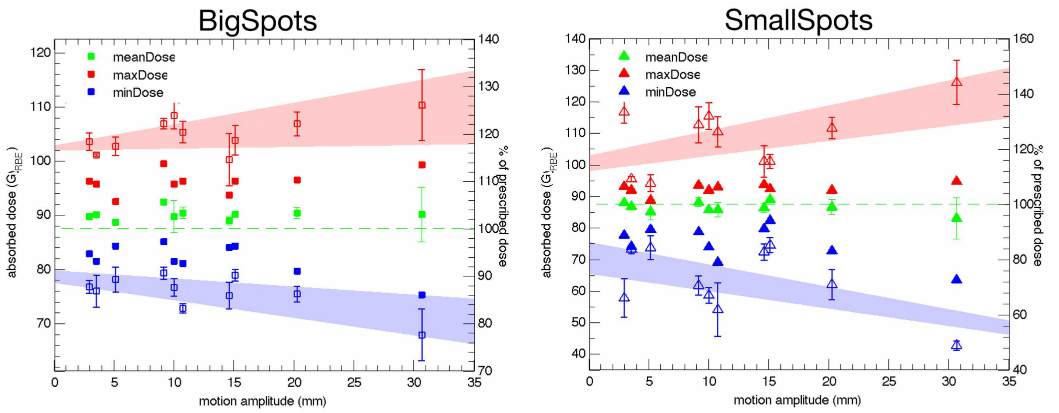

Figure 5.6: D$_{min}$ (blue), D$_{max}$ (red) and D$_{mean}$ (green) values for the CTV for the 1-fraction (open symbols) and n-fraction (closed symbols) case. The open and closed D$_{mean}$ symbols coincide. The error bars for the 1-fraction values represent the standard deviation of the 4 initial phases. The shaded areas represent a linear fit through the maximum and minimum values among the initial phases to guide the eye.

Figure 5.6 demonstrates the effect of motion on D$_{min}$, D$_{max}$ and D$_{mean}$ in the CTV. The 1-fraction values for D$_{min}$ and D$_{max}$ show a clear relationship with tumor motion. The effect is more pronounced for the SmallSpots, where the minimum dose in the CTV drops to 49% of the prescribed dose for the largest motion studied, compared to 78% for the same patient and motion amplitude using the larger spot size.

The 1-fraction mean dose stays within ±1.2% of the static plan for all motion amplitudes, except for a small systematic loss (-3%) for the SmallSpots machine and the highest motion amplitude. The standard deviation increases with motion amplitude, implying that in the delivery of a single fraction, larger motion is more likely to cause a mean dose which differs from the static plan. The stability of the average mean dose confirms that the dosimetric impact on D$_{min}$ and D$_{max}$ is due to interplay.

There is a distinct difference in the D$_{min}$ and D$_{max}$ values for the 1-fraction and n-fraction cases. Fractionation partly mitigates the creation of hot- and cold-spots, as they occur at different locations for each starting phase.

D$_{min}$ and D$_{max}$ are widely used clinically, however they refer to a single voxel and thus may overestimate the dose degradation resulting from interplay. Previous work [69] has used D$_{5-95}$ as measure of the homogeneity of the dose distribution.

Figure 5.7 shows the change in D$_{5-95}$ for BigSpots and SmallSpots for the 1-fraction and n-fraction cases as a function of motion amplitude. For the static case, the DVH fall-off is comparable between the two spot sizes for all patients. If the plans are delivered on the 4D-CT, the 1-fraction values differ significantly between the two spot sizes. On average, the increase in D_{5-95} is 5.6±4.2% of prescribed dose for BigSpots compared to 15.8±11.1% for SmallSpots.

The n-fraction values show little interplay effect for all motion amplitudes, except for the largest motion and small spot size. In that case D_{5-95} increases by 9.48Gy(RBE), i.e. 10.8% of the prescribed dose.

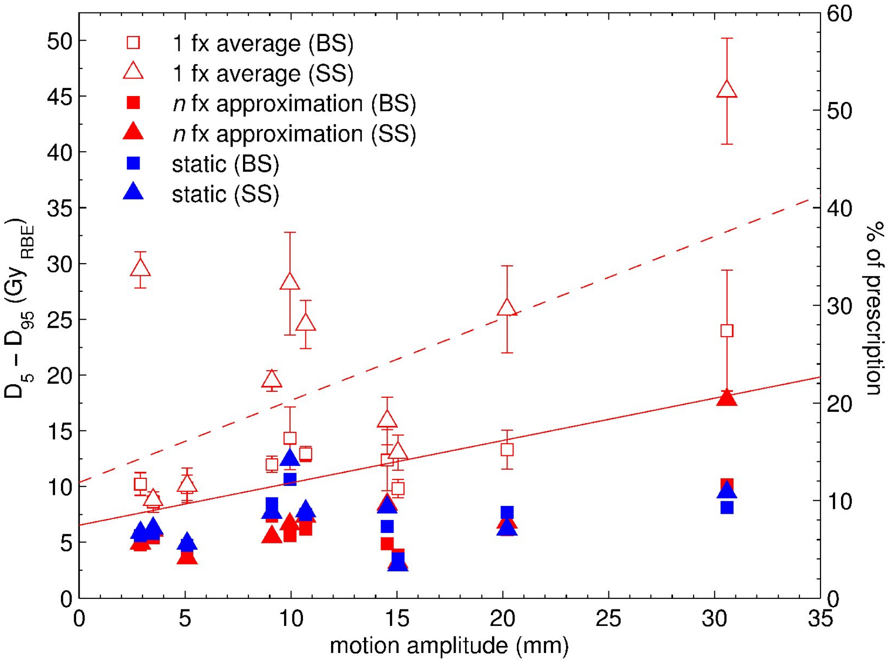

Figure 5.7: D_{5-95} values for the CTV for the 1-fraction (open symbols) and n-fraction (closed symbols) case for BigSpots (squares) and SmallSpots (triangles). Blue symbols denote the static case. The error bars for the 1-fraction values represent the standard deviation of the 4 starting phases. The lines represent a linear fit through the 1-fraction values to guide the eye (full line: BigSpots, dotted line: SmallSpots).

Figure 5.8 shows the EUD as a function of motion amplitude for the BigSpots and SmallSpots machines. The average reduction for the large spot size is consistently $<5\%$ of the prescribed EUD, and for the n-fraction case there is no significant effect of motion, i.e. no EUD reduction in excess of 2% of the prescribed value. For the smaller spot size (figure 5.8b) the reduction in EUD is substantial for some patients, up to 15Gy(RBE) for the largest motion. Also in this scenario the n-fraction values are close to the static prediction, only for the two largest motion amplitudes the deviation is $>2\%$.

5.3.3 Interplay Effect in the Target: TCP

To quantify the change in tumor control, we calculate the 2y-LC for all simulated plans. The 1-fraction value here can be interpreted in 2 different ways: either as the worst-case scenario for a fractionated treatment in which scanning always starts at

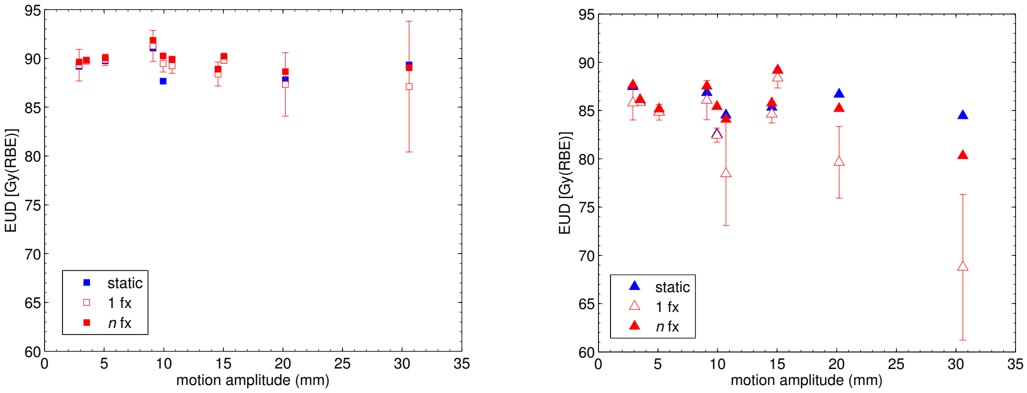

(a) BigSpots (b) SmallSpots

Figure 5.8: EUD values as function of motion amplitude for static (blue symbols), 1-fraction average (open symbols) and n-fraction (closed symbols) case. The error bars for the 1-fraction values represent the standard deviation of the 4 initial phases.

the same phase, or as the 1-fraction scenario where the prescribed dose is deposited at once. In the latter scenario the time to deposit the dose would be longer, possibly leading to additional smearing out of the interplay effect. However, it can serve as an estimation of the maximum TCP reduction in such a scenario.

Figure 5.9 shows the effect of motion on 2y-LC with varying tumor motion. For BigSpots, the TCP for the average 1-fraction case stays within 1.2% of the static case up to 20mm tumor motion amplitude. Only for the patient with >30mm motion, 2y-LC decreases by an average of 7.7±6.2% (for the worst initial starting phase by 14.7%) for the 1-fraction case compared to the static plan. For the n-fraction case, however, TCP is retained for all patients (average change 0.4±0.8%, range -0.4% to 2.4%).

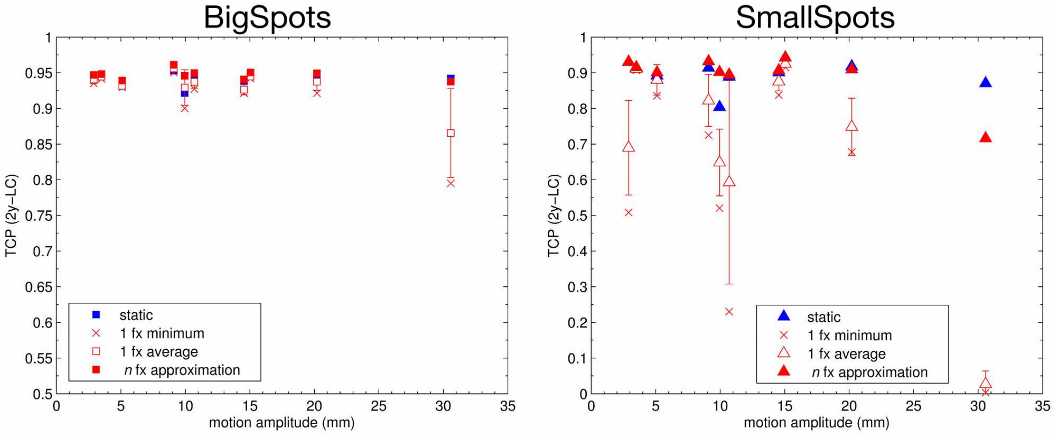

Figure 5.9: 2y-LC for the static (blue symbols), 1-fraction average (open symbols) and n-fraction (closed symbols) case. The error bars for the 1-fraction values represent the standard deviation of the 4 initial phases, and the cross denotes the worst 1-fraction result.

The same trend is visible for SmallSpots, but the magnitude of the changes is greater. The average loss in 2y-LC over all patients is -18.5±25.2%(range -84.3% to -0.3%) for the 1-fraction case. Even though the largest decrease is seen for the highest motion amplitudes, the changes are not significantly correlated with motion (Spearman's p=0.26). For the patient with the lowest motion amplitude the 1-fraction value decreases on average by 24%, while there is little change (-2.5% and -1.8%) for the 2 patients with 15mm motion. It appears motion amplitude alone is not a good predictor of the interplay effect and inter-patient variability is high.

In the n-fraction scenario for SmallSpots, the interplay effect seems to be mitigated for motion amplitudes up to 20mm in this patient cohort, as modeled 2y-LC decreases <0.4%. Only for the patient with >30mm motion 2y-LC drops from 87% to 71.6%.

We did not observe a correlation between any of the chosen metrics and tumor volume (Spearman's p>0.16 for all parameters).

5.4 Discussion

For motion amplitudes <10mm, the n-fraction treatment yields dose distributions more homogeneous than the static plan, as visible in figure 5.7. This is due to the intrinsically imperfect static plan, which always includes some hot- and cold-spots. Small motion averages the dose distribution such that the over- and under-dosage inherent in the static plan is lessened, thereby making it more homogeneous. A similar phenomenon has already been reported for multiple rescans of the target [69].

Bert *et al.* [10] also ascertained the strong influence of starting phase on the interplay effect, yet in our patient cohort the motion amplitude seems to dominate the general appearance of possible interplay effects less: the changes in D_{5-95}, EUD and TCP show little correlation to motion amplitude for the SmallSpots machine. Kraus *et al.* [74] observed a similar averaging out of the interplay effect for a fractionated treatment, which they also approximated by averaging over the initial phases. They also showed that irregular breathing motion, which was not included here, led to less distorted dose distributions.

Interplay effects can be reduced by a variety of techniques. Different re-scanning methods can provide additional averaging out of hot- and cold-spots. Gating reduces the effective motion of the tumor, thereby possibly reducing the interplay, but requires higher confidence in movement reproducibility. Tracking has been studied extensively for carbon-ion beams, but would not necessarily reduce the interplay effect.

To reduce the spot size at any established facility requires significant changes in hardware. However, several methods (e.g. decreasing quadrupole strength, inserting pre-absorbers) can be employed to increase the spot size, thereby making the system more robust against interplay.

5.5 Conclusion

For the 1-fraction scenario, D_{min} and D_{max} show a clear relationship with tumor motion, decreasing and increasing respectively, as the motion amplitude increases. This change is consistently higher for SmallSpots (σ ≈3mm) than for BigSpots (σ ≈13mm). The degradation of target homogeneity is on average a factor of 2.8 higher for SmallSpots than for BigSpots.

Even in the presence of the interplay effect from tumor motion up to ≈30mm, local control is preserved using a large spot size and conventional fractionation for this patient cohort. Thus gating may not be required for treatments with these characteristics, except when its main purpose is to reduce the dose to normal lung. For motion amplitudes less than ≈20mm, the large spot size mitigates deterioration in modeled 2y-LC for the delivery of a single fraction in our patient population.

For treatments with a small spot size, conventional fractionation retains dose homogeneity for motion less than ≈20mm in our patient group. In the delivery of single fractions, however, modeled 2y-LC falls on average by 18.5%. The deterioration of the dose distribution is highly patient-specific, and is not predicted accurately by tumor motion amplitude alone.

While the smaller spot size is significantly less robust toward motion, we want to highlight that it also reduces dose to the normal lung considerably due to the sharper lateral penumbra, as can be seen in the different MLD values.

Hypofractionated regimens consisting of only a few fractions are not specifically simulated here, though it can be expected that the interplay effect in such a case will be bound by our estimates of the 1-fraction case and the n-fraction approximation.

Chapter 6

Mitigating the Interplay Effect in Patients

Contents

6.1 Study Details 67

6.1.1 Motion Mitigation Techniques 69

6.2 Results 71

6.2.1 Effect of Motion Mitigation in Tumor 71

6.2.2 Effect of Motion Mitigation in Lung Tissue 73

6.3 Discussion 73

6.4 Conclusion 77

In the previous chapter we have investigated the extent of the interplay effect for two different spot sizes in the delivery of single fractions and estimated it for conventionally fractionated treatments. The results demonstrate that fractionation can play a large role in mitigating the interplay effect for motion amplitudes up to 20mm.

In the last years studies have shown improved survival for lung cancer patients treated with *hypofractionated* regimes [64, 103]. Hypofractionation refers to large doses given to the tumor in usually less than 5 fractions, compared to >30 fractions for conventionally fractionated treatment courses. This prevents averaging of the hot- and cold-spots created by the interplay between beam and tumor motion and necessitates motion mitigation techniques.

The aim of this chapter[1] is to investigate various forms of rescanning and gating (described below) to mitigate the interplay effect in five lung cancer patients who have previously shown degradation of the target dose distribution through motion.

6.1 Study Details

We selected five patients from the previous study who have shown a significant interplay effect, their characteristics are shown in table 6.1. The treatment planning process was similar to the last study, as described in the previous chapter, with the exception that we deliver now 12Gy(RBE) per fraction, which is a common fraction size in hypofractionated treatment regimens for lung cancer [121]. We studied 2 different energy-dependent spot sizes termed BigSpots (σ = 8-17mm) and SmallSpots (σ = 2-4mm), which represent the extremes used in proton therapy. The energy switching time was set to 1s and the spot settling time, which determines the dead time before delivery of each spot, to 5ms. The spot-spacing was 1σ and varied with energy, similar to the layer-spacing, which was equal to the width80.

---

[1] Results from this chapter have been presented as oral presentation at the Young Investigator Symposium at the 2013 Annual Meeting of the American Association of Physicists in Medicine (Indianapolis, USA), title: *"Motion Mitigation in Active Scanning Proton Therapy for Lung Cancer: a 4D Monte Carlo Study"*. Submission for publication is pending.

The time to deposit a spot is given by

$$\text{time}[s] = \frac{\text{spotweight}[\#p] \cdot q}{\text{beam current}[A]}, \tag{6.1}$$

where $q = 1.602 \cdot 10^{-19}$ C and the spotweight is given in the number of protons to be delivered. We used a constant beam current of 2 nA as currently employed by MGH.

The scanning speed varied depending on the axis, due to the different position of the scanning magnets in the nozzle. The fast magnet is parallel to the SI axis with a maximum speed of $30\frac{m}{s}$ for the lowest energy setting. The other magnet perpendicular to the SI axis has a maximum speed of only $3\frac{m}{s}$. The scanning pattern consists of a zig-zag pattern with the longer axis parallel to the fast scanning direction to minimize scanning time. It has been shown previously that the direction of the fast scanning axis has no consistent impact on the interplay effect [33].

Patient Nr	Tumor Size[cc]	Location	Motion Axis	Motion Amplitude[mm]
1	21.1	RLL	SI	30.6
2	26.0	LLL	SI	10.7
3	82.3	RUL	SI/AP	20.2
4	24.5	RML	SI	9.1
5	33.9	RUL	SI	2.9

Table 6.1: Patient characteristics in rescanning study: tumor size, location, axis of main motion and motion amplitude. Tumor location encoded as [R/L][L/M/U][L] = [Right/Left][Lower/Medium/Upper]Lobe of Lung. SI = Superior-Inferior, AP = Anterior-Posterior.

We assumed a constant breathing period of 5s and for every scenario studied 4 evenly spaced initial breathing phases were simulated: T0% (peak inhale), T25% (mid-exhale), T50% (peak exhale) and T75% (mid-inhale).

Additional to the equivalent uniform dose (EUD) and the dose homogeneity, as quantified by the D_{5-95}, we also analyzed the D_{99}, the dose received by 99% of the target. This quantity is a proxy for the minimum dose received by the tumor, but is more robust to the statistical uncertainties of the Monte Carlo simulation.

6.1.1 Motion Mitigation Techniques

6.1.1.1 Rescanning

Rescanning (also called repainting) refers to the target being scanned multiple times, with each scan only delivering a fraction of the intended dose. It was first proposed by Phillips *et al.* [109] and many ways to rescan a target have been proposed since:

Layered/Volumetric: in *layered* rescanning (also called *slice-by-slice* [113]), the layer of the target volume is repainted several times before changing the energy and irradiating the next energy slice. This minimizes the number of energy changes required, which is usually the slowest part of the beam delivery system. In *volumetric* rescanning the whole 3-dimensional volume is scanned multiple times, including switching between energy layers. In this case the delivery time grows almost linearly with the number of rescans N, as the only time saved is the time to deliver the dose to a spot, which is usually only a small part of the treatment time.

Scaled/Iso-layered: in *scaled* repainting the dose to be delivered in one repainting to each spot is simply $1/N$ for N rescans. The main drawback of this technique is that the dose to be delivered to low-weighted spots with high number of rescannings can become very small, which can lead practical problems in the accurate delivery of these spots. In *iso-layered* repainting on the other hand, the dose per spot at each repainting is kept at a constant value. As a result, spots with different weightings receive a different number of repaintings. This means the spot map to be delivered grows sparser at every painting, representing an issue similar to the traveling-salesman problem [148].

Breath-Sampled: *Breath-sampling* means that the start times of each rescan are evenly distributed throughout the breathing cycle, necessitating further dead times at the end of each painting. If T were the breathing period of a patient for example, 4 times breath-sampled rescanning (4x-BSR) would entail 4 rescans starting at times 0, $T/4$, $T/2$, $3T/4$ throughout the breathing cycle [120].

We have included scaled volumetric and layered rescanning in our study (2x, 4x, 6x, 8x and 10x), as well as breath-sampled volumetric rescanning (BSR, 2x and 4x). Figure 6.1 shows the dose distribution through the transverse slice of a patient without rescanning (6.1A) and employing 2x (6.1B), 6x (6.1C) and 2x breath-sampled (6.1D) rescanning. Figure 6.1F shows the nominal dose distribution on the static planning CT.

6.1.1.2 Gating

Gating has been developed for tumors unable to stay stable because of respiratory motion [95] and is used at several particle therapy centers [82, 86].

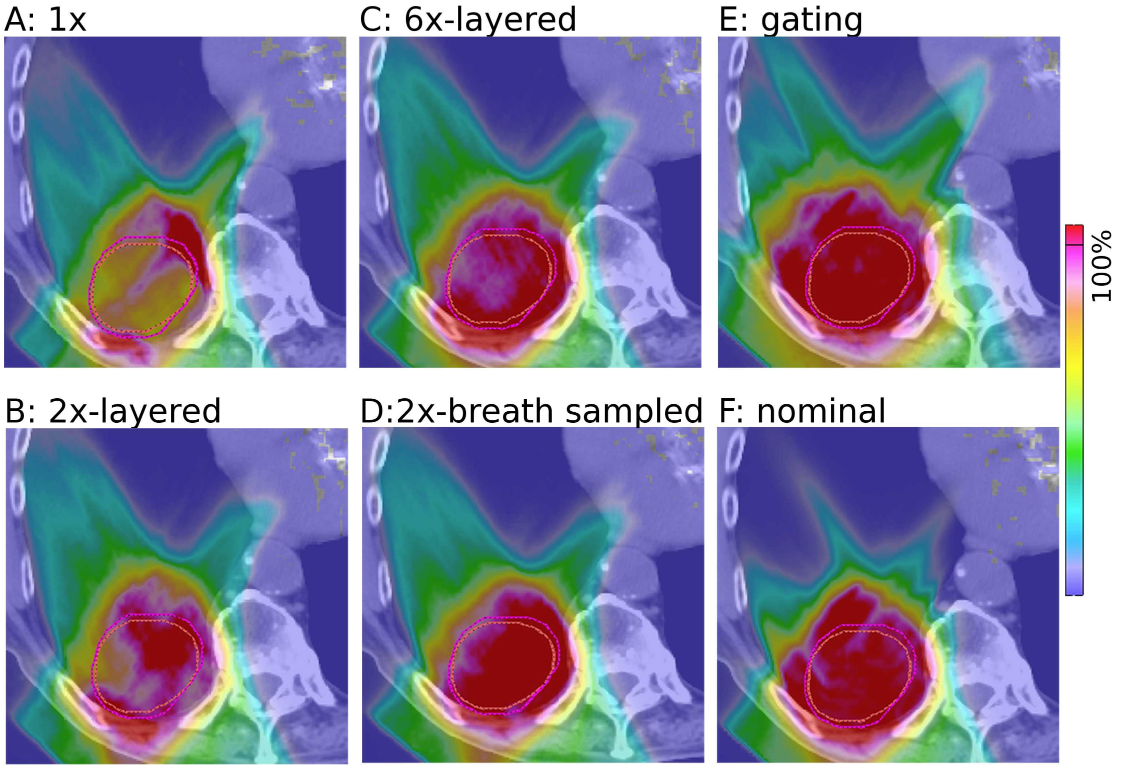

Figure 6.1: Example of dose distributions through the transverse slice after 4D-simulation for different motion mitigation approaches: (A) no motion mitigation, (B) 2x-layered rescanning, (C) 6x-layered rescanning, (D) 2x breath-sampled rescanning and gating (E). (F) shows the nominal, i.e. expected, distribution without any motion, simulated on the planning CT. The color bar is in percent of prescribed dose, the contours represent the GTV (orange) and the CTV (magenta).

Based on motion monitoring data the treatment delivery is restricted to certain parts of the breathing cycle. Usually the breathing phases around end-exhale (T50) are chosen, as they tend to be more reproducible [5].

Gating reduces the size of the target volume compared to rescanning, as only the phases within the treatment window will be used to delineate the target. This leads generally to less irradiation of normal tissue, while the treatment time increases based on the gating window.

Comparing to rescanning gating is technically more challenging, as additional hardware has to be implemented into the beam control system.

The main difficulty with gating is the robustness of the motion signal and its correlation to tumor motion, which depends heavily on the motion monitoring system [45], and irregular motion.

We have used a 30% duty cycle in our studies, using only the T40-T50-T60 phases to deliver the treatment. The treatments have been re-planned to take into account the reduced motion of the tumor in these phases. Figure 6.1E demonstrates the effect of gating, bringing the non-mitigated dose distribution (figure 6.1A) closer to the nominal one (figure 6.1E).

6.2 Results

6.2.1 Effect of Motion Mitigation in Tumor

Figure 6.2 shows the impact of the analyzed motion mitigation techniques on the interplay effect in the target of an example patient: top shows EUD, middle D_{99} and D_{5-95} at the bottom. The large beam size is given in blue, the smaller one in red. The values plotted for rescanning are the averages for the 4 initial breathing phases that were simulated, with the error bars marking the standard deviation. The triangles represent volumetric rescanning, squares volumetric rescanning. Further on the right the full circles give the values for 2x and 4x breath-sampled rescanning (BSR in the figure), the diamonds for gating and the stars for the nominal plan simulated without motion. The values in the EUD and D_{99} graphs are percentages of the static case, to avoid any bias due to differences in plan quality.

Volumetric and layered rescanning mitigate motion equally well in the patient shown in figure 6.2. 2x rescanning is sufficient in this patient for the large spot size, while 6x are necessary for the smaller spot. For more than 6 repaintings the EUD becomes higher than the nominal value, which has been observed by other authors for liver cases as well [69]. The reason for this is that the interplay effect together with rescanning can average out hot- and cold-spots that were present in the static dose distribution, making the dose distribution *more* homogenous.

Breath-sampling the timing of the rescanning proves to be a factor ≈2 more efficient than consecutive rescanning in this patient, as demonstrated by figure 6.2.

Table 6.2 shows the results for the EUD for all patients using the big spot size (top) and the small spot size (bottom). The bold numbers indicate that the EUD is within 2% of the planned value for the lowest number of repaintings, meaning that the interplay effect was successfully mitigated by the respective method.

The dose distribution for Patient 1, which shows the largest tumor motion amplitude (30.6mm), is only successfully restored by using gating and a large spot size. Even for a large number of rescans the EUD plateaus for BigSpots at ≈95%, for SmallSpots just below ≈90%. For the small spot size, the residual motion during the gating window is apparently large enough to reduce the EUD to 93.1% of the planned value.

For all other patients, table 6.2 shows that 2x rescanning is sufficient to restore the dose for the large spot size, even for motion of ≈20mm. For SmallSpots on the other hand, up to six repaintings are necessary to achieve an EUD $>$98% of the prescribed plan. If the rescannings are evenly sampled across the breathing period, 2 scannings are adequate. Gating succeeds in giving a uniform dose distribution for all patients except for the largest motion amplitude and small spot size (patient 1).

In three out of the five patients studied the efficacy of rescanning is compromised by a synchronization effect, which occurs if the total time to scan the tumor is close to an integer multiple of the breathing period. As the total dose deposited per painting changes with the number of rescannings and influences the total time to scan, this effect usually surfaces only for a specific number of rescannings. Figure

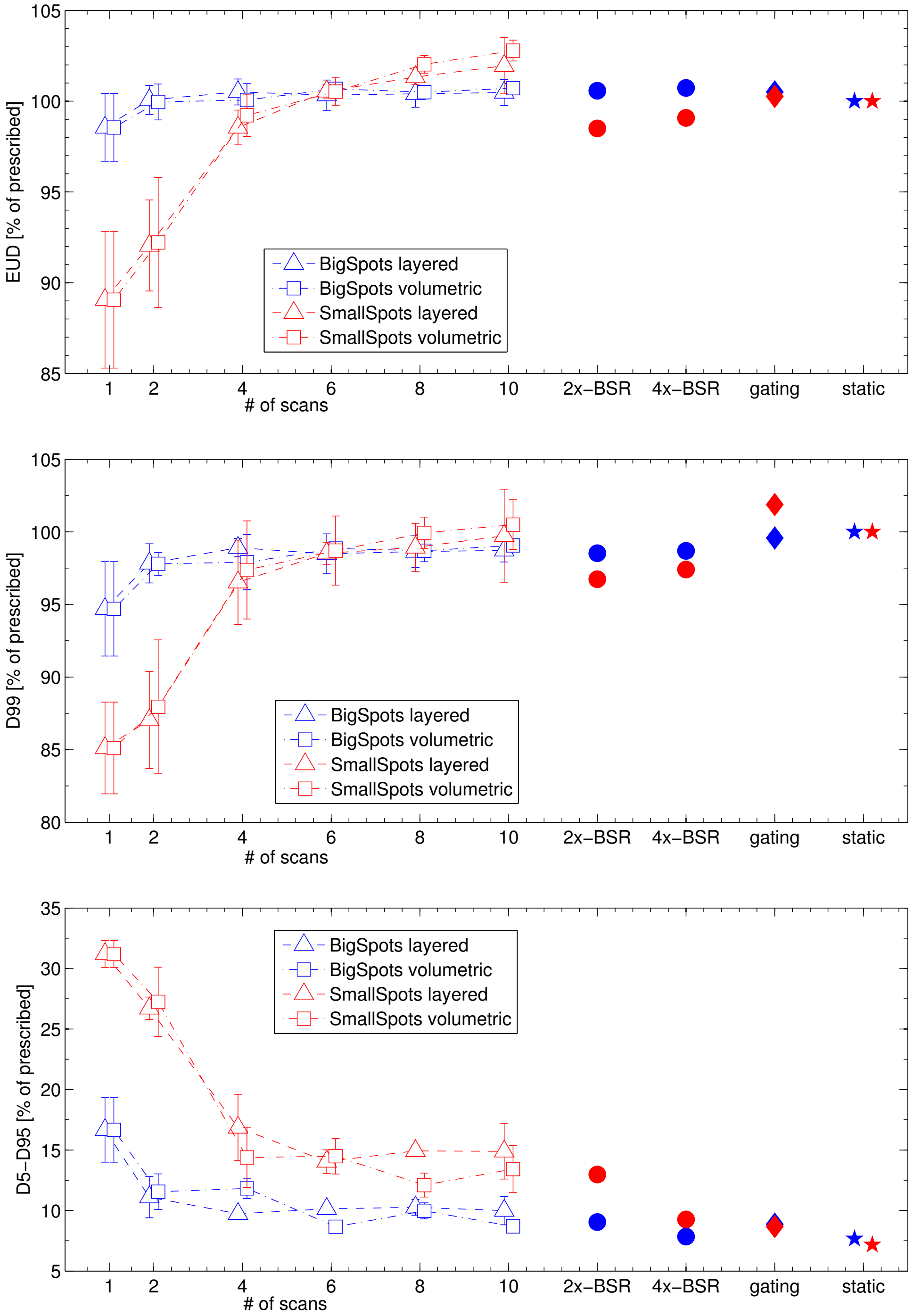

Figure 6.2: Results for patient 3: EUD (top), D_{99} (middle) and D_{5-95} (bottom). Triangles denote layered rescanning, squares volumetric rescanning, circles breath-sampled rescanning (BSR) and diamonds gating. The values for EUD and D99 are relative to the static dose distribution. Error bars represent the standard deviation from the 4 starting phases studied for each rescanning setting. Layered and volumetric symbols have been slightly offset to ease differentiation.

6.3 demonstrates this effect: for 4 consecutive rescannings with the small spot size the EUD is significantly reduced, almost to the level of no motion mitigation at all. This synchronization effect has been observed only for volumetric rescanning, while layered rescanning has not been affected.

6.2.2 Effect of Motion Mitigation in Lung Tissue

The effect of motion mitigation on the dose to the normal lung depends heavily on the quantity to be analyzed. Rescanning has almost no effect on the V20 and the mean lung dose: The V20 changes on average $<0.4\%$ and the mean lung dose stays within 0.3Gy(RBE) of the original values without any motion mitigation, even for 10 repaintings.

The effect on the maximum dose to the lung is however significant, and it leads to more reduction for the small spot size, as here the maximum values in the lung without motion mitigation are higher. For the large spot size 10x rescanning reduces the maximum dose to the lung on average 6.9Gy(RBE), for the small spot size 17Gy(RBE). For gating the reduction is similar, 6.8 Gy(RBE) for the large spot size and 6.9 Gy(RBE) for the small spot size.

Gating is on the other hand far more efficient in reducing the V20 and mean lung dose, as the treatment field is being reduced. For the large spot size the mean reduction in V20 and MLD is 0.9% and 0.4Gy(RBE) respectively, for the small spot size 2.8% and 4.9Gy(RBE). The exact reduction depends on the size of the tumor and the motion amplitude, the maximum reduction observed for our patient population was in patient 2, combining a large tumor (82.3cc) with significant motion (20.2mm). In this patient the mean lung dose and V20 reduced by 8.8 Gy(RBE) and 10% respectively.

6.3 Discussion

For the five patients investigated it has been demonstrated that rescanning can restore the dose distribution for motion up to $\approx$20mm. The number of required repaintings is relatively low, 2x for the large spot size and 6x for the small spot size.

Furthermore it has been shown that layered rescanning is more robust with respect to synchronization effects compared to volumetric rescanning. Each layer has a different number of spots and cumulative dose to be deposited, taking a varying amount of time to scan them, which makes synchronization of every layer with an almost constant breathing period improbable. For volumetric rescanning on the other hand only one timeframe counts, the total time to scan the target, making a synchronization more likely, as we have seen in three out of the five patients investigated. Layered rescanning has the advantage of being faster as well, depending on the exact time it takes to switch the energy layer. For systems developed with a focus on speed this can be as low as 80ms [105], though switching times above 1 second are more common in most treatment centers. This advantage of layered rescanning has recently been demonstrated for liver patients as well [8].

patient number	rescanning type	consecutive rescanning						breath-sampled rescanning		gating
		1x	2x	4x	6x	8x	10x	2x	4x	
BigSpots										
1	layered	91.2±4.6	91.9±5.5	94.2±3.2	94.6±0.5	94.7±2.7	94.5±2.1	94.9	95.3	**98.2**
	volumetric		93.9±2.7	94.8±1.8	94.9±1.5	93.4±4.4	94.8±0.5			
2	layered	97.6±3.4	**99.3±3**	100.2±1.3	100.1±0.6	100.2±0.8	100±0.5	99.9	100.2	98.5
	volumetric		**99.3±2**	100.1±0.5	99.9±0.7	100.1±0.5	100±0.2			
3	layered	**98.6±1.9**	100.1±0.8	100.5±0.7	100.3±0.8	100.4±0.7	100.5±0.7	100.6	100.7	100.5
	volumetric		100.0±1.0	100.1±0.9	100.7±0.1	100.5±0.4	100.7±0.1			
4	layered	**100.1±1.6**	101.1±0.4	101.1±0.5	101.3±0.2	101.3±0.4	101.4±0.2	101.3	101.4	99.3
	volumetric		100.9±0.3	101.3±0.1	101.3±0.1	101.3±0.3	101.1±0.5			
5	layered	**99.4±1.7**	99.9±1.1	100.0±0.6	100.1±0.2	100.2±0.1	100.2±0.2	100.2	100.3	101.3
	volumetric		99.9±0.4	100.2±0.2	100.2±0.1	100.1±0.2	100.2±0.1			
SmallSpots										
1	layered	61.1±4.9	78.4±5	84.0±4.4	86.0±1.8	86.6±2.1	87.3±1	83.1	86.8	93.1
	volumetric		69.0±7.3	78.9±5.9	82.6±5.1	78.9±4.1	87.2±0.4			
2	layered	89.2±8	96.8±1.5	97.0±2.9	**98.9±1.9**	100.2±1.3	101.3±1.4	99.1	100.5	98.8
	volumetric		97.8±0.7	92.4±5.6	**100.9±0.5**	101.1±0.6	100.9±1.1			
3	layered	89.1±3.8	92.1±2.5	**98.6±1.0**	100.5±0.4	101.3±0.4	102±1.5	98.5	99.1	100.3
	volumetric		92.2±3.6	**99.2±1.2**	100.5±0.8	102±0.5	102.8±0.6			
4	layered	93.5±3.6	**98.2±2.9**	100.2±1.5	101.5±0.9	102.1±0.9	102.8±0.3	100.4	101.7	102.6
	volumetric		96.9±1.7	**99.2±3.4**	100.0±2.1	102.5±0.5	103.1±0.5			
5	layered	94.9±1.8	97.3±1	**99.3±0.6**	99.7±0.5	100.7±0.4	101.1±0.5	99.7	100.0	98.4
	volumetric		96.3±1	**100.2±0.1**	95.7±1.6	100.7±0.5	101.6±0.2			

Table 6.2: Simulation results of all patients for the large spot size (top part) and the small spot size (bottom). All values are in percent of the prescribed EUD in the static plan.

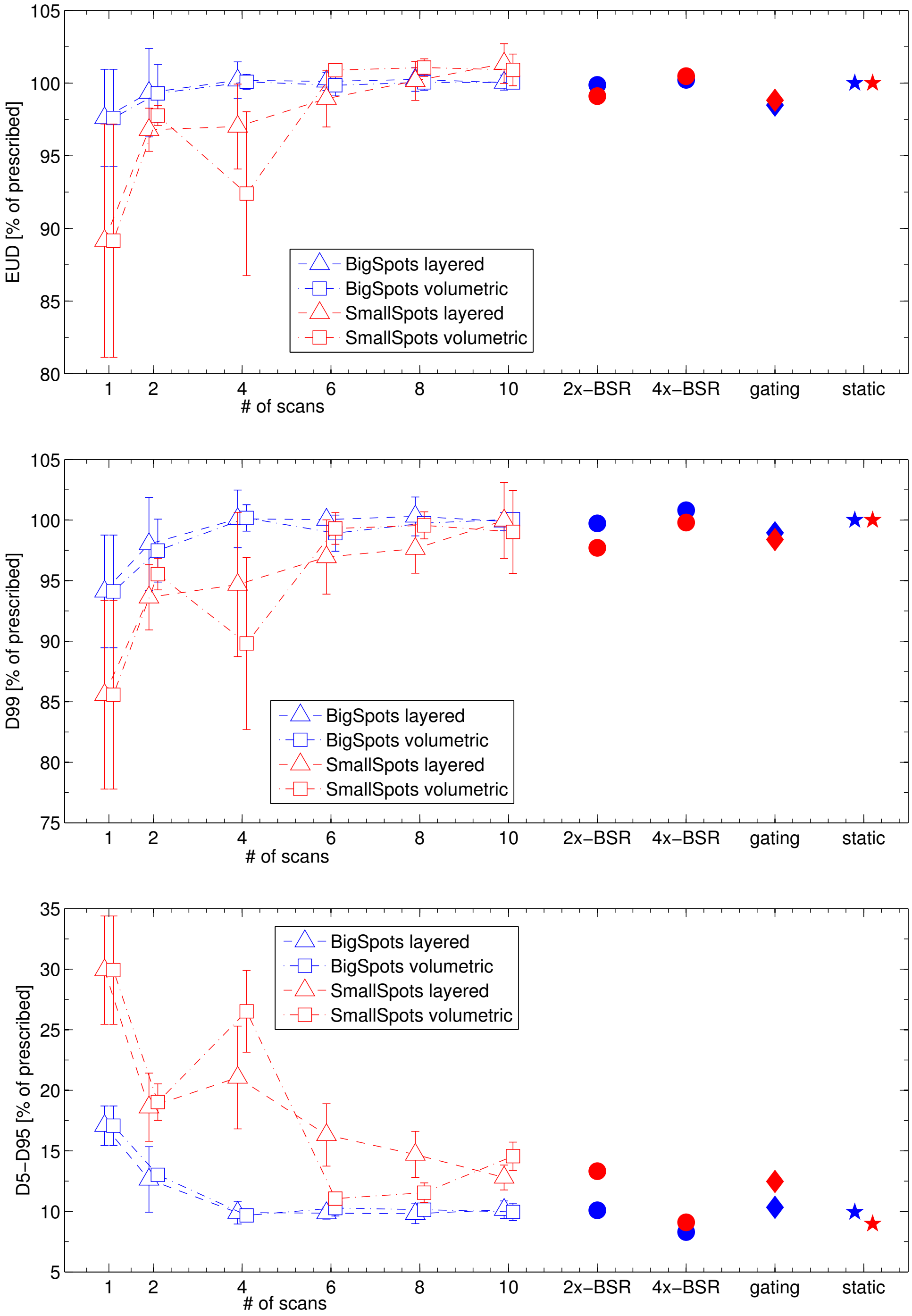

Figure 6.3: Example for synchronization effect in rescanning (patient 2), note the increase in interplay effect for 4x volumetric rescanning. EUD (top), D_{99} (middle) and D_{5-95} (bottom). Triangles denote layered rescanning, squares volumetric rescanning, circles breath-sampled rescanning (BSR) and diamonds gating. The values for EUD and D99 are relative to the static dose distribution. Error bars represent the standard deviation from the 4 starting phases studied for each rescanning setting. Layered and volumetric symbols have been slightly offset to ease differentiation.

Breath-sampling the timing of volumetric rescans has been shown to be highly effective in overcoming the synchronization effect and is rendering rescanning more effective. As can be seen in table 6.2, 2 volumetric repaintings starting half a breathing period apart are as efficient as 4-6 consecutive rescans, depending on the patient. If breath-sampling would make sense for layered rescanning is doubtful. On one hand the time needed would go up significantly, as dead times to wait for the correct breathing phase would have to be introduced at every single layer. On the other the synchronization effect does not affect layered rescanning as much as the volumetric variant, removing the other motivation for breath-sampling.

Other rescanning methods that have not been investigated here include randomizing the order of layers to be scanned, introducing random waiting times [120] and varying the scan paths of repaintings, either in 2 or even 3 dimensions [113].

What has not been investigated here is the dependence on the plan quality or number and incident angles of the beams, as we used always the same plans consisting of 2 fields. Knopf *et al* [69] have shown that more fields per plan have an averaging effect similar to rescanning.

We have planned according to a method which prescribes the dose to the envelope of target motion, which is then filled with tumor equivalent density to retain coverage in every phase. Other authors [68] use instead a range-adjusted ITV, which also includes the variations present in the entrance region of the beam. Even though the results suggest that the method used is also an adequate margin definition, it can not be excluded that using the latter methodology could have an impact in individual cases.

Furthermore the results have shown that gating with a 30% duty cycle is valid option for movement amplitudes up to 20mm in the patients studied. For the largest motion amplitude gating can only restore the EUD to >98% of the prescribed value for the large spot size. For the small spot size the residual motion in the gating window is apparently still significant, which would warrant further countermeasures. Restriction of the gating window is possible, but in this case time delays [82] and the performance of the motion monitoring itself becomes critical, requiring accuracy on the order of ≈1mm [113]. Another option would be to combine gating with rescanning, which would lead to further lengthening of the treatment time [44].

Regarding dose to normal tissue, rescanning is more effective in reducing maximum doses to the lung (or other tissues located distal to the target) while gating can significantly reduce the V20 and mean lung dose through the reduction of the treatment field. As the latter quantities are more suitable proxies to estimate the incidence of severe lung complications such as radiation pneumonitis [83], gating is superior to rescanning regarding lung side effects. The exception might be cases in which critical structures sensitive to the maximum dose, such as spinal cord and to some extent the heart, are located behind the distal edge of the beam. In this case rescanning could be necessary to reduce the impact of hotspots, possibly in addition to gating.

Tracking the target is another technique proposed for motion compensation, as it would combine the reduced normal tissue irradiation of gating with higher efficiency in beam utilization [51, 139]. Even though experimental tests in phantoms successfully mitigated interplay effects, the implementation for patient treatments has proved difficult. Online volumetric imaging of the patient would be the optimal solution, as we need not only the target motion but the complete geometry proximal to the target to be able to identify range changes. As this is not achievable at the moment, range compensation for every pencil beam spot would have to be pre-calculated for all motion states based on a pre-treatment 4D-CT scan. This however neglects irregular motion, inter- and intra-fractional changes and motion states outside the spectrum acquired by the 4D-CT [129]. This problem can be circumvented by building patient-specific motion models from extended image acquisitions beforehand and then reconstruct the motion using for example beams eye view imaging acquired during treatment [150].

6.4 Conclusion

We studied volumetric, layered and breath-sampled volumetric rescanning together with gating to mitigate the interplay effect from active scanning protons treatments in five patients. The following conclusions can be drawn from the results:

i. For motion amplitudes up to 20mm in out patient population, 2x-rescanning restores the dose distribution for a spot size σ of 8-17mm and 6x for a σ of 2-4mm.

ii. Layered rescanning proves to be more robust than volumetric rescanning in the mitigation of interplay. Three out of five patients show a synchronization effect for volumetric rescanning, reducing the effectiveness of volumetric rescanning significantly.

iii. Rescanning has no effect on the normal lung V20 or mean lung dose, independent of spot size and rescanning method. Maximum dose to the lung, however, is significantly reduced through rescanning.

iv. For the largest motion amplitude of 30mm, only gating in combination with a large spot size were able to mitigate motion effects.

v. Gating leads to a significant reduction of the dose to the normal lung only for the small spot size, -2.8% in V20 and -4.9Gy(RBE) in MLD *on average* over all patients.

Chapter 7

Conclusion and Outlook

Contents

7.1 **Experimental Validation and Implementation of Monte Carlo simulations** **79**
7.1.1 Clinical Impact 80
7.2 **Interplay Effect in Patients and Countermeasures** **80**
7.2.1 Clinical Impact 81
7.3 **Outlook** **81**
7.3.1 Monte Carlo Methods in a Clinical Environment 81
7.3.2 Treatment of Moving Targets 82

This last chapter will give a short summary of the main conclusions and the clinical impact for each part of this work, followed by future developments that are expected to move the field forward.

7.1 Experimental Validation and Implementation of Monte Carlo simulations

In the first part (chapter 3) the adequacy of the Monte Carlo code was assessed by comparing it to the clinical dose calculation algorithm and experiments in a static lung phantom. It has been shown that the use of Monte Carlo methods in the clinic could reduce the range margins that have to be applied for dose calculation uncertainty in complex geometries from 4.6% to 2.4%. In the subsequent study of a patient cohort Monte Carlo generally estimates a *lower* dose to the tumor, especially for small targets (up to 5.4% in average dose and 7.6% in minimum dose), and a *higher* dose to the surrounding lung, which was both confirmed in the experiments. The measurements in a lung phantom showed that the average difference to the Monte Carlo predictions in the target was 1.6%, while 5.6% for the clinical algorithm.

After demonstrating the benefits of Monte Carlo simulations in patients, the implementation for active scanning is presented in chapter 4. The results show that for calculation of the high-dose region in proximity of the treatment field, it is valid to approximate the pencil beams in a phase space approach at the surface of the patient. For secondary cancer estimation in the low-dose penumbra ($<$1% of maximum dose) this method is not valid, as it underestimates the out-of-field dose due to scatter in the ionization chambers.

Furthermore the energy spread to be used in the MC simulations is derived from the shape of measured depth dose distributions with the help of an analytical model (introduced in chapter 2.1.4), reproducing measurements in water to within 0.5mm.

7.1.1 Clinical Impact

Verification of patient treatments with Monte Carlo methods and the inherent reduction in range uncertainty could give the treatment planners more flexibility to chose beam angles in their design of an optimal treatment plan. The general reduction in dose to normal tissues could potentially benefit all patients, though lung cancer patients would benefit disproportionately due to the large extent of range margins in low-density lung tissue. The ≈2% margin reduction enabled by Monte Carlo could reduce the range margin in lung by ≈15mm for a proton beam of 20cm range, therefore reducing normal tissue irradiation significantly.

The increased dose calculation accuracy, in the target as well as for the healthy lung surrounding it, would increase the accuracy with which we can relate dose and effect, which is especially important for clinical trials comparing proton therapy to other modalities.

The insight that phase space based Monte Carlo simulations are accurate enough for in-field predictions of active scanning is especially important for the clinical implementation of such methods. GPU codes under development have shown promising results in terms of speed [63] and are far easier to implement for phase space based approaches.

7.2 Interplay Effect in Patients and Countermeasures

Subsequently the complexity has been increased by including the time-dependency of the patient's respiratory motion into the simulations. Chapter 5 describes the results for 10 clinical lung cancer patients for two pencil beam sizes employed by different institutions (SmallSpots = PSI, BigSpots = MGH), highlighting the important role the size of the beam has for the interplay effect. While the large beam shows almost no interplay effect up to motions of 20mm, the small spot size leads to an average loss in tumor control of 18.5% over all patients. Also the loss in dose homogeneity within the target is on average a factor 2.8 higher for the small beam. Additionally it is shown that tumor motion amplitude is not an ideal predictor for the severity of the effect in patients, contradicting studies in moving phantoms.

By using a number of conservative assumptions (the *n-fraction approximation*, see chapter 5.2.4) the mitigating effect of fractionation is analyzed, showing the effectiveness of this phenomenon to reduce the dose inhomogeneity in the target. For most patients fractionation kept tumor control within 1% of the planned value, only for the largest motion and small spot size tumor control fell by >15%.

As the trend in the treatment of lung cancer moves towards regimen employing fewer fractions (see chapter 1.2), methods to mitigate the interplay effect in a single fraction are investigated thereafter. Chapter 6 analyzes the efficiency of rescanning and gating in restoring the dose distribution in the patient.

The most important result is the robustness of layered compared to volumetric rescanning for patient cases, as the latter is often subjected to synchronization effects reducing its effectiveness. Surprisingly few rescannings are necessary to return the equivalent uniform dose to within 2% of its planned value: two for the large spot size and six for the small one are sufficient for the patients studied with motion up to 20mm. For the largest motion amplitude studied only gating in combination with a large spot size was able to mitigate the interplay effect, emphasizing the influence of residual motion during the gating window.

7.2.1 Clinical Impact

The important influence of the beam size on the interplay effect highlights the trade-off between robustness and dose conformity that can be exploited in the treatment of moving tumors. As it is relatively straightforward to increase the beam's size, variable beam sizes might be investigated to take advantage of this fact.

The superiority of layered rescanning shows that technical developments in this field should focus on in-plane beam speed and beam current more than the time to switch the energy. If slow scanning speeds make the clinical application of rescanning impractical, our results show that timing of rescanning with regard to the patient's breathing phase can increase its efficiency more than twofold.

Finally the failure of rescanning and gating for very large motion amplitudes treated with very small beams highlights the importance to combine different motion mitigation techniques, such as rescanning and gating or rescanning and tracking (termed retracking [139]).

7.3 Outlook

7.3.1 Monte Carlo Methods in a Clinical Environment

Fast GPU codes that would enable Monte Carlo based treatment planning are already under development [63] and will hopefully bring the Monte Carlo method into the proton clinic in the near future. The main uncertainty in Monte Carlo simulations remains the imperfect estimation of mean excitation energy I of patient tissues, which can possibly be reduced by employing dual-energy CT [146].

Further development of *in-vivo* verification of the dose to the patient, for example by positron emission tomography or prompt gamma imaging, offers the prospect of further understanding and reducing the uncertainties of Monte Carlo dose calculation in the patient.

7.3.2 Treatment of Moving Targets

4D treatment planning, taking into account all motion states of the moving CT, is being intensely investigated. Its main drawback is currently the reliance on specific motion from a single 4DCT, while a tumors exact motion trajectory and extent can vary from day to day. Robustness therefore needs to play a significant role in the development of these techniques. Beam angle optimization is another topic that might influence the magnitude of the interplay effect in moving targets.

The development of 4D treatment planning is closely tied to advances in image guidance for proton therapy, as the exact volumetric knowledge of patient anatomy would enable the reduction of the inherent uncertainties and robustness requirements. Proton therapy for lung cancer would profit immensely from in-room imaging, be it cone beam CT or even MRI, as the high sensitivity to changes in anatomy would also enable adaption over the course of the treatment.

Bibliography

[1] International Commission on Radiation Units and Measurements Report 49: Stopping Powers and Ranges for Protons and Alpha Particles. Journal of the ICRU 1993; Bethesda, MD. Technical report. (Cited on pages 18 and 42.)

[2] International Commission on Radiation Units and Measurements Report 78: Prescribing, recording, and reporting proton-beam therapy. Journal of the ICRU 2007; Bethesda, MD. Technical report. (Cited on pages 2 and 4.)

[3] S. Agostinelli, J. Allison, K. e. Amako, J. Apostolakis, H. Araujo, P. Arce, M. Asai, D. Axen, S. Banerjee, and G. Barrand. GEANT4—a simulation toolkit. *Nuclear instruments and methods in physics research section A: Accelerators, Spectrometers, Detectors and Associated Equipment*, 506(3):250–303, 2003. (Cited on page 18.)

[4] F. Albertini, M. Casiraghi, S. Lorentini, B. Rombi, and A. J. Lomax. Experimental verification of IMPT treatment plans in an anthropomorphic phantom in the presence of delivery uncertainties. *Physics in Medicine and Biology*, 56(14):4415–4431, July 2011. (Cited on page 39.)

[5] J. M. Balter, K. L. Lam, C. J. McGinn, T. S. Lawrence, and R. K. Ten Haken. Improvement of CT-based treatment-planning models of abdominal targets using static exhale imaging. *International Journal of Radiation Oncology*Biology*Physics*, 41(4):939–943, July 1998. (Cited on page 70.)

[6] E. A. Barnes, B. R. Murray, D. M. Robinson, L. J. Underwood, J. Hanson, and W. H. Roa. Dosimetric evaluation of lung tumor immobilization using breath hold at deep inspiration. *International Journal of Radiation Oncology* Biology* Physics*, 50(4):1091–1098, July 2001. (Cited on page 53.)

[7] M. J. Berger. Penetration of Proton Beams through Water. *NIST publications*, 1993. (Cited on pages 13 and 42.)

[8] K. Bernatowicz, A. J. Lomax, and A. Knopf. Comparative study of layered and volumetric rescanning for different scanning speeds of proton beam in liver patients. *Physics in Medicine and Biology*, 58(22):7905–7920, Oct. 2013. (Cited on page 73.)

[9] C. Bert and M. DURANTE. Motion in radiotherapy: particle therapy. *Physics in Medicine and Biology*, 56(16):R113–44, Aug. 2011. (Cited on page 8.)

[10] C. Bert, S. O. Grozinger, and E. Rietzel. Quantification of interplay effects of scanned particle beams and moving targets. *Physics in Medicine and Biology*, 53(9):2253–2265, May 2008. (Cited on pages 51 and 64.)

[11] A. Besemer, H. Paganetti, and B. Bednarz. The clinical impact of uncertainties in the mean excitation energy of human tissues during proton therapy. *Physics in Medicine and Biology*, 58(4):887–902, Feb. 2013. (Cited on page 42.)

[12] H. Bethe. Moliere's theory of multiple scattering. *Physical Review*, 89(6):1256–1266, 1953. (Cited on page 14.)

[13] H. Bethe and W. Heitler. On the stopping of fast particles and on the creation of positive electrons. In *Proceedings of the Royal Society of London Series A*, 1934. (Cited on page 12.)

[14] T. Bortfeld. An analytical approximation of the Bragg curve for therapeutic proton beams. *Medical Physics*, 24(12):2024–2033, Dec. 1997. (Cited on pages 15 and 16.)

[15] T. Bortfeld and W. Schlegel. An analytical approximation of depth-dose distributions for therapeutic proton beams. *Physics in Medicine and Biology*, 41(8):1331–1339, Aug. 1996. (Cited on page 16.)

[16] J. Bradley, J. Moughan, M. Graham, R. Byhardt, R. Govindan, J. Fowler, J. Purdy, J. Michalski, E. Gore, and H. Choy. A phase I/II radiation dose escalation study with concurrent chemotherapy for patients with inoperable stages I to III non-small-cell lung cancer: phase I results of RTOG 0117. *International Journal of Radiation Oncology* Biology* Physics*, 77(2):367–372, 2010. (Cited on page 6.)

[17] K. R. Britton, G. Starkschall, S. L. Tucker, T. Pan, C. Nelson, J. Y. Chang, J. D. Cox, R. Mohan, and R. Komaki. Assessment of gross tumor volume regression and motion changes during radiotherapy for non-small-cell lung cancer as measured by four-dimensional computed tomography. *International Journal of Radiation Oncology* Biology* Physics*, 68(4):1036–1046, July 2007. (Cited on page 53.)

[18] L. G. Brown. A survey of image registration techniques. *ACM Computing Surveys*, 24(4):325–376, Dec. 1992. (Cited on pages 23 and 24.)

[19] R. H. Byrd, P. Lu, J. Nocedal, and C. Zhu. A Limited Memory Algorithm for Bound Constrained Optimization. *SIAM Journal on Scientific Computing*, 16(5):1190–1208, Sept. 1995. (Cited on page 25.)

[20] A. K. Carlsson, P. Andreo, and A. Brahme. Monte Carlo and analytical calculation of proton pencil beams for computerized treatment plan optimization. *Physics in Medicine and Biology*, 42(6):1033–1053, June 1997. (Cited on page 38.)

[21] E. Cascio, J. Sisterson, B. Gottschalk, and S. Sarkar. Measurements of the energy spectrum of degraded proton beams at NPTC. *Radiation Effects Data Workshop, 2004 IEEE*, pages 151–155, 2004. (Cited on page 49.)

[22] J. Chang. Cancer of the Lung. *Technical Basis of Radiation Therapy*, pages 755–775, 2012. (Cited on page 6.)

[23] J. Y. Chang, R. Komaki, H. Y. Wen, B. De Gracia, J. B. Bluett, M. F. McAleer, S. G. Swisher, M. Gillin, R. Mohan, and J. D. Cox. Toxicity and patterns of failure of adaptive/ablative proton therapy for early-stage, medically inoperable non-small cell lung cancer. *International Journal of Radiation Oncology* Biology* Physics*, 80(5):1350–1357, Aug. 2011. (Cited on page 55.)

[24] Q.-S. Chen, M. S. Weinhous, F. C. Deibel, J. P. Ciezki, and R. M. Macklis. Fluoroscopic study of tumor motion due to breathing: Facilitating precise radiation therapy for lung cancer patients. *Medical Physics*, 28(9):1850–1856, 2001. (Cited on page 53.)

[25] W. Chen, J. Unkelbach, A. Trofimov, T. Madden, H. Kooy, T. Bortfeld, and D. Craft. Including robustness in multi-criteria optimization for intensity-modulated proton therapy. *Physics in Medicine and Biology*, 57(3):591–608, Feb. 2012. (Cited on page 49.)

[26] I. J. Chetty, B. Curran, J. E. Cygler, J. J. DeMarco, G. Ezzell, B. A. Faddegon, I. Kawrakow, P. J. Keall, H. Liu, C. M. C. Ma, D. W. O. Rogers, J. Seuntjens, D. Sheikh-Bagheri, and J. V. Siebers. Report of the AAPM Task Group No. 105:

Issues associated with clinical implementation of Monte Carlo-based photon and electron external beam treatment planning. *Medical Physics*, 34(12):4818, 2007. (Cited on page 29.)

[27] B. Clasie, N. Depauw, M. Fransen, C. Gomà, H. R. Panahandeh, J. Seco, J. B. Flanz, and H. M. Kooy. Golden beam data for proton pencil-beam scanning. *Physics in Medicine and Biology*, 57(5):1147–1158, Mar. 2012. (Cited on pages 16, 46, 49 and 50.)

[28] D. Craft, T. Halabi, and T. Bortfeld. Exploration of tradeoffs in intensity-modulated radiotherapy. *Physics in Medicine and Biology*, 50(24):5857–5868, Dec. 2005. (Cited on page 20.)

[29] W. J. Curran, R. Paulus, C. J. Langer, R. Komaki, J. S. Lee, S. Hauser, B. Movsas, T. Wasserman, S. A. Rosenthal, E. Gore, M. Machtay, W. Sause, and J. D. Cox. Sequential vs. concurrent chemoradiation for stage III non-small cell lung cancer: randomized phase III trial RTOG 9410. *JNCI Journal of the National Cancer Institute*, 103(19):1452–1460, Oct. 2011. (Cited on page 6.)

[30] J. Daartz, M. Engelsman, H. Paganetti, and M. R. Bussière. Field size dependence of the output factor in passively scattered proton therapy: influence of range, modulation, air gap, and machine settings. *Medical Physics*, 36(7):3205–3210, July 2009. (Cited on page 36.)

[31] A. K. Das, M. H. Bell, C. S. Nirodi, M. D. Story, and J. D. Minna. Radiogenomics predicting tumor responses to radiotherapy in lung cancer. *Seminars in radiation oncology*, 20(3):149–155, July 2010. (Cited on page 37.)

[32] N. Depauw and J. Seco. Sensitivity study of proton radiography and comparison with kV and MV x-ray imaging using GEANT4 Monte Carlo simulations. *Physics in Medicine and Biology*, 56(8):2407–2421, Mar. 2011. (Cited on page 49.)

[33] S. Dowdell, C. Grassberger, G. C. Sharp, and H. Paganetti. Interplay effects in proton scanning for lung: a 4D Monte Carlo study assessing the impact of tumor and beam delivery parameters. *Physics in Medicine and Biology*, 58(12):4137–4156, June 2013. (Cited on page 68.)

[34] S. J. Dowdell, B. Clasie, N. Depauw, P. Metcalfe, A. B. Rosenfeld, H. M. Kooy, J. B. Flanz, and H. Paganetti. Monte Carlo study of the potential reduction in out-of-field dose using a patient-specific aperture in pencil beam scanning proton therapy. *Physics in Medicine and Biology*, 57(10):2829–2842, May 2012. (Cited on page 49.)

[35] Y. Egashira, T. Nishio, T. Matsuura, S. Kameoka, and M. Uesaka. Experimental evaluation of a spatial resampling technique to improve the accuracy of pencil-beam dose calculation in proton therapy. *Medical Physics*, 39(7):4104–4114, July 2012. (Cited on page 38.)

[36] L. Ekberg, O. Holmberg, L. Wittgren, G. Bjelkengren, and T. Landberg. What margins should be added to the clinical target volume in radiotherapy treatment planning for lung cancer? *Radiotherapy and oncology: journal of the European Society for Therapeutic Radiology and Oncology*, 48(1):71–77, July 1998. (Cited on page 53.)

[37] M. Engelsman, E. Rietzel, and H. M. Kooy. Four-dimensional proton treatment planning for lung tumors. *Int J Radiat Oncol Biol Phys*, 64(5):1589–1595, Apr. 2006. (Cited on page 31.)

[38] S. C. Erridge, Y. Seppenwoolde, S. H. Muller, M. van Herk, K. De Jaeger, J. S. A. Belderbos, L. J. Boersma, and J. V. Lebesque. Portal imaging to assess set-up errors, tumor motion and tumor shrinkage during conformal radiotherapy of non-small cell lung cancer. *Radiotherapy and oncology: journal of the European Society for Therapeutic Radiology and Oncology*, 66(1):75–85, Jan. 2003. (Cited on page 53.)

[39] R. D. Evans. *The atomic nucleus*. International series in pure and applied physics. McGraw-Hill, New York, NY, 1955. (Cited on page 16.)

[40] U. Fano. Inelastic collisions and the Molière theory of multiple scattering. *Phys. Rev.*, 93(1):117–120, 1954. (Cited on page 14.)

[41] J. Ferlay, D. M. Parkin, and E. Steliarova-Foucher. Estimates of cancer incidence and mortality in Europe in 2008. *European journal of cancer (Oxford, England : 1990)*, 46(4):765–781, Mar. 2010. (Cited on page 6.)

[42] G. Folger, V. N. Ivanchenko, and J. P. Wellisch. The Binary Cascade. *The European Physical Journal A*, 21(3):407–417, Sept. 2004. (Cited on page 19.)

[43] P. Fournel. RTOG 94-10: Keenly Awaited Results Validating the Best Therapeutic Strategy for Locally Advanced Non-Small Cell Lung Cancer. *JNCI Journal of the National Cancer Institute*, 103(19):1425–1427, Oct. 2011. (Cited on page 6.)

[44] T. Furukawa, T. Inaniwa, S. Sato, T. Shirai, S. Mori, E. Takeshita, K. Mizushima, T. Himukai, and K. Noda. Moving target irradiation with fast rescanning and gating in particle therapy. *Medical Physics*, 37(9):4874, 2010. (Cited on page 76.)

[45] D. P. Gierga, J. Brewer, G. C. Sharp, and M. Betke. The correlation between internal and external markers for abdominal tumors: Implications for respiratory gating. *International Journal of Radiation Oncology* Biology* Physics*, 2005. (Cited on page 70.)

[46] S. Girdhani, R. Sachs, and L. Hlatky. Biological Effects of Proton Radiation: What We Know and Don't Know. *Radiation Research*, 179(3):257–272, Mar. 2013. (Cited on page 5.)

[47] M. Goitein. *Radiation Oncology: A Physicist's-Eye View*. Springer, Nov. 2010. (Cited on pages 11, 13 and 15.)

[48] B. Gottschalk, A. M. Koehler, R. J. Schneider, J. M. Sisterson, and M. S. Wagner. Multiple Coulomb scattering of 160 MeV protons. *Nuclear Instruments and Methods in Physics Research Section B*, 74(4):467–490, June 1993. (Cited on pages 14 and 21.)

[49] C. Grassberger, S. Dowdell, A. Lomax, G. Sharp, J. Shackleford, N. Choi, H. Willers, and H. Paganetti. Motion Interplay as a Function of Patient Parameters and Spot Size in Spot Scanning Proton Therapy for Lung Cancer. *International Journal of Radiation Oncology*Biology*Physics*, 86(2):380–386, June 2013. (Cited on page 51.)

[50] C. Grassberger and H. Paganetti. Elevated LET components in clinical proton beams. *Physics in Medicine and Biology*, 56(20):6677–6691, Sept. 2011. (Cited on page 16.)

[51] S. O. Grozinger, C. Bert, T. Haberer, G. Kraft, and E. Rietzel. Motion compensation with a scanned ion beam: a technical feasibility study. *Radiation Oncology*, 3(1):34, 2008. (Cited on page 77.)

[52] M. Guckenberger, T. Krieger, A. Richter, K. Baier, J. Wilbert, R. A. Sweeney, and M. Flentje. Potential of image-guidance, gating and real-time tracking to improve accuracy in pulmonary stereotactic body radiotherapy. *Radiotherapy and oncology: journal of the European Society for Therapeutic Radiology and Oncology*, 91(3):288–295, June 2009. (Cited on page 53.)

[53] M. Guckenberger, J. Meyer, J. Wilbert, A. Richter, K. Baier, G. Mueller, and M. Flentje. Intra-fractional uncertainties in cone-beam CT based image-guided radiotherapy (IGRT) of pulmonary tumors. *Radiotherapy and oncology: journal of the European Society for Therapeutic Radiology and Oncology*, 83(1):57–64, Apr. 2007. (Cited on page 53.)

[54] K. Hagiwara. Particle Data Group Collaboration. *Phys Rev D*, 2002. (Cited on page 19.)

[55] E. J. Hall and A. J. Giaccia. Radiobiology for the Radiologist. 2006. (Cited on pages 5 and 26.)

[56] J. Hanley, M. M. Debois, D. Mah, G. S. Mageras, A. Raben, K. ROSENZWEIG, B. Mychalczak, L. H. Schwartz, P. J. Gloeggler, W. Lutz, C. C. Ling, S. A. Leibel, Z. Fuks, and G. J. Kutcher. Deep inspiration breath-hold technique for lung tumors: the potential value of target immobilization and reduced lung density in dose escalation. *International Journal of Radiation Oncology* Biology* Physics*, 45(3):603–611, Oct. 1999. (Cited on page 53.)

[57] L. Hong, M. Goitein, M. Bucciolini, R. Comiskey, B. Gottschalk, S. Rosenthal, C. Serago, and M. Urie. A pencil beam algorithm for proton dose calculations. *Physics in Medicine and Biology*, 41(8):1305–1330, Aug. 1996. (Cited on pages 20 and 35.)

[58] Z. Hui, X. Zhang, G. Starkschall, Y. Li, R. Mohan, R. Komaki, J. D. Cox, and J. Y. Chang. Effects of interfractional motion and anatomic changes on proton therapy dose distribution in lung cancer. *International Journal of Radiation Oncology* Biology* Physics*, 72(5):1385–1395, Dec. 2008. (Cited on page 7.)

[59] V. N. Ivanchenko. Combined cross-sections and elastic scattering. In *11th Geant4 Collaboration Workshop and Users Conference, Oct. 2006*. (Cited on page 19.)

[60] J. F. Janni. Proton Range-Energy Tables, 1 keV-10 GeV, Energy Loss, Range, Path Length, Time-of-Flight, Straggling, Multiple Scattering, and Nuclear Interaction Probability. Part I. For 63 Compounds. *Atomic Data and Nuclear Data Tables*, 27:147, 1982. (Cited on pages 13, 15, 17, 42 and 45.)

[61] A. Jemal, R. Siegel, E. Ward, Y. Hao, J. Xu, T. Murray, and M. J. Thun. Cancer Statistics, 2008. *CA: A Cancer Journal for Clinicians*, 58(2):71–96, Jan. 2008. (Cited on pages v and 6.)

[62] X. Jia, X. Gu, Y. J. Graves, M. Folkerts, and S. B. Jiang. GPU-based fast Monte Carlo simulation for radiotherapy dose calculation. *Physics in Medicine and Biology*, 56(22):7017–7031, Oct. 2011. (Cited on page 38.)

[63] X. Jia, J. Schümann, H. Paganetti, and S. B. Jiang. GPU-based fast Monte Carlo dose calculation for proton therapy. *Physics in Medicine and Biology*, 57(23):7783–7797, Nov. 2012. (Cited on pages 38, 80 and 81.)

[64] J.-Y. Jin, F.-M. Kong, I. J. Chetty, M. Ajlouni, S. Ryu, R. Ten Haken, and B. Movsas. Impact of fraction size on lung radiation toxicity: hypofractionation may be beneficial in dose escalation of radiotherapy for lung cancers. *International Journal of Radiation Oncology* Biology* Physics*, 76(3):782–788, 2010. (Cited on page 67.)

[65] Y. Kang, X. Zhang, J. Y. Chang, H. Wang, X. Wei, Z. Liao, R. Komaki, J. D. Cox, P. A. Balter, H. Liu, X. R. Zhu, R. Mohan, and L. Dong. 4D Proton treatment planning strategy for mobile lung tumors. *International Journal of Radiation Oncology* Biology* Physics*, 67(3):906–914, Mar. 2007. (Cited on pages 8, 20, 31, 51 and 55.)

[66] P. Kimstrand, E. Traneus, A. Ahnesjö, E. Grusell, B. Glimelius, and N. Tilly. A beam source model for scanned proton beams. *Physics in Medicine and Biology*, 52(11):3151–3168, June 2007. (Cited on page 49.)

[67] T. Knöös, A. Ahnesjö, P. Nilsson, and L. Weber. Limitations of a pencil beam approach to photon dose calculations in lung tissue. *Physics in Medicine and Biology*, 40(9):1411–1420, Sept. 1995. (Cited on page 29.)

[68] A.-C. Knopf, D. Boye, A. Lomax, and S. Mori. Adequate margin definition for scanned particle therapy in the incidence of intrafractional motion. *Physics in Medicine and Biology*, 58(17):6079–6094, Sept. 2013. (Cited on page 76.)

[69] A.-C. Knopf, T. S. Hong, and A. Lomax. Scanned proton radiotherapy for mobile targets-the effectiveness of re-scanning in the context of different treatment planning approaches and for different motion characteristics. *Physics in Medicine and Biology*, 56(22):7257–7271, Nov. 2011. (Cited on pages 51, 61, 64, 71 and 76.)

[70] A. M. Koehler, R. J. Schneider, and J. M. Sisterson. Range modulators for protons and heavy ions. *Nuclear Instruments and Methods*, 131(3):437–440, Dec. 1975. (Cited on page 3.)

[71] A. M. Koehler, R. J. Schneider, and J. M. Sisterson. Flattening of proton dose distributions for large-field radiotherapy. *Medical Physics*, 4:297, 1977. (Cited on page 3.)

[72] H. M. Kooy, B. M. Clasie, H.-M. Lu, T. M. Madden, H. Bentefour, N. Depauw, J. A. Adams, A. V. Trofimov, D. Demaret, T. F. Delaney, and J. B. Flanz. A case study in proton pencil-beam scanning delivery. *International Journal of Radiation Oncology* Biology* Physics*, 76(2):624–630, Feb. 2010. (Cited on pages 20 and 22.)

[73] S. Korreman, G. Persson, D. Nygaard, C. Brink, and T. Juhler-Nøttrup. Respiration-correlated image guidance is the most important radiotherapy motion management strategy for most lung cancer patients. *International Journal of Radiation Oncology* Biology* Physics*, 83(4):1338–1343, July 2012. (Cited on page 53.)

[74] K. M. Kraus, E. Heath, and U. Oelfke. Dosimetric consequences of tumour motion due to respiration for a scanned proton beam. *Physics in Medicine and Biology*, 56(20):6563–6581, Sept. 2011. (Cited on pages 51 and 64.)

[75] K. M. Langen and D. T. L. Jones. Organ motion and its management. *International Journal of Radiation Oncology*Biology*Physics*, 50(1):265–278, May 2001. (Cited on page 7.)

[76] B. Larsson. Pre-therapeutic Physical Experiments with High Energy Protons. *British Journal of Radiology*, 34(399):143–151, Mar. 1961. (Cited on page 3.)

[77] Y. Li, R. X. Zhu, N. Sahoo, A. Anand, and X. Zhang. Beyond Gaussians: a study of single-spot modeling for scanning proton dose calculation. *Physics in Medicine and Biology*, 57(4):983–997, Feb. 2012. (Cited on page 38.)

[78] H. H. Liu, P. Balter, T. Tutt, B. Choi, J. Zhang, C. Wang, M. Chi, D. Luo, T. Pan, S. Hunjan, G. Starkschall, I. Rosen, K. Prado, Z. Liao, J. Chang, R. Komaki, J. D. Cox, R. Mohan, and L. Dong. Assessing respiration-induced tumor motion and internal target volume using four-dimensional computed tomography for radiotherapy of lung cancer. *International Journal of Radiation Oncology* Biology* Physics*, 68(2):531–540, June 2007. (Cited on page 53.)

[79] A. Lomax. Intensity modulated proton therapy and its sensitivity to treatment uncertainties 1: the potential effects of calculational uncertainties. *Physics in Medicine and Biology*, 53:1027, 2008. (Cited on page 39.)

[80] A. Lomax, T. Boehringer, A. Coray, E. Egger, G. Goitein, M. Grossmann, P. Juelke, S. Lin, E. Pedroni, and B. Rohrer. Intensity modulated proton therapy: a clinical example. *Medical Physics*, 28:317, 2001. (Cited on page 4.)

[81] A. J. Lomax. Intensity modulated proton therapy and its sensitivity to treatment uncertainties 2: the potential effects of inter-fraction and inter-field motions. *Physics in Medicine and Biology*, 53(4):1043–1056, Feb. 2008. (Cited on page 39.)

[82] H. M. Lu, R. Brett, G. Sharp, S. Safai, S. Jiang, and J. Flanz. Scitation: A respiratory-gated treatment system for proton therapy. *Medical Physics*, 2007. (Cited on pages 69 and 76.)

[83] L. B. Marks, S. M. Bentzen, J. O. Deasy, F.-M. S. Kong, J. D. Bradley, I. S. Vogelius, I. El Naqa, J. L. Hubbs, J. V. Lebesque, R. D. Timmerman, M. K. Martel, and A. Jackson. Radiation dose-volume effects in the lung. *International Journal of Radiation Oncology* Biology* Physics*, 76(3 Suppl):S70–6, Mar. 2010. (Cited on pages 55 and 76.)

[84] M. K. Martel, R. K. Ten Haken, M. B. Hazuka, M. L. Kessler, M. Strawderman, A. T. Turrisi, T. S. Lawrence, B. A. Fraass, and A. S. Lichter. Estimation of tumor control probability model parameters from 3-D dose distributions of non-small cell lung cancer patients. *Lung cancer (Amsterdam, Netherlands)*, 24(1):31–37, Apr. 1999. (Cited on page 27.)

[85] D. Michalski, M. Sontag, F. Li, R. S. de Andrade, I. Uslene, E. D. Brandner, D. E. Heron, N. Yue, and M. S. Huq. Four-dimensional computed tomography-based interfractional reproducibility study of lung tumor intrafractional motion. *International Journal of Radiation Oncology* Biology* Physics*, 71(3):714–724, July 2008. (Cited on page 53.)

[86] S. Minohara, T. Kanai, M. Endo, K. Noda, and M. Kanazawa. Respiratory gated irradiation system for heavy-ion radiotherapy. *International Journal of Radiation Oncology* Biology* Physics*, 47(4):1097–1103, July 2000. (Cited on page 69.)

[87] G. Moliere. Theorie der Streuung schneller geladener Teilchen I. Einzelstreuung am abgeschirmten Coulomb-Feld. *Zeitschrift Naturforschung Teil A*, 2:133, 1947. (Cited on page 13.)

[88] G. Moliere. Theorie der Streuung schneller geladener Teilchen II. Mehrfach- und Vielfachstreuung. *Zeitschrift Naturforschung Teil A*, 3:78, 1948. (Cited on pages 14 and 18.)

[89] S. Mori, M. Endo, S. Komatsu, T. Yashiro, S. Kandatsu, and M. Baba. Four-dimensional measurement of lung tumor displacement using 256-multi-slice CT-scanner. *Lung cancer (Amsterdam, Netherlands)*, 56(1):59–67, Apr. 2007. (Cited on page 53.)

[90] M. F. Moyers, G. B. Coutrakon, A. Ghebremedhin, K. Shahnazi, P. Koss, and E. Sanders. Calibration of a proton beam energy monitor. *Medical Physics*, 34(6):1952, 2007. (Cited on page 42.)

[91] R. Muirhead, L. van der Weide, J. R. van Sornsen de Koste, K. S. Cover, and S. Senan. Use of megavoltage cine-images for studying intra-thoracic motion during radiotherapy for locally advanced lung cancer. *Radiotherapy and oncology: journal of the European Society for Therapeutic Radiology and Oncology*, 99(2):155–160, May 2011. (Cited on page 53.)

[92] K. Murphy, B. van Ginneken, J. M. Reinhardt, S. Kabus, K. Ding, X. Deng, K. Cao, K. Du, G. E. Christensen, V. Garcia, T. Vercauteren, N. Ayache, O. Commowick, G. Malandain, B. Glocker, N. Paragios, N. Navab, V. Gorbunova, J. Sporring, M. de Bruijne, X. Han, M. P. Heinrich, J. A. Schnabel, M. Jenkinson, C. Lorenz, M. Modat, J. R. McClelland, S. Ourselin, S. E. A. Muenzing, M. A. Viergever, D. De Nigris, D. L. Collins, T. Arbel, M. Peroni, R. Li, G. C. Sharp, A. Schmidt-Richberg, J. Ehrhardt, R. Werner, D. Smeets, D. Loeckx, G. Song, N. Tustison, B. Avants, J. C. Gee, M. Staring, S. Klein, B. C. Stoel, M. Urschler, M. Werlberger, J. Vandemeulebroucke, S. Rit, D. Sarrut, and J. P. W. Pluim. Evaluation of registration methods on thoracic CT: the EMPIRE10 challenge. *IEEE transactions on medical imaging*, 30(11):1901–1920, Nov. 2011. (Cited on pages 24 and 58.)

[93] M. J. Murphy, D. Martin, R. Whyte, J. Hai, C. Ozhasoglu, and Q.-T. Le. The effectiveness of breath-holding to stabilize lung and pancreas tumors during radiosurgery. *International Journal of Radiation Oncology*Biology*Physics*, 53(2):475–482, June 2002. (Cited on page 53.)

[94] A. Niemierko. Reporting and analyzing dose distributions: a concept of equivalent uniform dose. *Medical Physics*, 24(1):103–110, Jan. 1997. (Cited on page 26.)

[95] K. Ohara, T. Okumura, M. Akisada, T. Inada, T. Mori, H. Yokota, and M. J. B. Calaguas. Irradiation synchronized with respiration gate. *International Journal of Radiation Oncology*Biology*Physics*, 17(4):853–857, Oct. 1989. (Cited on page 69.)

[96] C. Ong, W. F. A. R. Verbakel, J. P. Cuijpers, B. J. Slotman, and S. Senan. Dosimetric impact of interplay effect on RapidArc lung stereotactic treatment delivery. *International Journal of Radiation Oncology* Biology* Physics*, 79(1):305–311, Jan. 2011. (Cited on page 53.)

[97] H. Onishi, H. Shirato, Y. Nagata, M. Hiraoka, M. Fujino, K. Gomi, Y. Niibe, K. Karasawa, K. Hayakawa, Y. Takai, T. Kimura, A. Takeda, A. Ouchi, M. Hareyama, M. Kokubo, R. Hara, J. ITAMI, K. Yamada, and T. Araki. Hypofractionated stereotactic radiotherapy (HypoFXSRT) for stage I non-small cell lung cancer: updated results of 257 patients in a Japanese multi-institutional study. *Journal of thoracic oncology : official publication of the International Association for the Study of Lung Cancer*, 2(7 Suppl 3):S94–100, July 2007. (Cited on page 6.)

[98] S. F. C. O'Rourke, H. McAneney, and T. Hillen. Linear quadratic and tumour control probability modelling in external beam radiotherapy. *Journal of Mathematical Biology*, 58(4-5):799–817, Sept. 2008. (Cited on page 27.)

[99] H. Paganetti. Range uncertainties in proton therapy and the role of Monte Carlo simulations. *Physics in Medicine and Biology*, 57(11):R99–R117, June 2012. (Cited on pages vii, 34 and 37.)

[100] H. Paganetti, H. Jiang, K. Parodi, R. Slopsema, and M. Engelsman. Clinical implementation of full Monte Carlo dose calculation in proton beam therapy. *Physics in Medicine and Biology*, 53(17):4825–4853, Sept. 2008. (Cited on pages 19 and 46.)

[101] H. Paganetti, A. Niemierko, M. Ancukiewicz, L. E. Gerweck, M. Goitein, J. S. Loeffler, and H. D. Suit. Relative biological effectiveness (RBE) values for proton beam therapy. *International Journal of Radiation Oncology* Biology* Physics*, 53(2):407–421, June 2002. (Cited on page 5.)

[102] J. R. Pantarotto, A. H. M. Piet, A. Vincent, J. R. van Sornsen de Koste, and S. Senan. Motion analysis of 100 mediastinal lymph nodes: potential pitfalls in treatment planning and adaptive strategies. *International Journal of Radiation Oncology* Biology* Physics*, 74(4):1092–1099, July 2009. (Cited on page 53.)

[103] M. Partridge, M. Ramos, A. Sardaro, and M. Brada. Dose escalation for non-small cell lung cancer: analysis and modelling of published literature. *Radiotherapy and oncology: journal of the European Society for Therapeutic Radiology and Oncology*, 99(1):6–11, Apr. 2011. (Cited on page 67.)

[104] E. Pedroni, R. Bacher, H. Blattmann, T. Böhringer, A. Coray, A. Lomax, S. Lin, G. Munkel, S. Scheib, and U. Schneider. The 200-MeV proton therapy project at the Paul Scherrer Institute: conceptual design and practical realization. *Medical Physics*, 22:37, 1995. (Cited on page 4.)

[105] E. Pedroni, D. Meer, C. Bula, S. Safai, and S. Zenklusen. Pencil beam characteristics of the next-generation proton scanning gantry of PSI: design issues and initial commissioning results. *The European Physical Journal Plus*, 126(7):1–27, 2011. (Cited on pages 56 and 73.)

[106] E. Pedroni, S. Scheib, T. Böhringer, A. Coray, M. Grossmann, S. Lin, and A. Lomax. Experimental characterization and physical modelling of the dose distribution of scanned proton pencil beams. *Physics in Medicine and Biology*, 50(3):541–561, Jan. 2005. (Cited on page 50.)

[107] J. Perl, J. Shin, J. Schümann, B. Faddegon, and H. Paganetti. TOPAS: An innovative proton Monte Carlo platform for research and clinical applications. *Medical Physics*, 39(11):6818, 2012. (Cited on page 19.)

[108] P. L. Petti. Differential-pencil-beam dose calculations for charged particles. *Medical Physics*, 19:137, 1992. (Cited on page 35.)

[109] M. H. Phillips, E. Pedroni, H. Blattmann, T. Boehringer, A. Coray, and S. Scheib. Effects of respiratory motion on dose uniformity with a charged particle scanning method. *Physics in Medicine and Biology*, 37(1):223, 1992. (Cited on pages 8 and 69.)

[110] C. Plathow, S. Ley, C. Fink, M. Puderbach, W. Hosch, A. Schmähl, J. Debus, and H.-U. Kauczor. Analysis of intrathoracic tumor mobility during whole breathing cycle by dynamic MRI. *International Journal of Radiation Oncology* Biology* Physics*, 59(4):952–959, July 2004. (Cited on page 53.)

[111] T. G. Purdie, J.-P. Bissonnette, K. Franks, A. Bezjak, D. Payne, F. Sie, M. B. Sharpe, and D. A. Jaffray. Cone-beam computed tomography for on-line image guidance of lung stereotactic radiotherapy: localization, verification, and intrafraction tumor position. *International Journal of Radiation Oncology* Biology* Physics*, 68(1):243–252, May 2007. (Cited on page 53.)

[112] A. Richter, J. Wilbert, K. Baier, M. Flentje, and M. Guckenberger. Feasibility study for markerless tracking of lung tumors in stereotactic body radiotherapy. *International Journal of Radiation Oncology* Biology* Physics*, 78(2):618–627, Oct. 2010. (Cited on page 53.)

[113] E. Rietzel and C. Bert. Respiratory motion management in particle therapy. *Medical Physics*, 37(2):449, 2010. (Cited on pages 69 and 76.)

[114] G. O. Sawakuchi, U. Titt, D. Mirkovic, G. Ciangaru, X. R. Zhu, N. Sahoo, M. T. Gillin, and R. Mohan. Monte Carlo investigation of the low-dose envelope from scanned proton pencil beams. *Physics in Medicine and Biology*, 55(3):711–721, Jan. 2010. (Cited on pages 38 and 50.)

[115] G. O. Sawakuchi, X. R. Zhu, F. Poenisch, K. Suzuki, G. Ciangaru, U. Titt, A. Anand, R. Mohan, M. T. Gillin, and N. Sahoo. Experimental characterization of the low-dose envelope of spot scanning proton beams. *Physics in Medicine and Biology*, 55(12):3467–3478, May 2010. (Cited on pages 16 and 50.)

[116] S. E. Schild, W. L. McGinnis, D. Graham, S. Hillman, T. R. Fitch, D. Northfelt, Y. I. Garces, H. Shahidi, L. K. Tschetter, P. L. Schaefer, A. Adjei, and J. Jett. Results of a Phase I trial of concurrent chemotherapy and escalating doses of radiation for unresectable non-small-cell lung cancer. *International Journal of Radiation Oncology* Biology* Physics*, 65(4):1106–1111, July 2006. (Cited on page 6.)

[117] W. Schneider, T. Bortfeld, and W. Schlegel. Correlation between CT numbers and tissue parameters needed for Monte Carlo simulations of clinical dose distributions. *Physics in Medicine and Biology*, 45:459, 2000. (Cited on page 19.)

[118] T. E. Schultheiss. Models in radiotherapy: Definition of decision criteria. *Medical Physics*, 12(2):183–187, 1985. (Cited on page 27.)

[119] J. Schümann, H. Paganetti, J. Shin, B. Faddegon, and J. Perl. Efficient voxel navigation for proton therapy dose calculation in TOPAS and Geant4. *Physics in Medicine and Biology*, 57(11):3281–3293, June 2012. (Cited on page 19.)

[120] J. Seco, D. Robertson, A. Trofimov, and H. Paganetti. Breathing interplay effects during proton beam scanning: simulation and statistical analysis. *Physics in Medicine and Biology*, 54(14):N283–N294, June 2009. (Cited on pages 69 and 76.)

[121] S. Senthi, C. J. A. Haasbeek, B. J. Slotman, and S. Senan. Outcomes of stereotactic ablative radiotherapy for central lung tumours: A systematic review. *Radiotherapy and Oncology*, 106(3):276–282, Mar. 2013. (Cited on pages 37 and 68.)

[122] Y. Seppenwoolde, H. Shirato, K. Kitamura, S. Shimizu, M. van Herk, J. V. Lebesque, and K. Miyasaka. Precise and real-time measurement of 3D tumor motion in lung due to breathing and heartbeat, measured during radiotherapy. *International Journal of Radiation Oncology* Biology* Physics*, 53(4):822–834, July 2002. (Cited on page 53.)

[123] C. Shah, I. S. Grills, L. L. Kestin, S. McGrath, H. Ye, S. K. Martin, and D. Yan. Intrafraction Variation of Mean Tumor Position During Image-Guided Hypofractionated Stereotactic Body Radiotherapy for Lung Cancer. *International Journal of Radiation Oncology*Biology*Physics*, 82(5):1636–1641, Apr. 2012. (Cited on page 53.)

[124] G. C. Sharp, M. Peroni, R. Li, and J. Shackleford. Evaluation of plastimatch B-Spline registration on the EMPIRE10 data set. *Medical Image Analysis for the Clinic: A Grand Challenge*, pages 99–108, 2010. (Cited on page 24.)

[125] H. Shirato, K. Suzuki, G. C. Sharp, K. Fujita, R. Onimaru, M. Fujino, N. Kato, Y. Osaka, R. Kinoshita, H. Taguchi, S. Onodera, and K. Miyasaka. Speed and amplitude of lung tumor motion precisely detected in four-dimensional setup and in real-time tumor-tracking radiotherapy. *International Journal of Radiation Oncology* Biology* Physics*, 64(4):1229–1236, Mar. 2006. (Cited on page 53.)

[126] K. E. Sixel, M. Ruschin, R. Tirona, and P. C. F. Cheung. Digital fluoroscopy to quantify lung tumor motion: potential for patient-specific planning target volumes. *International Journal of Radiation Oncology* Biology* Physics*, 57(3):717–723, Nov. 2003. (Cited on page 53.)

[127] A. R. Smith. Vision 20-20: Proton therapy. *Medical Physics*, 36(2):556, 2009. (Cited on pages v and 2.)

[128] J.-J. Sonke and J. Belderbos. Adaptive radiotherapy for lung cancer. *Seminars in radiation oncology*, 20(2):94–106, Apr. 2010. (Cited on page 4.)

[129] J.-J. Sonke, J. Lebesque, and M. van Herk. Variability of four-dimensional computed tomography patient models. *International Journal of Radiation Oncology* Biology* Physics*, 70(2):590–598, Feb. 2008. (Cited on pages 53 and 77.)

[130] A. Sottoriva, J. J. C. Verhoeff, T. Borovski, S. K. McWeeney, L. Naumov, J. P. Medema, P. M. A. Sloot, and L. Vermeulen. Cancer Stem Cell Tumor Model Reveals Invasive Morphology and Increased Phenotypical Heterogeneity. *Cancer Research*, 70(1):46–56, Jan. 2010. (Cited on page 37.)

[131] G. Soza, M. Bauer, P. Hastreiter, C. Nimsky, and G. Greiner. Non-rigid Registration with Use of Hardware-Based 3D Bézier Functions. In *Medical Image Computing and Computer-Assisted Intervention—MICCAI 2002*, pages 549–556. Springer Berlin Heidelberg, Berlin, Heidelberg, Oct. 2002. (Cited on page 25.)

[132] E. Steiner, M. Stock, B. Kostresevic, A. Ableitinger, U. Jelen, H. Prokesch, A. Santiago, P. Trnková, A. Wolf, A. Wittig, A. Lomax, O. Jäkel, G. Baroni, and D. Georg. Imaging dose assessment for IGRT in particle beam therapy. *Radiotherapy and oncology: journal of the European Society for Therapeutic Radiology and Oncology*, Oct. 2013. (Cited on page 49.)

[133] C. W. Stevens, R. F. Munden, K. M. Forster, J. F. Kelly, Z. LIAO, G. Starkschall, S. Tucker, and R. Komaki. Respiratory-driven lung tumor motion is independent of tumor size, tumor location, and pulmonary function. *International Journal of Radiation Oncology* Biology* Physics*, 51(1):62–68, Sept. 2001. (Cited on page 53.)

[134] Y. Suh, S. Dieterich, B. Cho, and P. J. Keall. An analysis of thoracic and abdominal tumour motion for stereotactic body radiotherapy patients. *Physics in Medicine and Biology*, 53(13):3623–3640, July 2008. (Cited on page 53.)

[135] H. Szymanowski and U. Oelfke. Two-dimensional pencil beam scaling: an improved proton dose algorithm for heterogeneous media. *Physics in Medicine and Biology*, 47(18):3313–3330, Sept. 2002. (Cited on page 35.)

[136] R. Timmerman, R. Paulus, J. Galvin, J. Michalski, W. Straube, J. Bradley, A. Fakiris, A. Bezjak, G. Videtic, D. Johnstone, J. Fowler, E. Gore, and H. Choy. Stereotactic body radiation therapy for inoperable early stage lung cancer. *JAMA : the journal of the American Medical Association*, 303(11):1070–1076, Mar. 2010. (Cited on page 6.)

[137] W. Ulmer and B. Schaffner. Foundation of an analytical proton beamlet model for inclusion in a general proton dose calculation system. *Radiation physics and chemistry*, 80(3):378–389, 2011. (Cited on page 35.)

[138] L. Urban. A multiple scattering model in Geant4. *Preprint CERNOPEN-2006-077*, 2006. (Cited on page 18.)

[139] S. van de Water, R. Kreuger, S. Zenklusen, E. Hug, and A. J. Lomax. Tumour tracking with scanned proton beams: assessing the accuracy and practicalities. *Physics in Medicine and Biology*, 54(21):6549–6563, Oct. 2009. (Cited on pages 77 and 81.)

[140] W. van Elmpt, D. De Ruysscher, A. van der Salm, A. Lakeman, J. van der Stoep, D. Emans, E. Damen, M. Öllers, J.-J. Sonke, and J. Belderbos. The PET-boost randomised phase II dose-escalation trial in non-small cell lung cancer. *Radiotherapy and oncology: journal of the European Society for Therapeutic Radiology and Oncology*, 104(1):67–71, July 2012. (Cited on page 37.)

[141] J. Willner, K. Baier, E. Caragiani, A. Tschammler, and M. Flentje. Dose, volume, and tumor control prediction in primary radiotherapy of non-small-cell lung cancer. *International Journal of Radiation Oncology* Biology* Physics*, 52(2):382–389, Feb. 2002. (Cited on page 59.)

[142] R. Wilson. Radiological use of fast protons. *Radiology*, 47(5):487–491, Nov. 1946. (Cited on pages v, 1 and 3.)

[143] J. Wolf, M. E. Patno, B. Roswit, and N. D'Esopo. Controlled study of survival of patients with clinically inoperable lung cancer treated with radiation therapy. *The American journal of medicine*, 40(3):360–367, Mar. 1966. (Cited on page 6.)

[144] Q. Wu, R. Mohan, and A. Niemierko. IMRT optimization based on the generalized equivalent uniform dose (EUD). 1:710–713, 2000. (Cited on page 26.)

[145] T. Yamashita, T. Akagi, T. Aso, A. Kimura, and T. Sasaki. Effect of inhomogeneity in a patient's body on the accuracy of the pencil beam algorithm in comparison to Monte Carlo. *Physics in Medicine and Biology*, 57(22):7673–7688, Nov. 2012. (Cited on page 36.)

[146] M. Yang, G. Virshup, J. Clayton, X. R. Zhu, R. Mohan, and L. Dong. Theoretical variance analysis of single- and dual-energy computed tomography methods for calculating proton stopping power ratios of biological tissues. *Physics in Medicine and Biology*, 55(5):1343–1362, Feb. 2010. (Cited on pages 49 and 81.)

[147] C. Zacharatou Jarlskog and H. Paganetti. Physics Settings for Using the Geant4 Toolkit in Proton Therapy. *IEEE Transactions on Nuclear Science*, 55(3):1018–1025, 2008. (Cited on page 18.)

[148] S. M. Zenklusen, E. Pedroni, and D. Meer. A study on repainting strategies for treating moderately moving targets with proton pencil beam scanning at the new Gantry 2 at PSI. *Physics in Medicine and Biology*, 55(17):5103–5121, Aug. 2010. (Cited on page 69.)

[149] X. Zhang, Y. Li, X. Pan, L. Xiaoqiang, R. Mohan, R. Komaki, J. D. Cox, and J. Y. Chang. Intensity-modulated proton therapy reduces the dose to normal tissue compared with intensity-modulated radiation therapy or passive scattering proton therapy and enables individualized radical radiotherapy for extensive stage IIIB non-small-cell lung cancer: a virtual clinical study. *International Journal of Radiation Oncology* Biology* Physics*, 77(2):357–366, June 2010. (Cited on pages v, 7 and 51.)

[150] Y. Zhang, A. Knopf, C. Tanner, D. Boye, and A. J. Lomax. Deformable motion reconstruction for scanned proton beam therapy using on-line x-ray imaging. *Physics in Medicine and Biology*, 58(24):8621–8645, Nov. 2013. (Cited on page 77.)

[151] C. Zhu, R. H. Byrd, P. Lu, and J. Nocedal. Algorithm 778: L-BFGS-B: Fortran subroutines for large-scale bound-constrained optimization. *ACM Transactions on Mathematical Software*, 23(4):550–560, Dec. 1997. (Cited on page 25.)

[152] J. Ziegler. Comments on ICRU Report No. 49: Stopping Powers and Ranges for Protons and Alpha Particles. *Radiation Research*, 1999. (Cited on pages 12 and 13.)

[153] D. Zips and M. Baumann. Place of Proton Radiotherapy in Future Radiotherapy Practice. *Seminars in radiation oncology*, 23(2):149–153, Apr. 2013. (Cited on page 7.)